Fakultät für Chemie
Lehrstuhl für Technische Elektrochemie

Transport Processes in Li-Ion Batteries Studied by Impedance Spectroscopy and Small-Angle Neutron Scattering

Dipl.-Phys. Johannes Hattendorff

Vollständiger Abdruck der von der Fakultät für Chemie
der Technischen Universität München
zur Erlangung des akademischen Grades eines
Doktors der Naturwissenschaften (Dr. rer. nat.)
genehmigten Dissertation.

Vorsitzender: Prof. Dr. Thomas F. Fässler
Prüfende der Dissertation:
1. Prof. Dr. Hubert A. Gasteiger
2. Prof. Dr. Peter Müller-Buschbaum

Die Dissertation wurde am 07.11.2019 bei der Technischen Universität München eingereicht und durch die Fakultät für Chemie am 05.05.2020 angenommen.

Acknowledgment

Many contributed to this work and I am grateful to all of them but would like to thank especially the following. My doctoral advisor Prof. Hubert A. Gasteiger enabled this research by giving me a position at TEC and by inspiring me with electrochemistry, he gave invaluable input to all questions from general electrochemistry to lithium-ion batteries during my time in the lab. Also, this thesis was only possible with the support of Dr. Ralph Gilles who supervised the SANS work at the MLZ neutron source. A big thanks also to my colleagues at TEC, notably Irmgard Buchberger and Jörg Schuster from the ExZellTUM collaboration and Johannes Landesfeind. All SANS research has been conducted in close collaboration with Stefan Seidlmayer whom I also thank for XRD measurements and for reading the manuscript. At last, I thank my friends and family for supporting me during lab times and manuscript weekends. A special acknowledgment goes to my father for carefully reading the manuscript.

Munich, July 2019

Abstract - Zusammenfassung

The transport of lithium ions in liquid and solid phases is key to understanding the rate limitations of lithium-ion batteries. Here, two methods are presented to study the transport processes in both domains. First, graphite and lithium nickel manganese cobalt oxide (NMC) electrodes with increasing coating thickness are studied in a classical rate test and the associated resistances are calculated. Additionally, a dedicated AC impedance spectroscopy measurement, guided by the transmission line model in blocking conditions, is demonstrated which allows to measure the ionic resistance precisely and accurately. Tortuosity values for separators and electrodes determined by this method demonstrate that the often used Bruggeman assumption is not valid and that in reality tortuosity values are generally higher by a factor of two or more. Second, the lithiation of graphite is studied with small-angle neutron scattering (SANS). The theoretical framework and the experimental basics are prepared step-by-step in order to establish SANS as a method for studying lithium-ion pouch cells in situ and operando. The scattering signal is shown to be a superposition of the battery material contributions where the graphite anode is dominant. SANS signal and electrochemistry are correlated and a core-shell model of the lithiation of the graphite particles explains the observed features. Thus, SANS has been demonstrated as a new method to study the propagation of lithiation fronts in graphite and probably other materials in the future.

Der Transport von Lithium-Ionen in der festen und flüssigen Phase spielt eine entscheidende Rolle zum Verständnis der Leistungsgrenzen von Lithium-Ionen-Batterien bei hohen Stromraten. In dieser Arbeit werden zwei Methoden zur Untersuchung der Transportprozesse in beiden Domänen behandelt. Zunächst werden Graphit- und NMC-Elektroden mit ansteigender Beschichtungsdicke in einem klassichen Ratentest untersucht, dabei werden auch die entsprechenden Widerstände betrachtet. Eine zusätzliche, dedizierte Messung der Impedanz bei blockierenden Bedinungen im sogenannten „transmission line model“ erlaubt es, den ionischen Widerstand sehr präzise und genau zu messen. Die hieraus erhaltenen Werte für die Tortuosität für verschiedene Separatoren und Elektroden zeigen erneut, dass die oft benutzte Bruggeman-Formel nicht zutrifft und typische experimentelle Werte um einen Faktor zwei oder mehr nach oben abweichen. Daneben wird hier die Lithiierung von Graphit mit der Neutronen-Kleinwinkel-Streuung („small-angle neutron scattering“, SANS) verfolgt. Der theoretische Rahmen und die experimentellen Grundlagen werden Schritt für Schritt vorbereitet, um SANS als in situ und operando Methode für die Untersuchung von Pouch-Zellen zu qualifizieren. Das Streusignal kann dabei nachgewiesenermaßen als eine Superposition der Beiträge der einzelnen Batteriematerialien aufgefasst werden, wobei die graphitische Anode dominiert. Das SANS-Signal korreliert mit der elektrochemischen Analyse und die Lithiierung des Graphits kann mit einem Core-Shell-Modell erklärt werden. SANS ist also eine neue Methode, um die Fronten der Lithiierung in Graphit und möglicherweise zukünftig weiteren Materialien zu untersuchen.

Contents

1. Introduction

1.1. Status of battery technology

Since the experiments of Luigi Galvani [1] and Alessandro Volta [2] over 200 years ago, batteries have been a key device that helped to understand the phenomenon of electrical energy and that allowed its wide application. Batteries were the first source of a continuous supply of electrical energy and until today they play a role as back-up system. Today, stationary storage is again considered for some applications like solar home storage or short-term grid equalization. However, the main application of the dominating Li-ion batteries in the last decades has been as mobile power supply for all kinds of devices from power tools to computers and mobile phones [3, 4]. Furthermore, since a few years, batteries for electric vehicles are a rapidly developing market and the global stock of partly or fully battery driven cars has surpassed one million in 2015 [5]. It is not yet clear which drive train technology will dominate in the future, but it is clear that batteries and perhaps fuel cells will challenge the traditional internal combustion engine because they can significantly reduce global and local emissions. The choice between fuel cell and battery will be made based on factors such as cost, infrastructure, range and ease of use, and different options might be viable for specific applications [6]. Prices for Li-ion batteries have fallen dramatically in the last years and are already below 300 USD per kWh on the pack level and a further reduction by a factor of two seems plausible in the next decade [7, 8]. Improving the energy density remains the paramount goal for researchers but a breakthrough is not yet in sight. Li-sulfur and Li-oxygen technologies have seen increased research activity in the last years but seem far from application in the mass market [6, 9]. However, steady improvement of Li-ion technology is likely with new anode and cathode materials entering the market in the next decade [10–14]. Other promising technologies such as solid state batteries enabling Li metal anodes have yet to be proven [15].

1.2. The project ExZellTUM

This thesis was undertaken within the framework of the ExZellTUM project (Exzellenzzentrum für Batteriezellen an der Technischen Universität München) funded by the German Federal Ministry of Education and Research (BMBF) under grant number 03X4633A. Together, collaborators from electrochemistry, neutron research, electrical engineering and mechanical engineering set up a complete prototype pouch cell production facility at the Technical University of Munich. Research spanned from fundamental experiments at the neutron source and in small lab scale cells to aspects of (automated) production and testing of large-format 5 Ah cells (figure 1.1).

Figure 1.1.: 5 Ah pouch cell manufactured by the ExZellTUM project.

1.3. Organization of this thesis and novel ideas

This thesis is divided into three main parts. After a general introduction with some definitions and battery basics, the two main parts of this thesis are presented, i. e. impedance measurements and cycling experiments as well as neutron experiments with pouch cells. For each of the two, theory and experimental results are shown separately. Further details on experimental issues, data handling and error estimation are given in the appendices.
Several novel research ideas are presented in this work which ranges from simple electrochemical cycling experiments to specialized research at a neutron facility. Although known from theory, the blocking condition impedance measurement has not been applied broadly in battery research yet. In this work, in collaboration with others where mentioned, the fundamentals and practical limits of measuring battery material properties like tortuosity from impedance measurements have been studied in much detail. Furthermore, classical rate tests and the dedicated blocking condition tests have been compared for a range of thicknesses for anode and cathode in an innovative way. Also the SANS measurements comprise novel aspects. The study of well-defined laboratory pouch cells in situ and during operation combining scattering theory and electrochemistry was published with others for the first time [16]. In the present work, a thorough theoretical description of the measurements and further confirming measurements are added. Theory, material measurements, full cell and half cell experiments give a new clear picture of the possibilities of SANS for battery materials.

2. Battery basics

2.1. How a battery works

Basics and thermodynamics of the Li-ion battery

Secondary battery systems such as Li-ion are electrochemical systems that store electrical energy reversibly. Conversion from electrical to chemical energy and vice versa happens via redox reactions at the two electrodes, i. e. at anode and cathode which are separated by a separator soaked with electrolyte. The anode is defined as the more negative electrode where oxidation takes place during discharge, hence the name. On the other side, the cathode is the more positive electrode where reduction occurs during discharge [17, pp. 1.3.1/2]. A typical graphite vs. $Li_xNi_{0.33}Mn_{0.33}Co_{0.33}O_2$ (NMC-111) battery system is depicted in figure 2.1. During discharge oxidation occurs at the anode and graphite is delithiated, so that the Li-ion moves through the ion-conducting electrolyte to the cathode where it is reduced to form the lithiated metal oxide. So the reaction reads:

$$\begin{aligned} &\text{anode} && \mathrm{LiC_6} \rightleftharpoons \mathrm{C_6} + \mathrm{Li^+} + \mathrm{e^-} \\ &\text{cathode} && \mathrm{Li_{0.5}Ni_{0.33}Mn_{0.33}Co_{0.33}O_2} + \tfrac{1}{2}\mathrm{Li^+} + \tfrac{1}{2}\mathrm{e^-} \rightleftharpoons \mathrm{LiNi_{0.33}Mn_{0.33}Co_{0.33}O_2}\,. \end{aligned} \tag{2.1}$$

In parallel, the electron is moving through the external circuit from anode to cathode driving an electric load. During charge, the process is reversed by applying an external potential. The fundamentals of such electrochemical systems and analytical tools are well described in the literature, e. g. by Bard and Faulkner [18]. A short review of rechargeable batteries and fuel cells is given by Winter and Brodd in [19].

As in every chemical system, the Gibbs Free Energy ΔG represents the maximum amount of chemical energy which can be converted into electrical energy. It is:

$$\Delta G = \Delta H - T\Delta S \tag{2.2}$$

i. e. the reaction enthalpy ΔH minus the heat $T\Delta S$ with the entropy difference ΔS and temperature T. A spontaneous reaction is associated with a negative ΔG and, during discharge, drives an electrical current via the electromotive force connected to the potential U, so that:

$$\Delta G = -zFU \tag{2.3}$$

with z being the number of electrons involved in the redox reaction (1 for a Li-ion) and $F = e \cdot N_{\mathrm{A}}$ the Faraday constant, based on the Avogadro constant N_{A} and elemental charge e. The electromotive force U is the (positive) potential difference (without load) measured in Volt. This usable potential difference of a battery cell is characteristic of the used materials and given as the difference between anode and cathode potentials as shown in figure 2.1 (right). Potentials in electrochemistry are always measured against a reference, in this work against the Li metal redox couple Li/Li$^+$. For a given redox reaction the potential under open-circuit conditions (OCV) in the absence of an electrical load can be estimated by the Nernst equation:

$$U_{\mathrm{OCV}} = U_0 + \frac{RT}{zF} ln(\frac{a_{\mathrm{Pro}}}{a_{\mathrm{Rea}}}) \tag{2.4}$$

where U_0 is the standard electrode potential (reference), R the universal gas constant, and a_{Pro} and a_{Rea} are the activities of the products and reactants of the redox reaction. Typical battery potentials are in the range of a few Volts, e. g. 3 to 4.2 V for the graphite/NMC full cell.

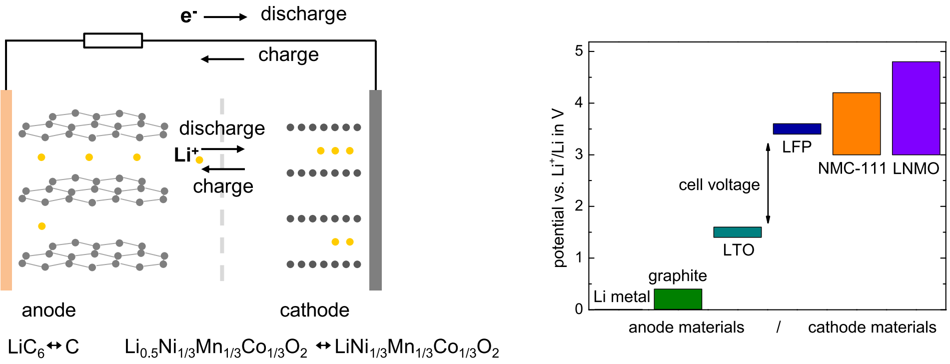

Figure 2.1.: Left: Scheme of a Li-ion battery. Right: Some anode and cathode materials and their potential ranges. Values from own measurements and from [14, 20].

The capacity of a battery material describes its ability to store charge and is therefore given in units of Coulomb (1 C = 1 As) or Ampere Hours (Ah). Faraday's law relates charge and converted material:

$$Q = I \cdot t = nzF \tag{2.5}$$

with the charge Q =current·time and the amount of converted material in mols n. E. g. for Li-ion during discharge, the charge of e is transferred for each conversion from LiC_6 to C_6 and the associated lithiation on the cathode side. The energy content W of the battery is given by:

$$W = Q \cdot U \tag{2.6}$$

It can be related either to weight (gravimetric energy density in Wh/kg) or to volume (volumetric energy density in Wh/liter). From equation 2.6 it follows that two strategies can improve the energy density, and thus e. g. the driving range of an electric car. One can aim to increase the capacity of the battery (Q per kg or liter) or one can aim to increase the average working potential of the battery.

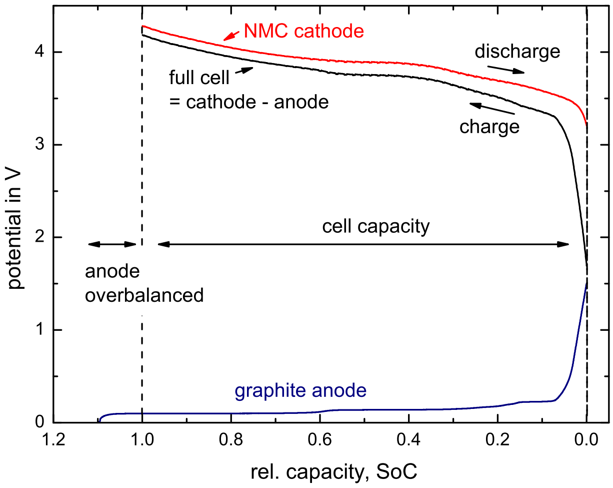

Figure 2.2.: The two electrode potentials graphite and NMC-111 are adding up to the full cell potential. Capacity (x-axis) is typically limited by one of the electrodes via utilization and cut-off potential or via the amount of transferable Li. Typically, the anode is oversized by 10% to avoid Li plating.

The specific potential that is associated with each material can be illustrated by a potential vs. charge curve, as shown for graphite and NMC-111 in figure 2.2. The shape of this curve depends on the redox reactions that take place in the system and may be flat, stepped or continuous. The reference curve of a material is measured against Li as counter electrode in a so called “half cell”. The “full cell” potential of a combination of two materials, say graphite and NMC, can be calculated from the individual contributions, $U_{\text{cell}} = U_{\text{cathode}} - U_{\text{anode}}$.

Kinetics and limitations of the Li-ion battery

When a current is drawn from a real battery, the situation is more complicated and in addition to thermodynamics, the kinetics of the processes have to be considered as well. All the kinetic hindrances visible in the effect on cell potential are usually subsumed under the term overvoltage. During discharge, hindrances decrease the useful potential, as shown in figure 2.3. We define the overvoltage η as difference of the thermodynamic open-circuit voltage and the effective terminal voltage [19]:

$$U_{\text{terminal}} = U_{\text{OCV}} - \eta \tag{2.7}$$

During charge, overvoltage increases the potential that has to be applied to charge the cell to a certain capacity value. The width of this hysteresis, i. e. the difference of charge and discharge potential at a given capacity is sometimes called overvoltage as well, a factor of ≈ 2 different from the definition before [21]. Using Ohm's law the overvoltage can also be understood as a resistance R which is called internal resistance. There are three main contributions to overvoltage. The first is due to the ohmic resistance of the electrode current collectors, the electrode matrix and the active material itself. It results in an immediate drop IR in potential. The second contribution which usually evolves on a longer timescale (10^{-4} to 10^{-2} s) is the activation polarization which stems from the kinetics of the charge-transfer reaction at the active material/electrolyte interface. Current and overvoltage are connected via the Butler-Volmer equation and show exponential behaviour. A third contribution at long timescales (seconds and more) is the concentration polarization which arises from limitations in mass transport (e. g. of the Li-ions) [22, p. 2.1]. E. g. in a simple setup with a separator between two electrochemically active electrodes, concentration polarization means that while applying a current the concentration of $\mathrm{Li^+/PF_6^-}$ pairs across the separator dimension will change. Usually at high rates, the transport process is slower than the production resp. consumption of $\mathrm{Li^+}$ at the electrodes which increases resp. decreases $\mathrm{Li^+}$ concentration at the interface. Due to charge-neutrality the PF_6^- concentration rises or drops accordingly and the result is a rise or drop in the local concentration of $\mathrm{LiPF_6}$. A limiting steady-state is reached when the concentration of $\mathrm{LiPF_6}$ reaches zero at the side where $\mathrm{Li^+}$ ions are consumed. So for a linear drop in concentration, there will be zero concentration at one side and twice the initial concentration at the other. The relevant transport limitations are shown in figure 2.3. Li-ion diffusion in the electrolyte (in separator and pores of the electrode) and in the solid active material is paramount. Figure 2.3 shows how the overvoltage rises in a non-linear fashion for higher discharge rates. Since the electrode potential is thus shifted for a real, current-bearing electrode it can make sense to insert a third current-free reference electrode into the battery to measure the undisturbed potentials.

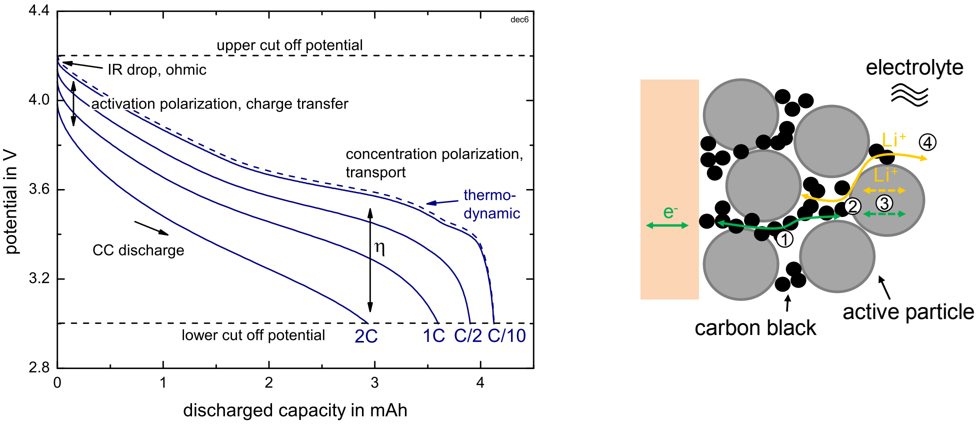

Figure 2.3.: Left: Effect of overvoltage on discharge capacity for different discharge rates. Right: Transport limitations for ions and electrons. Process 1 represents the electric conduction in the carbon black matrix, process 2 represents the electric contact resistance and ionic transfer resistance at the interface, process 3 the electrical and ionic conduction inside the active particle and process 4 the ionic conductivity in the liquid electrolyte.

Stability, operation and definitions

Kinetics play an important role not only for the cell potential but also for the function of the electrolyte. In a typical battery, as shown above, the potential vs. Li can reach near 0 V at the anode and more than 4 V at the cathode. The typical Li-ion electrolyte is a mixture of alkyl carbonates, e. g. ethylene carbonate (EC) and ethyl methyl carbonate (EMC), with a conductive salt, mostly $LiPF_6$. Fortunately it is stable against oxidation of the PF_6^--anion up to ≈ 4.5 V [23, table 4]. Below potentials of 1 V the alkyl carbonates of the organic solvent are generally sensitive to reductive reactions [23, table 5] which involves also the reaction of Li and therefore the deactivation or loss of cyclable Li. However, after the first cycle, i. e. charging the graphite in a full cell, a passivating metastable solid-electrolyte interface (SEI) is formed at the anode which drastically slows down the reduction of the electrolyte [24, 25]. A measure to quantify the continuous reduction of electrolyte and associated loss of capacity due to loss of cyclable Li is given by the so called Coulombic efficiency, defined as the ratio of charge obtained during discharge and the preceding charge:

$$CE = \frac{Q_{\mathrm{dch}}}{Q_{\mathrm{ch}}}\,. \tag{2.8}$$

After the first cycle, called formation, it is well above 99.9% in commercial cells. The loss in the first cycle is called irreversible capacity loss. There are also other side reactions that limit the lifetime of a battery and a variety of studies has been published on both aging during storage (calendaric) and aging during operation (cyclic) [26, 27].

For battery operation we make the following definitions: the C-rate denotes the current I of charge or discharge and is given as I/Q_{tot}, usually in units of 1/h. Accordingly, a rate of 0.5 C represents a current at which the battery is discharged within two hours; the unit of the C-rate is usually omitted. The total battery capacity Q_{tot} refers to the theoretically expected capacity, i. e. the nominal capacity or the capacity at very slow rates. There are two modes which can be applied in charging/discharging the battery: either galvanostatic with constant current (CC) or potentiostatic with constant voltage (CV). Typical charging procedures are CC followed by CV to ensure that the battery is fully charged, minimizing overvoltage at the end of charge. The state of charge (SoC) of a full cell is the actual charge (available as power source) related to the total charge, $Q_{\mathrm{actual}}/Q_{\mathrm{total}}$. So $SoC = 1$ or 100% for the charged cell. In this work, in a half cell SoC refers to the state of graphite as if it were in the full cell.

3. Experimental

The experimental details of the preparation of electrodes and battery cells are discussed in the following. In general, the procedures follow common practice as e. g. described by Marks et al [28]. All battery components were pre-dryed and assembled in an argon-filled glove box with typical water and oxygen level below 1 ppm.

3.1. Materials, electrode manufacturing

Anode materials

Anode materials used in this work were Li metal and graphite. Li foil (Rockwood Lithium) with a thickness of 450 µm was used as reference electrode and as counter electrode in half cells. It was always handled under argon atmosphere. Furthermore, potato-shaped synthetic graphite (SGL Carbon T157) with micrometer-sized particles as shown in figure 3.1 was used. The particle diameter was determined by laser diffraction particle sizing (Retsch-Horiba LA-950). The mean diameter is 22 µm (distribution by volume) with a standard deviation of 11 µm where the median diameter is 20 µm (distribution by volume). Practical capacities reached 360 mAh/g. More details on lithiation of graphite in general are given in section 5.1 later on. The Brunauer-Emmett-Teller (BET) surface was determined via nitrogen adsorption (Quantachrome autosorb iQ) as $4 \pm 0.2\,\mathrm{m^2/g}$.

Cathode materials

The cathode material NMC-111 (BASF), i. e. $Li_1Ni_{0.33}Mn_{0.33}Co_{0.33}O_2$, is a layered metal oxide which is especially popular in automotive applications because it is more stable than $LiCoO_2$ and has more energy density than $LiFePO_4$ [20]. Here, the material consists of spherical secondary particles with a mean diameter of 12 µm (distribution by volume) with a standard deviation of 4 µm. The median size was 11 µm. BET surface is given as $0.25\,\mathrm{m^2/g}$ from the specification sheet. Primary crystallites have a size of several hundred nm, as shown in figure 3.2 (a) and (b). The first charge capacity of NMC (i. e. including the first-cycle irreversible loss) reached 170 mAh/g and the reversible first discharge capacity was typically 150 mAh/g.

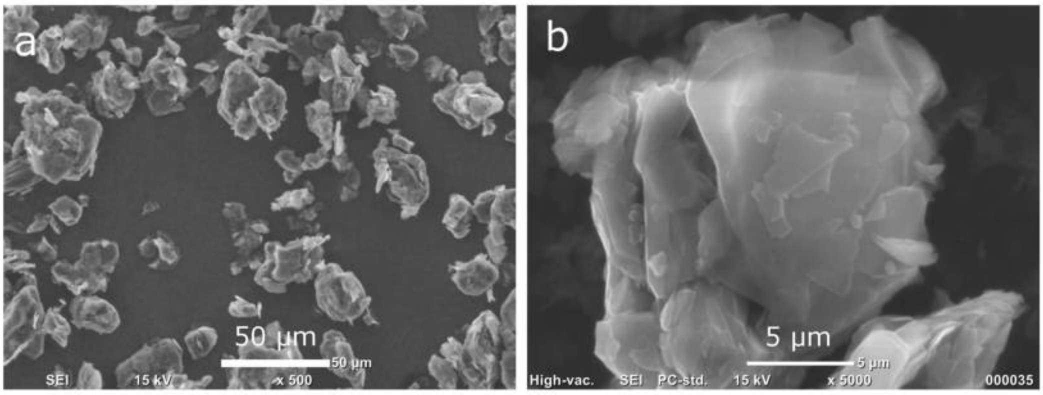

Figure 3.1.: Synthetic graphite anode particles.

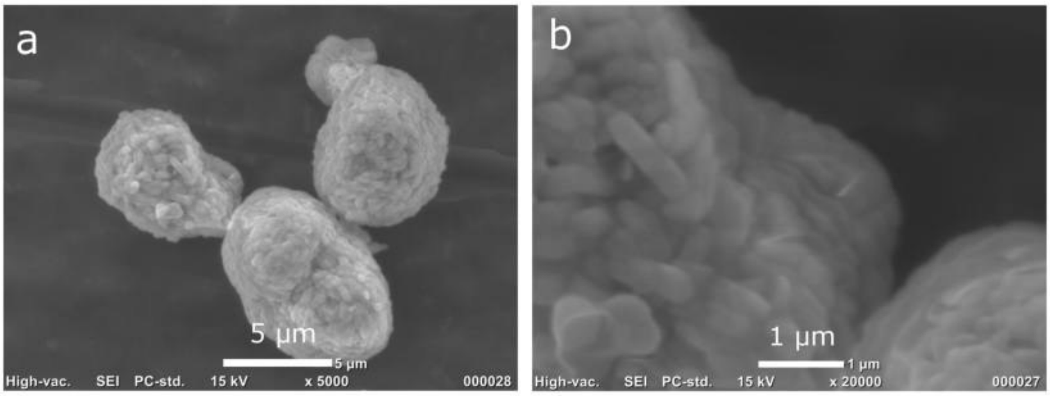

Figure 3.2.: NMC-111 cathode particles.

Slurry and electrode manufacturing

All slurries were prepared with N-methyl-2-pyrrolidone (NMP) as a solvent. Dry powders were mixed in a first step with a planetary mixer (rotation-revolution Thinky ARV-310) and then diluted step-by-step. The anode recipe was 95 wt.% graphite with 5 wt.% polyvinylidene fluoride (PVDF) as a binder. The cathode recipe included 96 wt.% NMC plus 2 wt.% PVDF binder and 2 wt.% carbon black (C65, Timcal) as a conductive additive. The slurry was coated with a doctor blade at controlled speed (K-Coater, Erichsen) to a thin Cu (12 µm) or Al (18 to 19 µm) foil (MTI Corp). The electrode was dryed in a convective oven at ca. 50°C and cut to measure with a knife or with a circular punch (Hohsen). After this, the electrode was compressed in a hydraulic laboratory press with a pressure on the order of 10^8 Pa, i. e. a weight of a few tons on the area of around 1 cm^2. Electrode weight and area were measured and the loading in mg/cm^2 or mAh/cm^2 was calculated.

The thickness of the complete electrode was measured with a Mitutoyo Litematic VL-50 with 0.01 N measurement force. The estimated error from this thickness measurement was confirmed by SEM measurements to be below 2%. From the thickness also the porosity can be calculated as ratio of void volume to the volume of the "envelope" cube:

$$\epsilon = 1 - \frac{\Sigma_{\mathrm{i}}\, m_{\mathrm{material,i}}/\rho_{\mathrm{material,i}}}{t\,A}\,, \tag{3.1}$$

where m is the mass and ρ the density of the solid material i and t is the coating thickness together with the considered surface element A. Before cell assembly, all electrodes were dryed at min. 95°C under vacuum. An overview of material properties is given in table 3.1.

Cu foil	8.7	mg/cm^2
Al foil	4.9	mg/cm^2
graphite	2.26	g/cm^3
NMC	4.72	g/cm^3
PVDF	1.76	g/cm^3
C65	2.00	g/cm^3

Table 3.1.: Areal weights of metal foils and densities of electrode active materials, PVDF binder and C65 carbon black.

Separator and electrolyte

As separator, two alternatives were used. In coin cells, usually a non-woven glass-fiber separator (uncompressed 250 µm thick, VWR) with a porosity of 90% was used. For transmission line model (TLM) measurements in T-cells mostly glass-fiber separator was used. In most of the pouch cells, standard commercial polyolefin separators such as trilayer PP/PE/PP Celgard C2325 and C480 (25 resp. 21.5 µm thick, porosities of 0.39 and 0.5) were employed [29]. The chosen standard electrolyte was EC:EMC (3:7 wt.%) with 1M $LiPF_6$ as a conductive salt and 2 wt.% vinylene carbonate (VC) as an additive (product name LP572, BASF). It was always handled under Ar atmosphere and kept dry (below 20 ppm H_2O). For some impedance measurements, an electrolyte consisting of EC:DMC (1:1 wt.%) with 10 mM $TBAClO_4$ (Sigma Aldrich, purity >99%) was used (DMC is dimethyl carbonate).

3.2. Cell systems, EIS systems

Standard coin cells

Most of the cells in this work were built as a coin cell (high quality steel SUS316L, parts by Hohsen Corp.) where the stack was made up of circular punched electrodes and separator. Typically a cathode was 14 mm, an anode 15 mm and the separator 16 mm in diameter. A spring ensured good stack pressure of ca. one bar after crimping and closing the coin cell, as shown in figure 3.3. Another commonly used system in the lab were T-cells (made of Swagelok fittings, figure 3.4) which could also be built with a third Li reference electrode. Here the diameters of cathode and anode were typically 10 to 11 mm. T-cells were also used for PEIS measurements of symmetric cells.

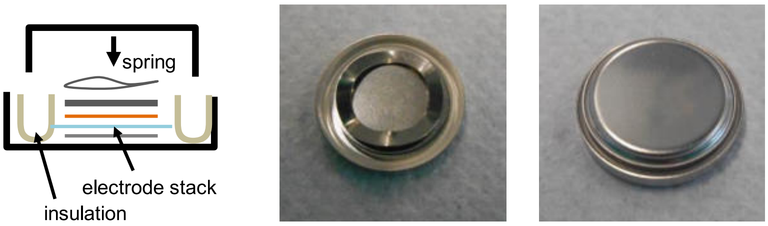

Figure 3.3.: Schematic drawing and picture of open (left) and closed (right) coin cell.

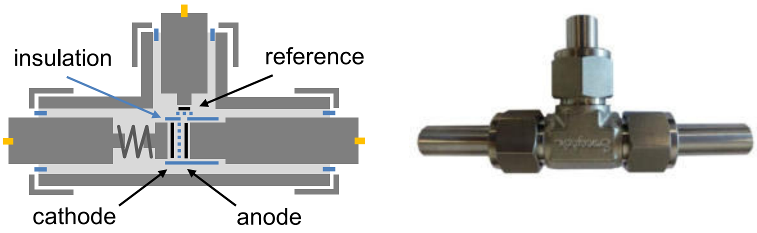

Figure 3.4.: Scheme and picture of Swagelok T-cell setup. Electrodes of 10 to 11 mm diameter are pressed upon each other and contacted via the rods and a spring. The reference is optional.

Pouch cells

For all in situ experiments, custom made lab-scale pouch cells were prepared. The typical cathode was $3 \cdot 3\,\mathrm{cm}^2$ and the typical anode (oversized both in geometric size and in loading) was $3.5 \cdot 3.5\,\mathrm{cm}^2$. Electrodes were cut directly from the coated electrode foil which included also a tab which was cleaned from coating and served as current collector tab. By leading the current collector foil directly outside the cell as a connector, contact resistances are avoided. The area of the electrode (coated and bare metal) was precisely measured by analyzing planar pictures of the electrode with a reference scale. Then, electrodes and separator were stacked in the pouch foil as depicted in figure 3.5. The assembly was fixed with BOPP adhesive tape (3M) and the current collector tabs were wrapped with sealing polymer tape at the edge. After filling in electrolyte, the pouch cell was sealed at 50 mbar with a vacuum sealing machine (Multivac) inside the glove box.

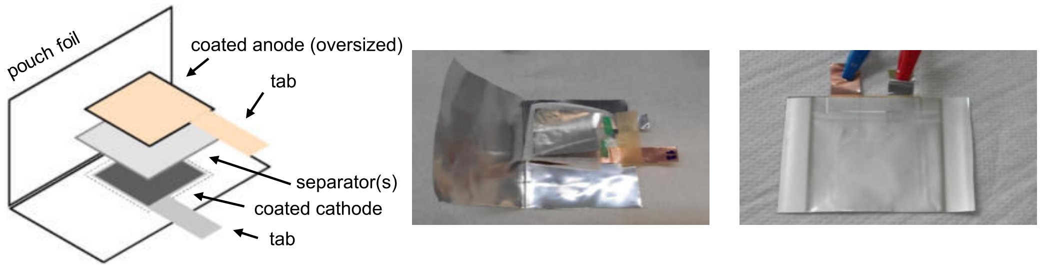

Figure 3.5.: Schematic drawing of pouch cell setup and picture of open (left) and sealed (right) pouch cell.

Cycling equipment and potentiostats

For cycling, the cells were placed in an oven at 25°C (Binder) and connected to either a battery cycler (Maccor) or a potentiostat (Biologic VMP-3). Typical cycling voltages for graphite/NMC cells were 3 to 4.2 V and for Li/graphite 0.01 to 1.5 V. With the potentiostat, also electrochemical impedance measurements were undertaken. Typically impedance was measured with an excitation of a few mV at frequencies between 500 kHz and a few Hz. Pouch cells were always connected with separate current and potential connectors (4-point-probe method) to avoid contact resistances. This was also used for most of the coin cells and T-cells; however, the internal resistances from the contact of the stack to plates and cell casing could not be eliminated. The electrical conductivity of coatings (in-plane) was also measured with a 4-point-probe setup where the resistance of a known area with defined thickness was measured.

The ionic resistance of separators was measured in a pouch cell and in a Cu block setup. The pouch setup was similar to the full cell pouch, except that anode and cathode were replaced by pure Cu foil electrodes. The separator was always very large compared to the electrodes and one electrode was smaller than the other to precisely define an effective area.

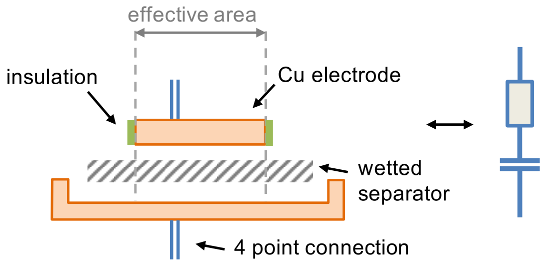

Figure 3.6.: Cu block setup to measure the ionic resistance of a separator; the right-hand side of the figure shows the equivalent circuit used to model the impedance response.

The second system was an open setup of two copper blocks as depicted in figure 3.6. The lower block formed a tray where the excessively wetted separator was placed. The upper block with a well defined effective area was placed on top and pressed by hand on the separator stack. This setup allowed very easy but reliable and repeatable measurements. For PEIS measurements in symmetric cells, also T-cells were used where both electrodes were 11 mm in diameter, fitting precisely in the cylindrical insulation.

4. Impedance spectroscopy study of battery materials

4.1. Theory: Impedance, porous materials and battery models

4.1.1. Basic elements of impedance spectroscopy

Electrochemical impedance spectroscopy (EIS), also called AC impedance spectroscopy, subsumes several techniques which measure the frequency dependent response of an electrochemical system. Orazem [30] and Lvovich [31] give a broad overview and Salomon [22] a short introduction. The concept of potentiostatic electrochemical impedance spectroscopy (PEIS) is to apply a fluctuating voltage U around a static potential (e. g. 0 V or OCV):

$$U(t) = U_1 \cdot e^{i\omega t} \tag{4.1}$$

where U_1 is the amplitude, $i = \sqrt{-1}$ and $\omega = 2\pi f$ the angular frequency. The current response $I(t)$ is measured and in the linear regime it oscillates accordingly shifted by a phase angle ϕ:

$$I(t) = I_1 \cdot e^{i(\omega t - \phi)} \tag{4.2}$$

The physical potential is of course either the real or the imaginary part of this function, but the complex notation allows easy calculation of various properties. E. g. the complex impedance Z is defined as:

$$Z = \frac{U(t)}{I(t)} = |Z|\, e^{i\phi} \tag{4.3}$$

with $|Z|$ being the magnitude equal to the length of the vector in complex space. The Nyquist diagram in figure 4.1 draws the two dimensions of complex space with a negative imaginary axis, as typically used in electrochemistry. Two frequency-dependent impedances are shown: on the left the semi-circle of a classical RC-element and on the right the point-like ohmic impedance (no frequency dependence) on the real axis together with a vertical line of a capacitance adding up in a serial circuit. As described in the experimental section, measurements here were done by simply scanning through the frequencies from kHz to mHz, applying a few oscillations at each data-point. It is important that the excitation amplitude (potential) is small so that the requirement of linearity is met. Also the measurement should be done in a stationary condition which limits the measurement time and thus the lowest measurable frequency. Data quality can generally be checked by calculation of the so called Kramers-Kronig residuals [32]. There are also sophisticated measurements in the time domain, e. g. step measurements which use Fourier transform to yield similar results for impedance values [33], but these are not used here.

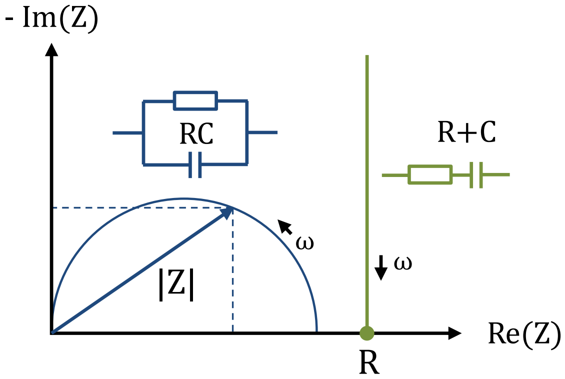

Figure 4.1.: Basic combinations of a resistor R and a capacitor C and their impedance response depicted in a so-called Nyquist diagram.

4.1.2. EIS of battery materials

In a real battery, ohmic, capacitive and sometimes even inductive behavior can be found. One can model the response of the battery by various equivalent circuits with more or less complicated layout. The first element of a typical equivalent circuit is always an ohmic contribution from the electronic resistance of battery materials. These include the resistance of wiring and tabs, current collector foils and of the active material in the conductive matrix (if carbon black was added). Also the ionic resistance of the electrolyte in the pores and the separator must be considered. In principle, impedance values of batteries can be measured in analogy to voltages between two electrodes. In a three-electrode setup with a reference electrode, the overall cell impedance can therefore be separated into anode and cathode impedances. However, it has been shown in the literature [34] that a reliable measurement is difficult and geometric artifacts can distort the results.

Porous materials

In general, we can relate the effective ionic conductivity κ_{eff} of an electrolyte filled porous matrix to the bulk ionic conductivity of the same free electrolyte κ by defining the MacMullin number N_{M} [35–37]:

$$N_{\text{M}} = \frac{\kappa}{\kappa_{\text{eff}}} \tag{4.4}$$

The MacMullin number of a porous solid where the solid phase is not contributing to the conductivity is therefore larger than one. The MacMullin number is often expressed as the ratio of tortuosity τ and porosity ϵ of the porous solid:

$$N_{\text{M}} = \frac{\tau}{\epsilon} \tag{4.5}$$

Note that different definitions of tortuosity are used. A simple geometric definition in two dimensions describes it as the ratio of the curved diffusion path through a pore to the straight length of the structure. Tjaden et al. [37] show how this tortuosity can be related to the tortuosity definition used above which they call tortuosity factor. The difference lies in using either τ or τ^2 depending on its definition. Here, and in most battery literature, tortuosity is understood as defined in equations 4.4 and 4.5, i. e. by defining it as part of the proportionality constant of the effective and bulk electrolyte conductivity so that $\kappa_{\text{eff}} = \epsilon/\tau \cdot \kappa$. A bulk phase without pores has a tortuosity of one. A porous system with less effective conductivity has a tortuosity of larger than one.

The tortuosity is often approximated by an empirical relationship which was first introduced by the dutch physicist Dirk A. G. Bruggeman in 1935 [38]. Newman and coworkers introduced it to the battery simulation community where it is widely used today [39, 40]. Here, tortuosity is a function of porosity ϵ and expressed as:

$$\tau = \epsilon^{-\alpha} \text{ , with } \alpha = 0.5 \text{ for spheres} \tag{4.6}$$

This needs not be true for anisotropic materials with complex shapes like real battery electrodes and the validity of the Bruggeman assumption is reviewed in the following.

Ohmic resistance of separator

Returning to the general equations 4.4 and 4.5, for a separator of thickness t, area A, filled with an electrolyte with conductivity κ we can write:

$$R_{\text{ion}} = \frac{\tau}{\epsilon} \frac{t}{A\kappa} \tag{4.7}$$

Here, ϵ is the porosity and τ is the tortuosity of the separator. Note that in a separator the solid phase is non-conducting and all conductivity is restricted to the liquid electrolyte phase. The ohmic resistance of the electrolyte in the separator is typically larger than all other ohmic contributions in a lithium ion battery and dominates the ohmic resistance. In a battery electrode, electronically and ionically conducting phases are mixed which results in complicated behavior as we will see below. When measuring a typical Li-ion cell at very high frequency (above 100 kHz), one mostly measures the ohmic resistance which is dominated by the ionic resistance in the separator as given by equation 4.7. It is the minimum internal resistance.

Capacitor and constant-phase element

Another element of battery equivalent circuits is a capacitor which represents e. g. electrochemical double-layers at chargeable surfaces [18, p.11ff.]. This is the case for so called ideally polarizable electrodes or blocking conditions where no faradaic current (i. e. no charge transfer reaction) occurs. A simple example is the Cu surface in an electrolyte with a standard conductive salt which does not undergo charge transfer reactions at a low excitation potential of a few mV. In a real system the capacitive behavior is better described by a constant-phase element (CPE) and the impedance is:

$$Z_{\mathrm{CPE}} = \frac{1}{Q(i\omega)^{\gamma}} \tag{4.8}$$

where ω is the angular frequency and Q a parameter. The constant-phase exponent γ is < 1 for CPE behavior and the unit of Q is adjusted accordingly. For an ideal capacitance $\gamma = 1$, and Q is the standard capacitance C. The CPE model fits well to experimental data but its physical origins are still debated and several root causes are in discussion, such as surface roughness [41] or inhomogeneities in general which lead to an inhomogeneous distribution of resistances and capacitances across the surface [42]. Note that for high frequencies the impedance of a capacitor or a CPE goes to zero, i. e. reduces to a simple conductive connection in an equivalent circuit diagram. Another special case is $\gamma = 0.5$ which is represented by a line with a slope of 45° in the Nyquist diagram and called Warburg impedance. This element represents diffusion in the liquid electrolyte and is valid for an infinite thickness of the diffusion layer. More complicated expressions of impedance for multi-dimensional and finite diffusion exist as well. At high frequencies diffusion can be neglected since the ions do not move very far from equilibrium, at low frequencies however rearrangement via diffusion can happen.

Charge transfer and RC-elements

Classical electrochemistry describes processes at interfaces and the charge transfer that happens during a reaction. The solid-liquid interfaces in a Li-ion battery are the places where redox reactions of the Li/Li$^+$ couple and charge transfer take place. Such charge transfer generally follows the Butler-Volmer law [18, 33]. The faradaic current I (per area) is given as a function of applied overpotential η:

$$I = I_0 \left(e^{\frac{\alpha z F}{RT}\eta} - e^{\frac{-(1-\alpha) z F}{RT}\eta} \right) \tag{4.9}$$

with z, F, R, T as defined in equation 2.4. α is the transfer coefficient which is 0.5 for a symmetric anodic/cathodic reaction. I_0 is the exchange current density at $\eta = 0$. For an ideal Butler-Volmer process the faradaic current increases exponentially for higher overpotentials in the well-known Tafel regime. In a real system however, the current is often limited by transport processes and a saturation current I_{limit} is reached. Figure 4.2 illustrates this behavior; it also shows how an oscillating AC impedance measurement at a certain overpotential, which can be $\eta = 0$ or as shown here around η_{bias}, induces an oscillating current response around the respective current level I_{bias}. It is evident that linearity is only given for very small potential changes. EIS measurements of battery systems are often and also in this work done around OCV, so $\eta = 0$ and at this point the so called charge-transfer resistance R is defined as the ratio of potential to current. In general, the interface does also have a certain capacitance and the two elements are combined in parallel to get an equivalent circuit element for charge-transfer processes. The charge-transfer resistance is a function of overpotential or equivalently current. A common observation following from Butler-Volmer is, that the internal resistance of a battery drops with higher currents, which is however only true when no transport limitations occur. In a real system under load, the dependence of resistance on current is non-trivial and various loss and transport processes play a role, as shown later in this work. Surface capacitances are usually constant with respect to applied current densities [33].

In summary, RC-elements are building blocks of equivalent circuit models which describe various charge-transfer processes or reactions at anode and cathode. The resistance is related to the kinetics of this reaction. An RC-element is represented by a characteristic semi-circle in the Nyquist diagram as already shown in figure 4.1. The impedance is given by:

$$Z_{\text{RC}} = \frac{R}{1 + i\omega RC} \tag{4.10}$$

where R is the value of the resistance and C the capacitance of the capacitor. Kinetics of the underlying faradaic process are characterized by the characteristic time constant RC and the apex of the semi-circle is at $\omega = 1/RC$.

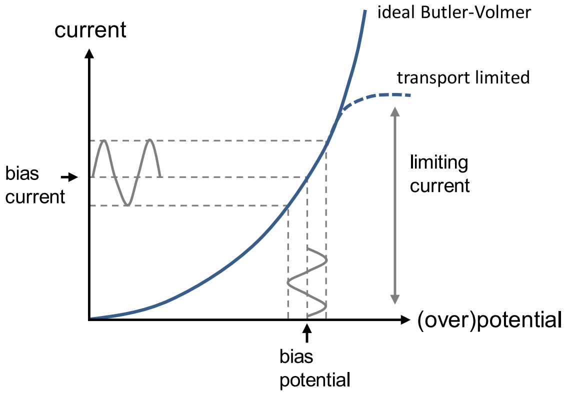

Figure 4.2.: Charge transfer with Butler-Volmer kinetics and transport limitations at higher overpotential. An AC-impedance around a bias voltage (and thus a bias current) is illustrated by a sinusoidal change in potential. Here, the sinusoidal current response is already slightly non-linear and upper and lower amplitude boundary are asymmetric in the graph. Graph inspired by Park et al. [33]

In battery systems several RC-elements are usually connected in series, representing different charge-transfer processes e. g. at anode and cathode with their respective time constants.

Another root cause of RC-behavior is contact resistance. It is often neglected, but a high contact resistance at e. g. an active particle to the current collector metal foil is perfectly modeled by an RC-element as shown by Gaberšček et al. [43]. One has to take care not to attribute this RC-behavior to faradaic electrode processes. Useful checks could be to e. g. change the substrate to materials with better contact (e. g. soft Cu) or to apply pressure and identify the shrinking of the RC semi-circle caused by contact resistance.

Figure 4.3 shows a typical experimental impedance response of a battery system. An ohmic high frequency resistance (HFR) marks the starting point at the lowest value along the x-axis and for lower frequencies two overlapping RC semi-circles and a Warburg diffusion tail can be identified. A simple equivalent circuit to describe such behavior (but only one RC-semi-circle) is a resistance in series with an RC-element which includes a Warburg impedance on the resistive branch. It is called Randles circuit [22, p. 2.27] after J. Randles [44].

Transmission line model

We can use the circuit building blocks given above to construct a model for the battery electrode where the active material matrix is structured by pores filled with electrolyte. Figure 4.4 (a) shows an appropriate model for this two phase system which is called transmission line model. After having passed the contact

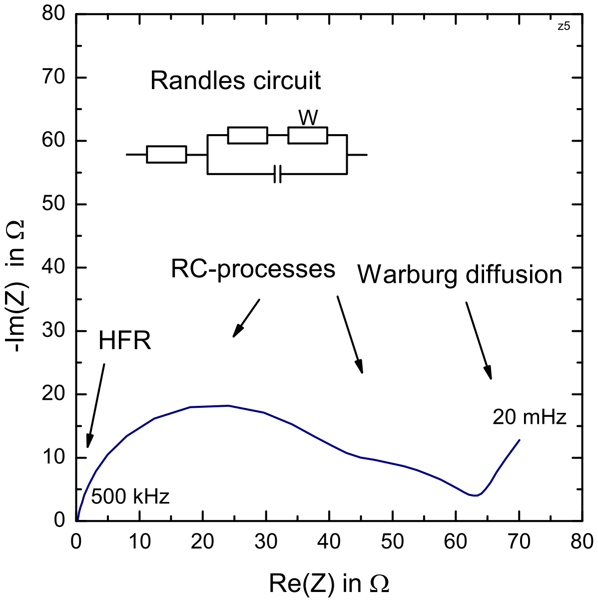

Figure 4.3.: Typical PEIS from a pouch full cell showing HFR, RC and Warburg behavior from diffusion. A simple equivalent circuit is the Randles circuit.

resistance element, electrons can travel in the solid phase through serially connected ohmic resistances r_{el}. In the liquid phase of electrolyte, ions can move analogously through ionic resistances r_{ion} which add up linearly with the length of the conductive path. In a general transmission line model in non-blocking condition, charge-transfer happens via an RC-element at the surface and connects the two branches. r_{t} is the transfer resistance and c_{t} the capacitance of this element. $R_{\mathrm{ion,s}}$ is the residual ionic resistance of the electrolyte in the separator.

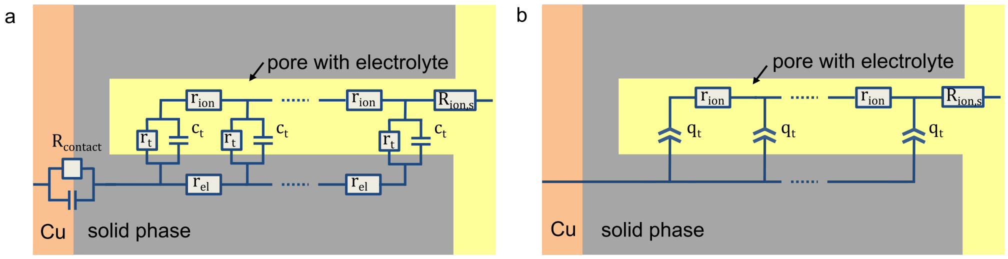

Figure 4.4.: Transmission line model for a porous battery electrode including contact resistance RC-element (a) and simplified model neglecting the electrical resistances (b).

In a typical electrode, the electronic conductivity in the solid phase of the electrode (often enhanced by the addition of carbon black) is much higher than the conductivity of the electrolyte. For layered transition metal oxide based cathodes the electronic conductivity of the electrode is on the order of 10 S/m, for graphite anodes 1000 S/m [45] which was confirmed by four-point-probe conductivity measurements for the electrodes tested here. So, a typical LP572 electrolyte with a bulk conductivity of 1 S/m (often given as 10 mS/cm) is at least one order of magnitude worse in conductivity. Additionally, in the TLM measurements an electrolyte with very low conductivity of 0.05 S/m is chosen. Thus, we can neglect the electronic resistances. Furthermore, in blocking condition where no charge transfer happens we can replace the RC-element at the surface by a pure capacitor or in a realistic system by a constant-phase element with a capacitive value of q_{t}. For a typical electrochemical double-layer, the capacitance is on the order of $10^{-5}\,\mathrm{F/cm^2}$ [43]. Such a simplified transmission line model is shown in figure 4.4 (b). For this transmission line model an analytic expression has been derived for application to porous layers in fuel cells [46, 47] and battery electrodes by Ogihara et al. (with $\gamma = 1$)[48, 49] guided by the early work of De Levie [50]. In the general case with variable γ (CPE) and without ionic resistance in the separator, the impedance is given by:

$$Z_{\mathrm{TLMQ}} = \sqrt{\frac{R_{\mathrm{ion}}}{Q_{\mathrm{t}}(i\omega)^{\gamma}}}\, coth\left(\sqrt{Q_{\mathrm{t}}(i\omega)^{\gamma} \cdot R_{\mathrm{ion}}}\right) \tag{4.11}$$

where $R_{\mathrm{ion}} = \sum r_{\mathrm{ion}}$ and $Q_{\mathrm{t}} = \sum q_{\mathrm{t}}$. The Nyquist plot in figure 4.5 shows the typical TLM behavior. At low frequencies capacitive behavior dominates, at higher frequencies a typical 45° slope is observed and at very high frequencies the curve hits the real axis at the residual ohmic resistance. Since the capacities have no impedance at very high frequencies, the main current path is simply through the solid phase to the last transition element and into the electrolyte and further through the remaining ionic resistance in the separator. The effect of $\gamma < 1$ is to rotate the whole curve slightly to the right, resulting in a TLM slope smaller than 45°. A fit of experimental data to equation 4.11 yields the unknown variables (Q_{t},R_{ion},γ), especially the ionic resistance. Another method is to extrapolate the low frequency branch to the real axis to get the low frequency resistance (LFR). Liu and Ogihara et al. have already shown that for $\gamma = 1$:

$$Z_{\mathrm{LFR}} = \frac{R_{\mathrm{ion}}}{3} + \underbrace{R_{\mathrm{ion,s}}}_{\mathrm{HFR}} \tag{4.12}$$

where the HFR of the electrolyte/separator is just added.

When charge transfer can happen, in the so called faradaic or non-blocking condition, we have to include the transfer resistances r_{t} which are now finite (and not infinite). The TLM-formula [48] in this case reads:

$$Z_{\mathrm{TLMQf.}} = \sqrt{\frac{R_{\mathrm{ion}} R_{\mathrm{t}}}{1 + R_{\mathrm{t}} Q_{\mathrm{t}} (i\omega)^{\gamma}}}\, coth \left(\sqrt{\frac{(1 + R_{\mathrm{t}} Q_{\mathrm{t}} (i\omega)^{\gamma}) \cdot R_{\mathrm{ion}}}{R_{\mathrm{t}}}} \right) \tag{4.13}$$

with $R_{\mathrm{t}} = \sum r_{\mathrm{t}}$ when still neglecting the electronic resistance. Figure 4.5 shows the faradaic TLM response which at high frequencies evolves similar to the blocking model, but does not show capacitive behavior but rather an RC-semi-circle at low frequencies. In conclusion, blocking and faradaic condition show very different behavior in the Nyquist plot and can be well distinguished in the experiment. In a study of $LiNiO_2$-based cathode electrodes, Ogihara et al. tuned the condition of the electrochemical impedance system by varying the SoC [49]. For 0% SoC blocking conditions were achieved, for 50% SoC faradaic conditions, respectively. This is in line with others who have found that the transfer resistance of typical electrodes increases at low SoC [32, 51].

In this study, an electrolyte without a Li-salt is used in order to guarantee non-intercalating conditions. Instead of the usually used $LiPF_6$ conducting salt which provides Li^+ cations, the salt tetrabutylammonium perchlorate $TBAClO_4$ is used. At the potential window of the impedance measurement (at OCV ± <25 mV) this cation does not intercalate into the anode [52] or cathode materials (compare also [53, chapter 4]). As also discussed in our publication [54], any RC-semi-circle observed in the measurement can then clearly be attributed to a contact resistance contribution.

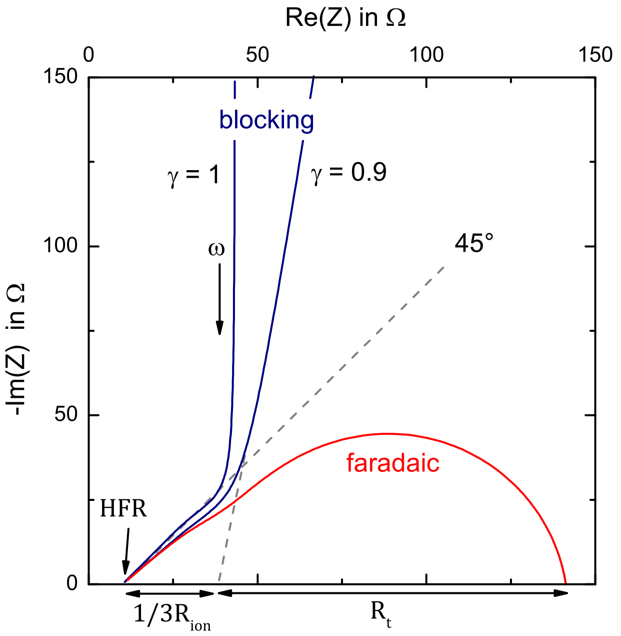

Figure 4.5.: Blue curves, TLM plot in blocking condition (equation 4.11) with varying γ. Red curve, TLM plot in faradaic condition (equation 4.13), where R_t is not infinite and charge-transfer is possible. Plot parameters: R_ion=100 Ω, Q_t = 0.0001 Fs$^{\gamma-1}$, HFR=10 Ω, R_t=100 Ω.

4.1.3. Battery models and tortuosity

A more sophisticated modeling approach is the so called porous electrode model which was introduced by Newman, Doyle and Fuller [40, 55]. This model is able to simulate charging and discharging of a battery in a pseudo two-dimensional geometry, as shown in figure 4.6. The first dimension is typically the x-dimension from anode to cathode and the second dimension represents the radial dimension of the solid active material particle. Diffusion and conductivity in the liquid electrolyte and the two solid phases are modeled by differential equations. The porous nature of the materials is considered by using effective values of transport parameters, e. g. the conductivity $\kappa_{\text{eff}} = \kappa \cdot \epsilon/\tau$ is adjusted by porosity ϵ and tortuosity τ as in equations 4.4 and 4.5. Charge and mass conservation and starting respectively boundary conditions are added. Butler-Volmer relations are used to link solid and liquid domain by giving the charge transfer currents at the active material surface as a function of overpotential. Here, the experimentally measured open circuit potential is conventionally used as the SoC-dependent equilibrium potential. The tortuosity τ is usually expressed through the Bruggeman relation, equation 4.6. The tortuosity τ is a critical input parameter which has a strong influence on the high current performance of the electrode.

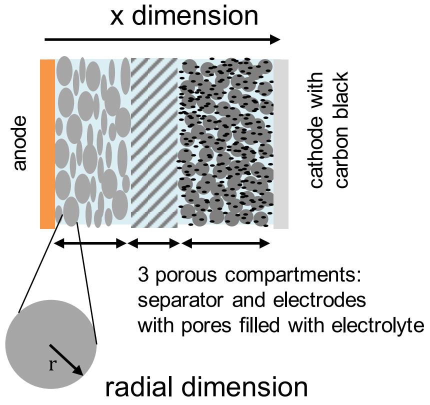

Figure 4.6.: Sketch of the three porous media model compartments and the two dimensions: electrode direction and radial dimension inside the particle.

4.1.4. Effective transport properties in literature

Separators

The ionic resistance of battery separators can be determined by a simple measurement with any kind of electrolyte which is widely applied in industry and research

[29, 35, 56, 57]. However, reported values for ionic conductivity or for the related quantities MacMullin number or tortuosity vary quite significantly. Take the Celgard 2500 separator as an example for which the reported MacMullin numbers vary from 8.5 [35], 13 [57] to 18 [56]. A small scatter could be explained by the error from measurement of input parameters for the calculation such as thickness or porosity. Also, the production methods of separators may vary over time. But such a large deviation suggests that experimental artifacts cannot be excluded in some of the measurements. Therefore, special care was taken here to minimize all error contributions. For the calculation of tortuosities we assume the porosity given by the manufacturer which is usually given from a simple calculation of the void fraction from outer dimensions and polymer density, similar to equation 3.1 or from absorption experiments [29].

Although, the electrodes are the limiting factor in most cases, also the electrolyte in the pores of the separator has a limiting current. If we assume that diffusion is the dominant transport mechanism in the liquid phase (neglecting convection and also migration) we can write down Fick's law of diffusion and set in the limiting case when we have a concentration gradient of twice the equilibrium $\mathrm{LiPF_6}$ concentration c_0 over the effective thickness $\tau/\epsilon\, t$ of the separator:

$$\frac{I_{\mathrm{limit}}}{A} = zFD\,\frac{\delta c}{\delta x}\bigg|_{\mathrm{limit}} \approx zFD\frac{2c_0}{\tau/\epsilon \cdot t} \tag{4.14}$$

where I_{limit}/A is the purely diffusion limited current density based on Fick's law, with $z = 1$ for $\mathrm{LiPF_6}$, the Faraday constant and the electrolyte diffusivity D [22, p. 2.16]. Following the general relation between conductivity and diffusivity [58], we can write $D = \kappa k_{\mathrm{B}} T/(e^2 c_0)$ with the Boltzmann constant, the temperature T, the elementary charge e and the concentration of $\mathrm{Li^+}$ in the electrolyte $c_0 = 1\,\mathrm{mol/l}$, and get $D_{\mathrm{electrol}} \approx 2.6 \cdot 10^{-6}\,\mathrm{cm^2/s}$. Here, some assumptions such as dilution are made. For a typical glass-fiber separator of $200\,\mu\mathrm{m}$ (compressed) thickness and $\tau/\epsilon \approx 1$ we get a limiting current of around $20\,\mathrm{mA/cm^2}$. A similar value is obtained for the Celgard separator which is a factor of 10 thinner but has a much higher τ/ϵ. Current densities here are in most of the cases below these values, so we expect indeed to see the limiting behavior of the electrodes. In the data, performance at a given current density is also varying with electrode thickness which indicates current-limiting factors within the electrodes as well.

Electrode performance and tortuosity

It is long known that transport properties are the key to high performance. Typical high performance, i. e. high power batteries as used in hybrid electric vehicles feature usually very thin electrode coatings. In contrast, high energy batteries minimize inactive materials content and use thick coatings [3]. In recent years, some researchers tried to make thicker coatings while still enabling sufficient rate performance. A direct comparison of the quantitative influence of electrode thickness is of course not possible due to the variety of materials and processes used, but trends can be discussed.

Lu et al. [59] show that thicknesses around 100 µm are optimal because of transport restrictions and also mechanical integrity limits. Zheng et al. [60] vary cathode thickness (LFP and NMC) and find that diffusion limits high rate performance. Both agree that the resistance, which they measure by relatively fast 10 s current pulses, scales inversely proportional to thickness. And they find that the achieved areal capacity scales with the square root of discharge time. The work of Tran et al. [61] varied the thickness of NCA cathodes and Singh et al. [62] that of NMC electrodes, and both find similarly limited high rate performance. Part of the effect is attributed to electronic transport or contact limitations or also limitations in the separator from high current density. Sivakkumar et al. [63] find similar results for thick graphite electrodes. Some papers find no influence of thickness on aging [59] whereas others [60] claim that increased mechanical stress and triggered side reactions from higher current densities (based on the area of the separator) could indeed reduce lifetime.

Other researchers have furthermore used models to understand experimentally measured limitations. Gallagher et al. [64] have compared experiments with Ni-rich NMC material to an electrochemical model. They postulate that performance is depending on the so called penetration depth which is a measure of how much of the electrode is still used when electrolyte polarization occurs. They find a relationship where the achieved discharged capacity at a given rate is proportional to the square root of discharge time or equivalently to the square root of the inverse current, similar to what Zheng et al. have observed. However, the theoretical capacity relationship reported by Gallagher et al. is also proportional to the square root of porosity over tortuosity. Thus, the precise determination of these parameters is a pre-requisite for a meaningful model. Indeed, other literature (e.g. Zheng et al. [65]) has shown how electrode performance varies with porosity and tortuosity.

Model-based optimization of electrodes

In fact, already the first electrochemical models were used to find out optimized parameters for electrode manufacturing. Fuller et al. [55] vary the thickness of the positive electrode. Arora et al. [66] compare a similar theoretical variation to experiments and Wang et al. [67] model electrodes to deduce a critical thickness and critical rate. Nemani et al. [68] showed how the design of electrode microstructure or tortuosity, e. g. by having regions of high and regions of low tortuosity can enhance electrode performance. And Han et. al. [69] showed experimental results with the same principle, enhancing performance by an extra porous additive to the anode.

Measurement of electrode porosity and tortuosity

To understand the properties of a given electrode before or after optimization, reliable measurement methods are needed. In the case of electrodes, the determination of the effective transport properties such as tortuosity is unfortunately not straightforward because the porous medium itself is now electronically conductive. A typical EIS measurement will therefore give a mixed response from ionic and electronic conduction pathways as shown above. Researchers have thus used a range of different techniques to measure these properties.

Thorat et al.[36], Zacharias et al. [70] have measured τ/ϵ of porous electrodes by comparing the effective diffusion coefficient in a freestanding electrode sheet to the bulk diffusion coefficient in the pure electrolyte. A quantitative result is deduced by comparing the voltage response of a current pulse (so called polarization-interrupt method) to a numerical model. The preparation of the freestanding electrode by delamination or dissolution of the metal substrate is however not trivial. Another drawback is that the model requires knowledge of the concentration-dependent values of the transference number, the thermodynamic factor and the diffusion coefficient. Holzer et al. [71] applied similar methods to fuel cell materials.

Another method by DuBeshter et al. [72] measures the pressure-dependent term of the gas diffusion coefficient through the porous electrode. This assumes however an isotropic electrode morphology which is not true for flake like particles like typical graphite. The effective conductivity can also be calculated by solving the transport equations in the pores given by the exact morphology of the electrode. X-ray tomography and cross sections from focused ion beam scanning electron microscopy (FIB-SEM) [73–78] or even normal SEM cross section images [79] are used to generate 3D reconstructions of porous electrodes. A drawback of this method is the limited resolution of 3D-imaging methods which cannot resolve typical carbon black particles below 0.1 µm.

Sophisticated AC impedance methods like the TLM method described have been used for fuel cell by Liu et al. [47] and by Ogihara et al. for cathodes [48, 49] and by Cericola and Spahr for anodes [80]. Liu et al. could eliminate the charge transfer resistance in the TLM circuit model by removing the reacting gases and achieve blocking conditions. Ogihara et al. reach blocking condition by varying the state of charge, as described in section 4.1.2. They are thus able to distinguish ionic resistances in the electrode even though they do not calculate tortuosities from it.

4.2. Results from impedance spectroscopy of battery materials

In this section results of electrical impedance spectroscopy of battery materials ranging from separators to electrodes are presented. The aim was to determine an important parameter of effective transport which is the tortuosity. Results of similar measurements and the data of figures 4.7 and 4.8 have already been published together with J. Landesfeind and others [54, 81].

4.2.1. Ionic resistance of separators

A simple application for impedance spectroscopy is to determine the ionic resistance of a separator filled with electrolyte. As already discussed, the equivalent circuit is an ohmic resistance given by equation 4.7 in series with a capacitor. The real system is better described by a constant-phase element so that the capacitive branch is a little bit tilted in a Nyquist diagram. But in all cases, the data can be fitted by a line (see also appendix A.1) which hits the real impedance axis at the value of the ionic resistance. Figure 4.7 shows the ionic resistance (i. e. the intersection value with the real axis) of several separator measurements. Here, Celgard 2325 and C480 separators were used. Two factors of equation 4.7 were varied. First, the number of separator layers was varied, which is equivalent to varying the thickness t. The results show a perfect linear behavior (linear fit with $R^2>0.99$) as expected. This is even valid for both setups, i. e. the evacuated pouch cell and the simple Cu-block setup in a glove box environment. We can therefore assume that geometric effects do not play a role here and that the separators are completely wetted. The standard electrolyte here was always EC:EMC 3:7 (wt.%) with 1 M $LiPF_6$ with a conductivity of 9.26 mS/cm. We calculate the tortuosity τ from the fitted slope and get $\tau = 4.1 \pm 0.2$ for Celgard 2325 and $\tau = 3.4 \pm 0.2$ for C480. Both tortuosities are significantly higher than the Bruggeman estimation (equation 4.6) of 1.6 ($0.39^{-0.5}$) and 1.4 ($0.5^{-0.5}$) respectively. For Celgard 2325 we can calculate the equivalent MacMullin number $N_{\mathrm{M}} = 10 \pm 0.6$ from our measurement which is higher than the value of 7.0 reported by Arora et al [29]. However, both values are higher than the Bruggeman estimate for the MacMullin number of Celgard 2325 which is $N_{\mathrm{M}} = 4.1$ (Bruggeman).

The second experiment varied the conductivity κ by using different electrolytes when measuring the ionic resistance of Celgard 2325 in the Cu-block setup. By using equation 4.7 we can calculate the respective tortuosities. The two other electrolytes were EC:DEC 1:1 (wt.%) with 0.5 or 1 M $LiClO_4$ and a conductivity of 5.38 and 5.81 mS/cm, respectively. Within the error bars estimated from simple propagation of error, the tortuosity is independent of conductivity, as expected, and is close to 4.1. In summary, the variation of measurement system, the separator thickness and the electrolyte conductivity proved the reliability of the tortuosity measurement method and questioned the validity of the simple Bruggeman estimation for typical battery separators. Key to a reliable measurement is the precise control of the ionically conductive path, i. e. to have two precisely defined active surfaces with the separator in between and no stray currents around the edges of the current collectors. Similar results have been measured with a range of separators as shown by us [54, 81]; the result for Celgard 2320 has been confirmed by Hantel et al. recently [82].

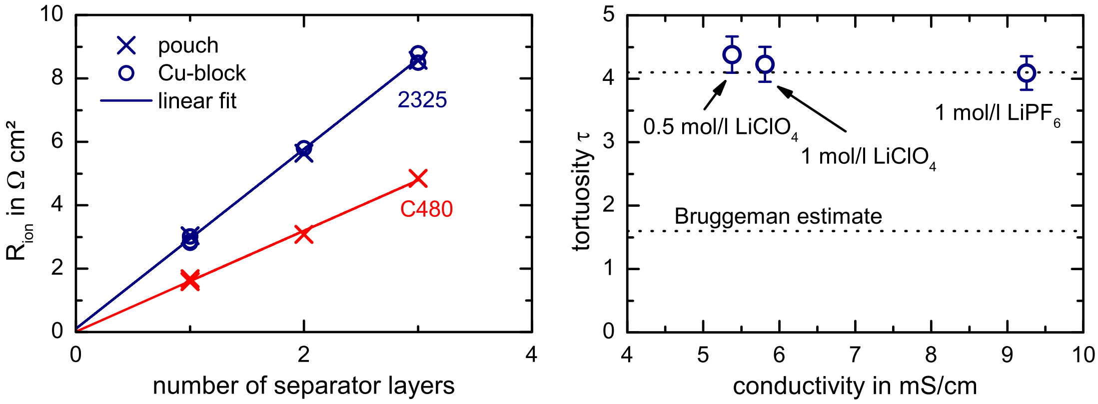

Figure 4.7.: Left: Specific ionic resistance of Celgard 2325 and C480 separators in pouch and Cu-block measurement setups wetted with LP572. The areal resistance scales linearly with the number of separators, as one would expect. Right: Tortuosity calculated from ionic resistance versus electrolyte conductivity for Celgard 2325 separator in Cu-Block setup. Electrolytes: EC:DEC 1:1 (wt.%) with 0.5 or 1 M LiClO4 and EC:EMC 3:7 (wt.%) with 1 M LiPF6,

4.2.2. Ionic resistance of electrodes in a symmetric cell

Another application of impedance spectroscopy is to measure the TLM response of electrodes. Results of such a measurement with graphite electrodes (thickness 63 µm, porosity 0.42 ± 0.02) are shown in figure 4.8, corresponding closely to the theoretical curve which is expected for the TLM model in blocking conditions (compare figure 4.5). Blocking conditions are realized here by using a non-intercalating electrolyte with $TBAClO_4$ salt, as discussed in section 4.1.

The electrodes are measured in symmetric cells which consist of similar electrodes. Here, we basically measure the transmission line model of figure 4.4 twice with some electrolyte and separator in the middle. All relations are still valid, except that we measure the resistance of both electrodes. If the electrodes are essentially identical, we can just divide the measured resistance, e. g. R_{ion} by two to get the respective single electrode value. So, in the measurement of figure 4.8 the length of the TLM-45°branch is actually $2/3R_{\text{ion}}$ when referring to the single electrode ionic resistance. Again, we can change the conductivity of the electrolyte to study the change in impedance and to check the sensitivity of e. g. the tortuosity which is calculated from the measured ionic resistance R_{ion}. The concentration of the salt in the electrolyte allows to tune the conductivity; here the following was used: EC:DMC 1:1 (wt.%) with 10, 50, 200 or 700 mM of TBAClO$_4$ with a conductivity of 0.46, 1.74, 5.22 and 9.56 mS/cm, respectively. As one can see in figure 4.8 (left), the length of the TLM-branch scales drastically with conductivity, which reflects the change in ionic resistance as expected. A small conductivity results in high ionic resistance which can be measured easily. Also, the ionic resistance of the separator and accordingly the HFR and beginning of the TLM curve shifts with conductivity. From equation 4.7, we can calculate the independent transport property of the electrode which is expressed by the tortuosity τ. The four measurements yield tortuosity values in the range from 4.1 to 5.1 with an error range of ±0.3. So the method is indeed able to measure the tortuosity over a relatively large range of conductivity.

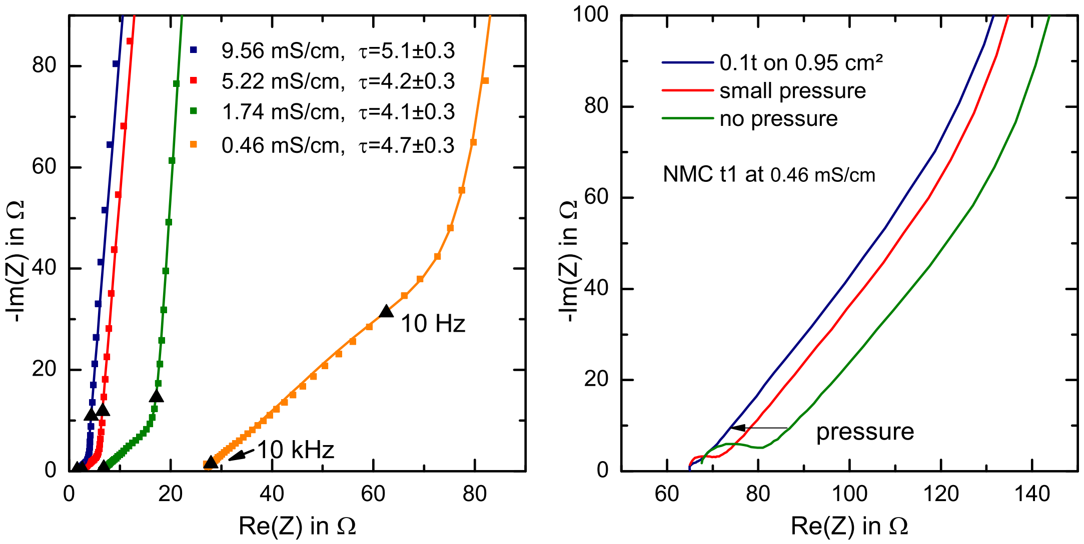

Figure 4.8.: Left: Varying the electrolyte conductivity in symmetric pouch cells with similar graphite electrodes (thickness 63 µm, porosity 0.42 ± 0.02) in EC:DMC 1:1 (wt%) with 10, 50, 200 or 700 mM TBAClO$_4$. Area is ca. 2.3 cm^2, Celgard 2325 separator. Right: Applying pressure to an NMC symmetric T-cell reduces the pseudo-RC-behavior from contact resistance in the TLM measurement (10 mM TBAClO$_4$). Area is 0.95 cm^2.

4.2.3. Validity of the TLM model

HFR and ionic resistance can be measured easily with impedance spectroscopy methods. But some care has to be taken when one wants to measure RC-elements or the associated resistances. Unfortunately RC-elements describe all sorts of processes such as charge transfer at surfaces (anode and cathode) and also contact resistances as already mentioned [43]. Especially in NMC electrodes, contact resistance may disturb a TLM measurement. Figure 4.8 (right) shows a semi-circle at high frequencies which apparently stems from contact resistance, as it vanishes by applying pressure. A pressure of 10^7 Pa (0.1 tons on electrode area) is enough to eliminate the contact resistance and to measure the pure TLM behavior. This pressure is still a factor of 10 below the pressure which was used for compacting the electrodes during manufacture so that we can neglect any change in thickness or porosity. Therefore, NMC electrodes were generally measured under the moderate pressure of 10^7 Pa.

Another thing to keep in mind is, that the TLM model neglects electronic resistances in the solid phase of the electrode. For electrolytes with relatively high conductivity and cathodes with low content of carbon black this assumptions might not hold true anymore. In the Nyquist diagram, an increase in solid resistance will be seen as a shift of the curve to the right since there is an additional ohmic contribution in the solid. The HFR will increase and the length of the 45° branch will decrease, in the extreme case to half of its original size when solid and liquid resistance values are equal. The shape of the curve will remain very similar to the pure TLM so that this error is not easy to detect. A simple countermeasure is to check the HFR resistance which should not be above the value measured for the separator individually. Another technique is to make the difference in conductivities between liquid and solid as big as possible, e. g. by using low conductive electrolyte as applied in this work.

4.2.4. Study of electrodes with varied thickness

As we have discussed in the sections above, battery and electrode properties are often measured by impedance techniques. These techniques are sometimes challenging to interpret but, if done right, can help to assess the performance of cells and electrodes. Here, we want to compare ohmic and ionic as well as charge transfer resistances which are derived from PEIS measurements, with cycling results in coin cells. The motivation is to understand the limitations of electrodes in order to optimize a cell design for high energy density and/or high performance. A key to increase energy density on the battery cell level is to increase the share of active material in relation to the inactive metal foils and separator by increasing the electrode coating thickness. The thickness is however limited by the difficulty of

transport through thick electrodes, so that the power to energy ratio goes down [49] and the energy cannot be delivered at higher C-rates. This is the reason why high power cells typically have thinner electrodes.
Here, graphite and NMC-111 electrodes were prepared with four different thicknesses and tested in half cells vs. Li and in symmetric cells for PEIS. The experiments were all done at 25±0.5° C and with at least two cells ($n = 2$) in each condition. We report the mean value of these cells and give a sample standard deviation $s = \sqrt{\sum_{\mathrm{i}}^{\mathrm{n}}((x_{\mathrm{i}} - \bar{x})^2/(n-1))}$ which is plotted as error bar. Note that the standard error of the mean is smaller by a factor of $\sqrt{n}$, but for our small n the chosen visualization with sample standard deviation might better represent the level of variation in the data. Simple error propagation was used to give the error bars of calculated quantities accordingly; all other error influences were neglected (compare also appendix A.4). In detail, the test protocol was as following:

1. Cycling of electrodes vs. Li in coin cells:
   Coin cells with glass-fiber separators and LP572 electrolyte were assembled. A rate test was done with 25 to 30 cycles and increasing discharge currents from 0.1C to 10C (charge was with an equally low rate or maximum 1C and a subsequent CV phase until a cut-off of C/20), followed by 10 cycles at 1C. Here, discharge refers to the condition a given electrode would experience in a full cell. So graphite saw the high rates during delithiation and NMC saw the high rates during lithiation. NMC was cycled from 3 to 4.3 V and graphite from 0.01 V to 1.5 V.

2. Non-blocking PEIS of symmetric cell from harvested electrodes:
   Two electrodes were taken out at 50% SoC from the half cell and built into a symmetric cell (Swagelok) with LP572 electrolyte. PEIS was measured with an amplitude of V=± 5 to 25 mV.

3. Blocking PEIS of symmetric cell with fresh electrodes:
   Two fresh electrodes were assembled into a symmetric cell (Swagelok) and electrolyte with 10 mM $\mathrm{TBAClO_4}$ as salt was added. PEIS was measured with an amplitude of V=± 5 to 25 mV.

4.2.5. Thickness variation results for NMC-111

The prepared NMC electrodes with coating thicknesses of t0=17, t1=35, t2=84 and t3=127 µm were cycled vs. Li in a coin cell. Accordingly, the areal capacity varied from 0.7, 1.5, 3.5 to 5.1 mAh/cm^2 and the porosity was ca. 0.34 for all electrodes after calendering. Figure 4.9 shows images of the cross section of the electrodes obtained by SEM. The samples were prepared by vacuum casting the electrode with a resin and subsequent polishing. The Al foil and the coating with active particles and a conductive binder matrix can be identified. For the thinnest coating the thickness is smaller than the biggest active particles so that the film is very inhomogeneous.

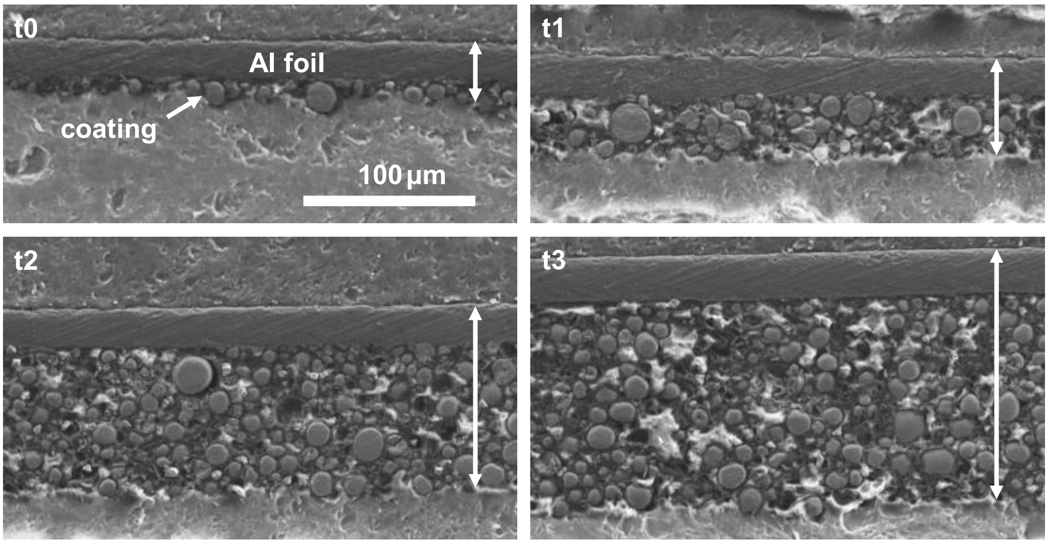

Figure 4.9.: Cross section SEM images of the NMC-111 coatings with increasing thickness.

In figure 4.10 (left) the specific discharged capacity in mAh per gram cathode active material is shown vs. the number of cycles. At low rates the theoretically expected specific capacity of NMC-111 of 156 mAh/g is nearly reached. At higher rates less capacity can be discharged as expected and this effect is greater for thick electrodes. Already at 1C the thin electrode t0 delivers still 142 mAh/g whereas the thickest electrode t3 can only support 80 mAh/g (taking the last of the three cycles of a rate step for comparison). Above 3C the thick electrodes are practically unable to deliver any capacity whereas the thin sample performs well up to 10C where it can still deliver two thirds of the nominal capacity. Here, we have focused on discharge or NMC lithiation and increased this rate up to 10C, due to the long CV phase before we can be sure that charge (at max. 1C) is not limiting. Even though the CV phase was limited in this case to one hour, a detailed analysis of the charge and discharge capacities of subsequent cycles confirms that the major limitations stem from NMC lithiation resp. discharge as intended by the test protocol. Furthermore, cycling at 1C after the rate test (cycle 27 ff.) shows that all electrodes return to the same capacity value which was measured at 1C before. This confirms that no cyclic or calendaric aging is superimposed in the rate test data. Prolonged cycling at 1C or higher rates could however introduce aging which can also be more severe for higher thickness as indicated by the drop in capacity of the last cycles for t3, but aging is not in our focus and neglected here. In summary, the thick electrodes perform worse but does this already mean that thick electrodes are worse at the same current density (in mA/cm^2)?

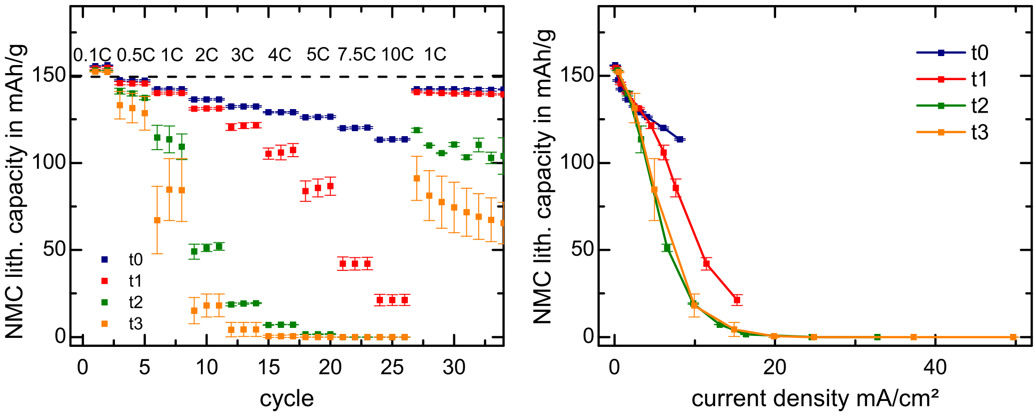

Figure 4.10.: Left: Specific lithiation capacity of NMC-111 electrodes vs. cycles during rate test. Electrode thickness increasing from t0=17, t1=35, t2=84 and t3=127 µm. Corresponding to areal capacities of 0.7, 1.5, 3.5 and 5.1 mAh/cm^2. Right: Specific lithiation capacity of NMC-111 electrodes vs. current density during rate test. Mean values and sample standard deviation of two cells per condition.

C-rate is defined by the electrode capacity, and a higher thickness and thus higher loading means higher capacity. So thick electrodes face much higher current densities in mA/cm^2 (per electrode surface). Therefore, limitations in the separator or the external wiring could play a more important role here. These ohmic contributions should all be linear in current density. Figure 4.10 (right) shows the discharge resp. lithiation capacity vs. current density. First, one can see that for current densities above 40 mA/cm^2 no charge can be extracted. Second, the thick electrodes achieve worse capacities in comparison, e. g. around a current density of 10 mA/cm^2, thin electrodes achieve 110 mAh/g whereas the thick electrodes are around 20 mAh/g. So even if we consider the current density effect, the thick electrodes are limited in performance by another mechanism. The higher current density could also contribute to the more severe aging for the higher thickness material.

Theses results for NMC-111 half cells are in line with results of Zheng et al. for LFP, NMC-111 with 24 to 108 µm particle size [60] and Gallagher et al. for NMC-622 with 70 to 175 µm [64]. Figure 4.11 (left) gives an overview of all data points, here plotted as capacity per area (simple electrode area facing the separator) vs. current density. One can see that higher mass loadings yield higher achievable areal capacities for low currents but loose dramatically at higher currents between

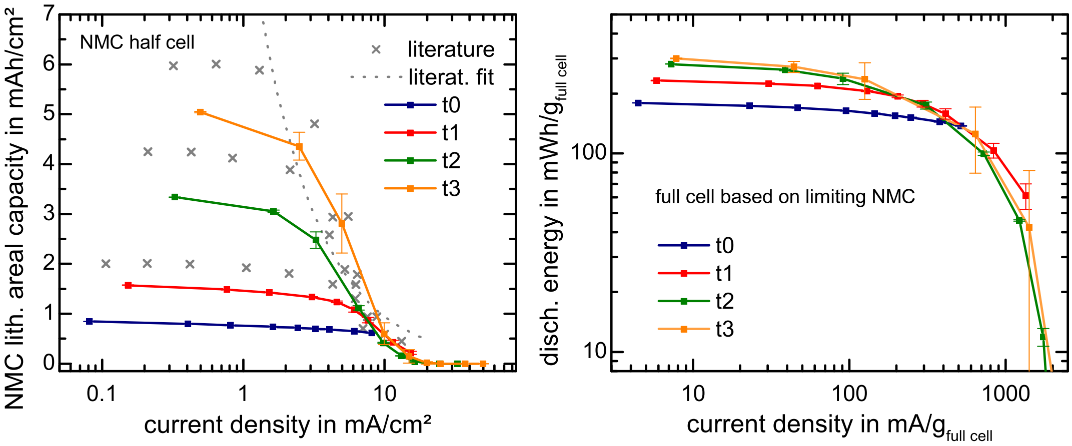

Figure 4.11.: Left: Specific lithiation capacity of NMC electrodes per electrode area vs. current density with comparison to literature data points and literature fit $\propto 1/\sqrt{I}$ [60, 64] in the region of decrease around 5 to 10 mA/cm^2. Right: Ragone plot showing the discharge energy vs. current density for a theoretical full cell, calculated from NMC half cell data. Details in appendix A.3.

3 and 10 mA/cm^2. The curves follow a typical S-shape and the lower part, i. e. the region of critical current can be fitted to a function that is proportional to one over the square root of current ($1/\sqrt{I}$) which is proportional to the square root of time of discharge and can indeed be derived from theory with electrolyte polarization and limited diffusion as the root cause [64]. The usefulness of such a fit function is however limited because the tortuosity τ is an input parameter which has to be determined first. The region at low rates is traditionally fitted by the empirical Peukert law [83] but is not of interest here. From the half cell results, we can estimate a Ragone plot for a full cell where the NMC cathode is limiting. We assume about 9 mg inactive mass per cm^2 plus some electrolyte in the pores of the electrodes. Details are given in appendix A.3. The Ragone plot in figure 4.11 (right) shows how thin coatings perform better (i. e. they yield more energy) for very high current densities or equivalently power requirements. Here, the second last and the last data point of coating t1 perform best at high rates. The axes, i. e. capacity (mileage in a car) and current density (power) are normalized to total full cell weight (alternatively liter) which is the most important criterion in many applications.

As we have seen above, overvoltages of various origin drive the cell potential off the thermodynamic equilibrium and limit the performance of a battery. Figure 4.12 shows how the potential curve is shifted during the rate test for thin and thick electrodes. At 0.1C both electrodes follow almost the same curve and reach the lower cut-off voltage at a capacity of well above 150 mAh/g. At higher rates two distortions can be observed. First, there is an instantaneous drop in potential after the start of lithiation resp. discharge at 4.3 V, due to the ohmic or so called IR drop. It represents all ohmic contributions (electronic and ionic resistances) throughout the cell. Since the switching is not infinitely fast and the first data point is collected after 40 to 200 ms, this resistance is the real part of the impedance vector at an equivalent frequency of 5 to 25 Hz. So there are some contributions which are not purely ohmic (when we define ohmic as resistance above 100 kHz as in a typical PEIS experiment). We can see that at 1C this drop is bigger for the thick electrode, so there are some additional resistances above 5 to 25 Hz.

At very long time scales, i. e. minutes and hours as the NMC lithiation resp. discharge moves along, a second effect is observed. The potential curve is pushed down even further during cycling. At 1C this overvoltage drives down the curve strongly, so that at little over 70 mAh/g cut-off is reached. This dynamic overvoltage is obviously the cause for the bad performance of the thick electrode. As already stated before, it is typically associated with concentration polarization in the electrolyte after prolonged polarization during cycling. Transport limitation in the solid active material cannot play the main role here as the achieved capacity vs. current density (correctly scaled to mA/cm^2) would then depend on active particle size rather than on coating thickness.

To be fair, we have to adjust again for loading and compare the overvoltage contributions at the basis of current density. In figure 4.13 the IR drop of the first data point is shown vs. current density. Note, that this measurement includes the Li counter electrode. The data points of all four thicknesses follow a linear behavior, so this is indeed an ohmic resistance which is given by the slope of the curve. If estimated from the $\Delta U/I$ data point at 10 mA/cm^2 we get ohmic resistances of 72, 70, 50 and 33 Ω (area 1.54 cm^2). The drop from t3 to t0 is 54% which is less than the difference in capacity at the same current density in figure 4.10 (right) which is 84%.

In summary, the IR drop is one aspect why discharged capacity goes down with higher current densities in figure 4.10, but it does not explain the non-linear drop for higher current densities nor does it explain the drop for higher thicknesses t2 and t3 completely. The discharge curve of figure 4.12 is not just shifted downwards by the constant amount of the IR drop but it is shifted down by an overvoltage which is increasing during discharging resp. NMC lithiation.

In order to get a better understanding of the origin of the overvoltages, we want to compare resistances from time space measurements such as the IR drop, with impedance measurements in frequency space. PEIS measurements yield the complete impedance at all frequencies and not just one data point as the IR drop evaluation which is a typical pulse measurement. Furthermore any artifacts or con-

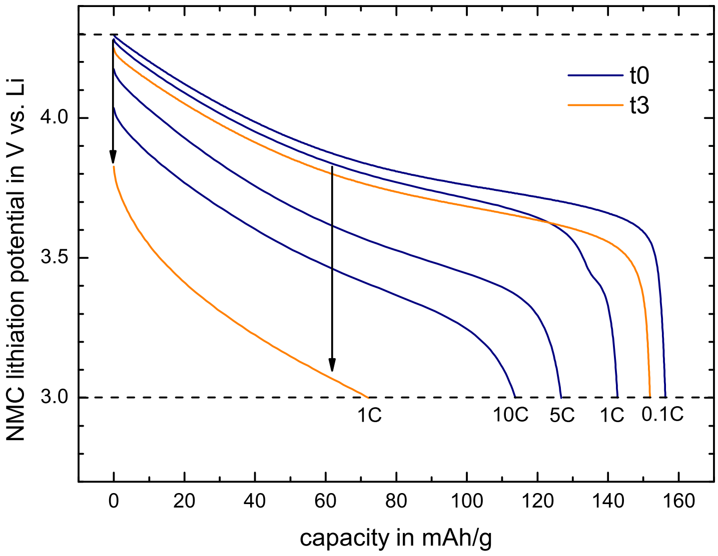

Figure 4.12.: Potential vs. capacity of NMC electrode vs. Li during discharge, i. e. lithiation for thinnest and thickest electrode. For t3, rates above 1C are omitted because they drop instantaneously to the lower cut-off potential. Upper and lower cut-off potentials are marked by the dashed lines.

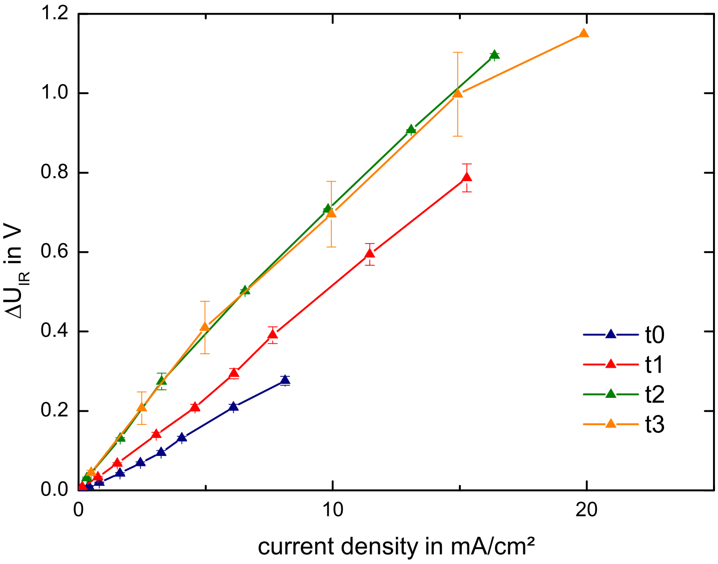

Figure 4.13.: IR drop upon first data point (i. e. at 5 to 25 Hz) taken during the discharge as a function of current density for all NMC electrodes in half cells vs. Li.

tributions from the Li counter electrode are avoided when measuring impedance in symmetric cells with similar electrodes on both sides. In such a cell the measured impedance values have to be divided by a factor of 2 to get the single electrode value.

Figure 4.14 (left) shows a Nyquist plot of the data from symmetric cells with LP572 electrolyte and harvested electrodes at 50% SoC. Being at this SoC and using standard Li-salt containing electrolyte, we can be sure to be in faradaic conditions where intercalation is possible. In the experiment, a typical RC-like semi-circle is observed which extends to data points with a frequency of below 0.1 Hz, and not the whole semi-circle is covered by the measurement. As expected the width of the semi-circle, which is a measure of the charge transfer resistance, decreases with thickness because the total surface of active material increases for higher loadings. Dividing the measured values by 2 yields a characteristic charge transfer resistance R_t for one electrode. The order of magnitude of transfer resistance is in line with measurements of similar cathode materials [49]. The relevant area in all impedance measurements is $0.95\,\mathrm{cm}^2$ from the Swagelok cell setup, so the specific resistance in $\Omega\,\mathrm{cm}^2$ is of the same order of magnitude for all the following measurements and not explicitly calculated. The charge transfer resistance R_t was fitted with a faradaic TLM model in MATLAB following equation 4.13. Further details are given in appendix A.1.

From the faradaic TLM measurement, the ionic resistance can in principle be fitted, but the length of the 45° branch is limited to very few data points and very small compared to the charge transfer resistance, so that fitted values for ionic resistance are not very reliable. A better approach is to measure the ionic resistance separately in true blocking conditions. Figure 4.14 (right) shows data from symmetric cells with electrolyte with 10 mM $\mathrm{TBAClO_4}$ salt and pristine, i. e. lithiated NMC electrodes. The data follow nicely the blocking TLM behavior as given by equation 4.11. The choice of an electrolyte with low conductivity results in large resistance values that can be measured easily. From the data we see that the ionic resistance is increasing with coating thickness. The HFR of the separator is more or less the same for all samples, as it is given by the electrolyte and separator properties and only mildly changed by compression of the glass-fiber separator.

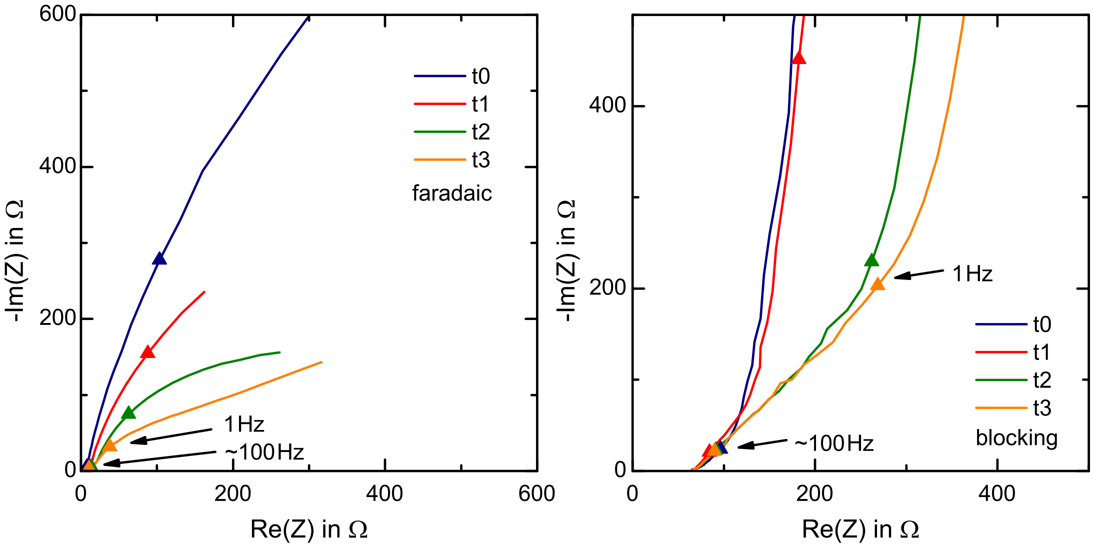

Figure 4.14.: Left: Data from symmetric cells with LP572 electrolyte and harvested NMC electrodes of equal thickness. The relevant area is 0.95 cm^2, so specific resistance in Ω cm^2 is of the same order. The charge transfer resistance R_t is decreasing for thicker electrodes and can by fitted with a faradaic TLM model. Right: Data from symmetric cells with 10 mM TBAClO$_4$ based electrolyte and pristine NMC electrodes, area is 0.95 cm^2. R_ion can be fitted with a blocking TLM model or estimated from the difference (2/3) of LFR and HFR values.

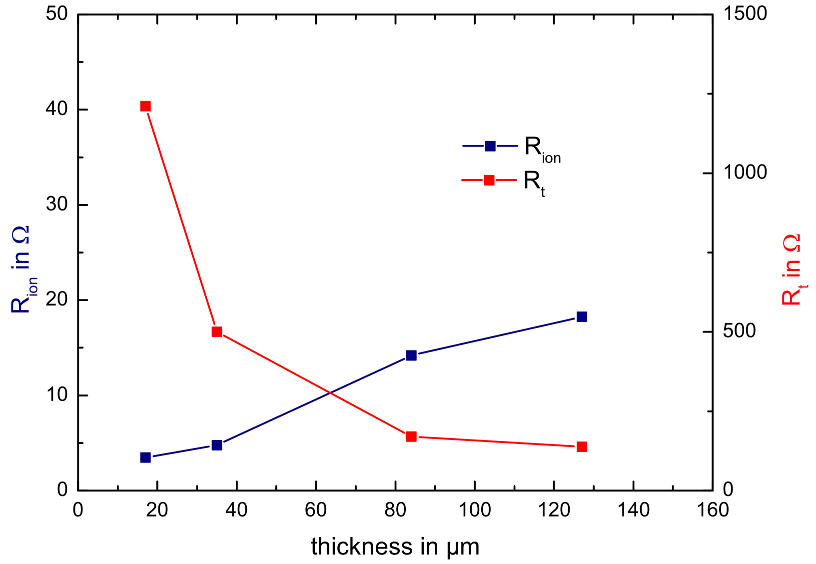

Figure 4.15.: Resistances R_t (harvested electrodes in faradaic condition) and R_ion (fresh electrodes in blocking condition) from MATLAB fit, all values are adjusted to the conductivity of LP572, area is $0.95\,\mathrm{cm}^2$.

The fitted values for R_t (from faradaic TLM) and R_ion (from blocking TLM) are shown in figure 4.15. The resistance data from blocking condition were adjusted to the higher conductivity of LP572 by multiplying with $\kappa_\mathrm{TBAClO4}/\kappa_\mathrm{LP572}$, so that all resistances can be compared. The ionic resistance of the pore network is increasing linearly with thickness as one would expect also from equation 4.7. The charge transfer resistance in faradaic conditions scales roughly with $1/t$ because it is inversely proportional to active surface area which in turn scales approximately linearly with coating thickness.

4.2.6. Thickness variation results for graphite

For the anode material graphite a similar study as for NMC was done. Again, electrodes with a range of coating thicknesses of t0=11, t1=29, t2=60 and t3=89 µm were produced and cycled vs. Li in a coin cell. The loadings were accordingly increasing from 0.7, 1.7, 3.1 to 4.5 mAh/cm^2. Porosity was chosen comparable to NMC with around 0.34 after calendering. Figure 4.16 shows the cross sections of the electrodes which are all quite aligned and homogeneous.

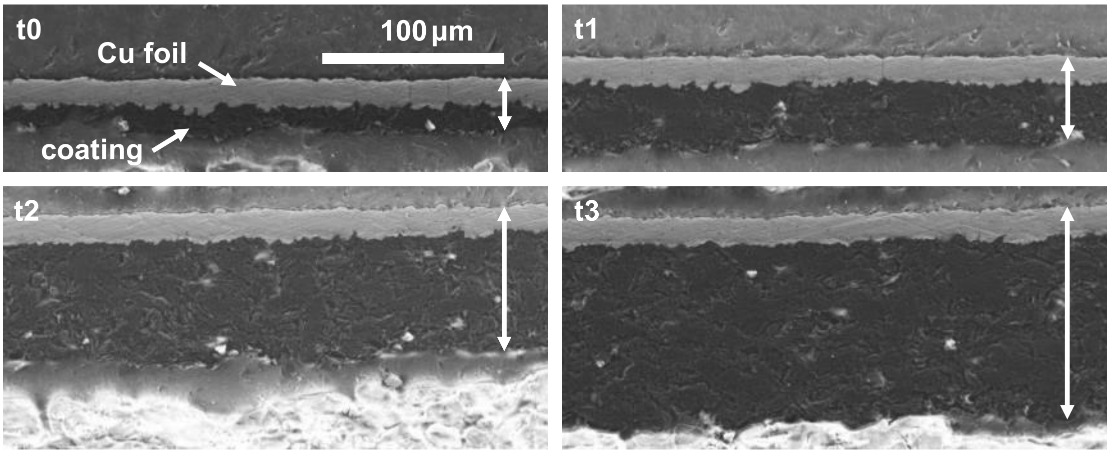

Figure 4.16.: Cross section SEM images of the graphite coatings with increasing thickness.

Figure 4.17 (left) shows the specific half cell charge (corresponding to full cell discharge), i. e. graphite delithiation capacity in mAh per gram active material vs. the number of cycles. Note, that here we focus on charge in the half cell which is delithiation of graphite which in turn is discharge in a full cell vs. a standard cathode material. So again, we aim at limitations in the discharge in a practical application as for NMC. Here, a very long CV phase at 0.01 V made sure that the delithiation capacity is not limited by the previous lithiation capacity. Figure 4.17 shows that the theoretically expected capacity of 372 mAh/g (indicated by the dashed line) is almost reached for all thicknesses at low rates like 0.1C. Graphite can in general support higher rates than NMC, so at 1C the thin electrode t0 is still near 372 mAh/g and even at 10C it can support 361 mAh/g. But thicker electrodes are worse and show the typical performance loss with thickness. The thickest electrode t3 drops to 317 mAh/g at 1C and further to 12 mAh/g at 10C. Cycling at 1C after the rate test shows that all electrodes return to their initial capacity values at 1C which proves that aging does not influence the rate measurement.
This holds true even after we have corrected for the effect of increased loading in figure 4.17 (right) where charge or delithiation capacity is plotted against current

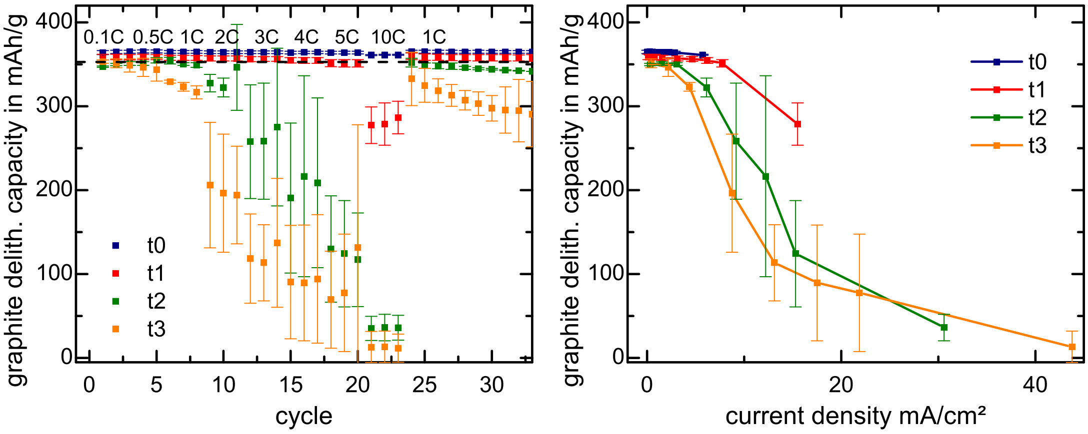

Figure 4.17.: Left: Specific delithiation capacity of graphite electrodes vs. cycles during rate test. Electrode thicknesses of t0=11, t1=29, t2=60 and t3=89 µm. Corresponding to areal capacities of 0.7, 1.7, 3.1 and 4.5 mAh/cm^2. Right: Specific delithiation capacity of graphite electrodes vs. current density during rate test.

density. The thick electrodes are still much worse than the thinner ones, e. g. at current densities of 15 mA/cm^2. The error bars in both figures are relatively large because the rapid cycling of graphite in half cells vs. Li is very sensitive towards lithium plating. Dendrites of plated lithium cause changes in the internal resistance or even small short-circuits in the half cell which lead to characteristic spikes in the potential curve and disturb the capacity measurement, compare also section 5.3.3. The spikes in the potential curve are e. g. visible in figure 4.19 for higher rates. Figure 4.18 shows that graphite exhibits the same behavior in the areal capacity vs. current density plot with the same S-shaped drop in performance as NMC, though at a higher level with critical current densities of 5 to 12 mA/cm^2. The assumption that full cell discharge is limited by NMC is therefore valid.

The potential curves of figure 4.19 are plotted against charge or delithiation capacity. The low-rate curves show the three major graphite potential plateaus which indicate the coexistence of two phases. More details on the phases are also given in section 5.1. At higher rates the potential curve is shifted upwards and the plateaus are smeared out. There are basically three overvoltage phenomena. The first overvoltage contribution is only present at higher rates and is a potential overshoot just at the beginning of charge. E. g. this overshoot drives the potential of the thin electrode to 0.5 V at 10C but declines rapidly to a steady value after 20 mAh/g or so. Such a behavior is characteristic for the Li counter electrode where we change from stripping to plating. This effect can be demonstrated also in a Li/Li cell. The second overpotential is after the initial overshoot at a capacity

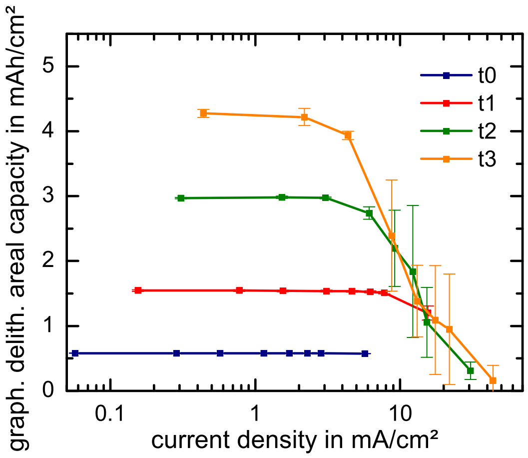

Figure 4.18.: Specific delithiation capacity of graphite electrodes per electrode area vs. current density.

of around 25 mAh/g indicated by the first black arrow which represents a delta of 0.13 V. This is what we would attribute to the ohmic contributions on the graphite electrode side and in the separator. This overvoltage increases with higher rates and higher loading. Finally, the third overpotential is marked by the second black arrow above 200 mAh/g which represents a higher delta of 0.21 V, an increase by about 60%. It is the ohmic overpotential plus the additional overpotential contributions from polarization in the electrolyte and material. For higher rates of 5C and 10C for the thick electrode, the polarization drives the overpotential up dramatically, so that the typical graphite plateau vanishes completely and the upper cut-off is reached very early. Since this effect increases dramatically with coating thickness, we conclude again, that the liquid electrolyte phase is the main bottleneck, not the transport in the solid.

Figure 4.20 shows the graphite IR drop vs. current density. The initial overshoot is excluded here, so ΔU is measured from the start at 0.01 V to the potential level of the first stable plateau resp. the potential minimum after the overshoot. Again, the potential drop is a linear function of the current density and represents thus an ohmic resistance. This specific resistance is of the order of 40 Ωcm^2 (0.8 V divided by 0.02 A/cm^2) and similar for all electrode thicknesses. Obviously, the good electric conductivity of the active material ensures that there is no contact resistance problem depending on the quality or thickness of the coating film. Here, it is very obvious that the non-linear drop in capacity for higher rates and thicker electrodes does not stem only from ohmic resistances, no matter if electric or ionic.

To gain further insight, we can use the PEIS methods to actually measure the ohmic resistances in the system. Figure 4.21 shows PEIS data from symmetric

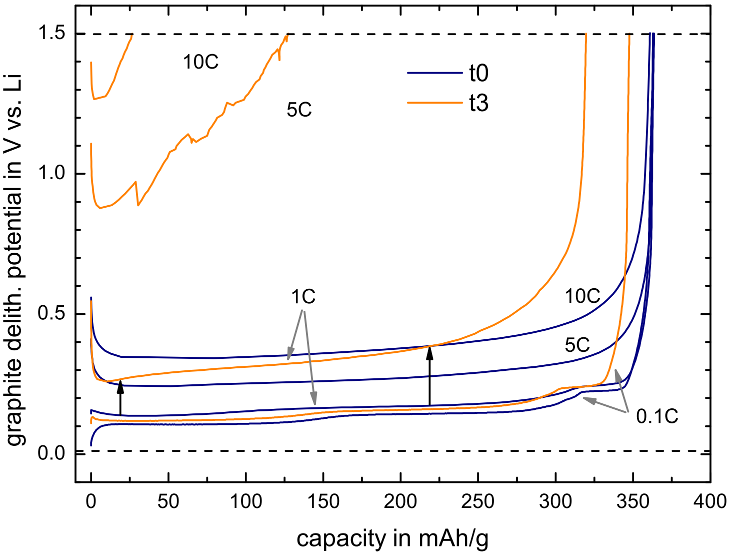

Figure 4.19.: Potential vs. capacity of graphite electrode vs. Li during half cell charge, i. e. graphite delithiation for thinnest and thickest electrode.

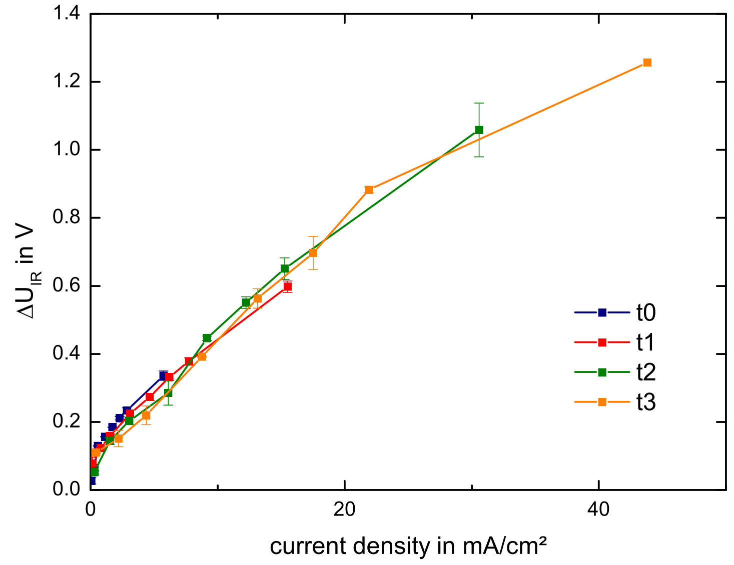

Figure 4.20.: IR drop from the initial potential difference but without the overshoot, data taken during delithiation as a function of current density for all graphite electrodes in half cells vs. Li.

cells with harvested graphite electrodes which were at 50% SoC. The general trend is similar to NMC: starting from the HFR of the separator at high frequencies, an RC-semi-circle is visible at lower frequencies and finally a Warburg diffusion tail. Again, the diameter of the semi-circle which is a measure of the charge transfer resistance decreases with the overall surface of active material and thus with coating thickness. R_t can be easily fitted with the faradaic TLM model. At high frequencies, even the start of a 45° slope from the faradaic TLM model can be seen, but again it is hard to fit any ionic resistance from the faradaic TLM model.

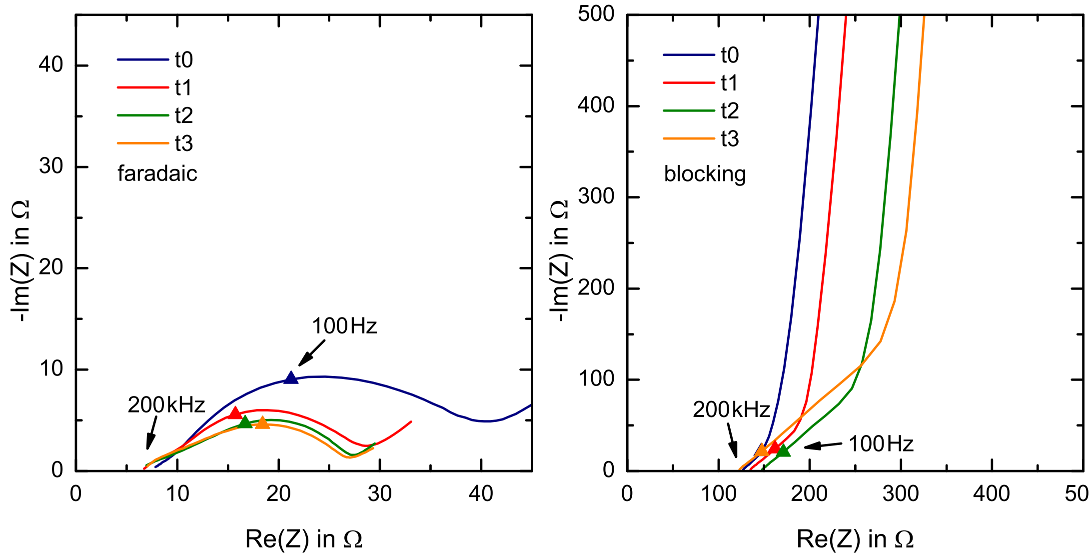

Figure 4.21.: Left: Data from symmetric cells with LP572 electrolyte and harvested graphite electrodes of equal thickness, area is $0.95\,\mathrm{cm}^2$. R_t is decreasing for thicker electrodes and can by fitted with a faradaic TLM model. Right: Data from symmetric cells with 10 mM $\mathrm{TBAClO_4}$ based electrolyte and pristine graphite electrodes, area is $0.95\,\mathrm{cm}^2$. R_ion can be fitted with a blocking TLM model or estimated from the difference (2/3) of LFR and HFR values.

In order to determine the ionic resistance, we turn to the symmetric cells filled with $\mathrm{TBAClO_4}$ based electrolyte which are in blocking conditions as seen in figure 4.21 (right). The curves follow nicely the expected blocking TLM behavior with an initial 45° slope and a capacitive low frequency branch. Due to the varying pressure of the cell assembly which was done by hand in the glove box, the glass-fiber separator was compressed differently from cell to cell which is reflected by the changing HFR at the start of the curves at very high frequencies. Since we are only interested in the differences in HFR and LFR, this absolute shift can be neglected. The difference of HFR and LFR, resp. the inclination point scales with thickness. So does the ionic resistance R_{ion} which is 2/3 of this difference.

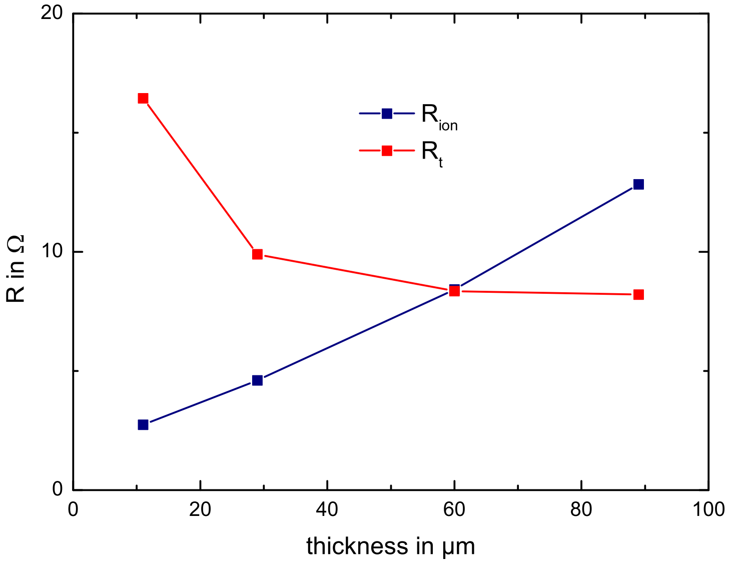

Figure 4.22.: Resistances R_{t} (harvested electrodes in faradaic condition) and R_{ion} (fresh electrodes in blocking condition) from MATLAB fit, all values are adjusted to the conductivity of LP572, area is 0.95 cm^2 for both.

The fitted values for R_{t} and R_{ion} for the graphite electrodes are shown in figure 4.22. The resistance from the blocking condition measurement has been adjusted to be comparable to the measurement with LP572 electrolyte with much higher conductivity. Again, the ionic resistance is increasing linearly with thickness. At low thicknesses $t < 30\,\mu\mathrm{m}$, the charge transfer resistance is also scaling with $1/t$, as before, inversely proportional to the overall active surface. At larger thickness however, higher resistances than expected are observed. The extrapolation of the $1/t$ rule from the first data point (11 µm, 16.5 Ω) would yield values of approx. 2 Ω at 89 µm, whereas (89 µm, 8.2 Ω) is observed. A possible reason is that the extra surface in the thicker electrode is not accessible in the cycled cells. Graphite is softer than NMC and the compacting of thick electrodes might block some pores in the electrode so that a part of the surface is not accessible for charge transfer anymore. Indeed, figure 4.17 shows that for thick electrodes only 350 mAh/g and not 365 mAh/g as for the thin electrodes are reached, even at low current densities. This is another hint, that some areas are (ionically) not connected in the cycled cells. The measurement of ionic resistance which should also reflect the number of connected of pores, is simply proportional to thickness; the last data point seems to be a little bit higher than the linear trend, but small deviations are not so obvious for this linear dependence. Furthermore, the ionic resistance was measured with fresh electrodes.

4.2.7. Measured tortuosities and conclusion

So we have measured different resistances which characterize the electrodes, but can we already explain quantitatively the non-linear drop in performance? In the literature, Ogihara et al. [49] and Illig et al. [32, 51] have used resistance values which were obtained from TLM impedance measurements or from half cell impedance to discuss transport properties and also performance of electrodes.

Of course, ionic and transfer resistance play a significant role in electrode performance. Both contribute to the observed (near ohmic) IR drop which is observed at frequencies from 5 to 25 Hz (for NMC, but without overshoot probably also for graphite). Yet for all impedance measurements the time scale is limited to some mHz (e. g. 100 mHz in the measurements shown above) and the measured resistances reflect only the state of the electrode upon beginning of charge or discharge. Furthermore, impedance measurements may include geometric artifacts and contributions from counter electrodes. Dependence on SoC and temperature as well as misleading contact resistances complicate the easy interpretation of impedance spectra further.

Besides, a continuous cycling experiment is different from a short impedance measurement, a real cell is (dis-)charged continuously in hours or minutes and other effects such as polarization may limit transport and affect the electrode performance. Polarization, e. g. an unequilibrated distribution of charge or also species, can happen both in the electrolyte where the concentration of the conductive salt forms a gradient and in the solid active materials where Li ions are distributed unequally. An overvoltage associated with a concentration gradient in the solid should however not vary with coating thickness and does thus not explain the above rate limitations.

The detailed behavior and performance of the battery electrode can only be estimated by setting up a full porous-electrode model with the governing differential equations [39]. One of the most important input parameters which accounts for the geometrical properties of the porous material is the tortuosity τ. From the blocking TLM measurement, the ionic resistance can be determined very precisely. Since conductivity, thickness and porosity as well as area are known, we can calculate the tortuosity directly from equation 4.7. So instead of using statically measured resistances to somehow deduce dynamic cycling performance, it is better to use a blocking TLM measurement to actually measure the input parameter τ for a precise numerical simulation of electrode performance.

The tortuosities calculated from the above blocking TLM measurements of graphite and NMC are shown in figure 4.23 (left) vs. thickness and in figure 4.23 (right) vs.

porosity. For homogeneous coatings which are thicker than the primary particle size and where percolation effects do not play a role, we would expect τ to be independent of coating thickness. Indeed, the data shows that the tortuosity is more or less constant for both active materials. For NMC we get a mean tortuosity of $\tau = 4.6 \pm 0.8$ and for graphite a mean of $\tau = 4.3 \pm 0.6$. Both values are significantly higher than the Bruggeman estimate for a porosity of 0.34 which is $\tau = 0.34^{-0.5} = 1.7$. The Bruggeman equation quantifies how the tortuosity increases with lower porosity. This qualitative behavior has also been confirmed experimentally [54, 80] and discussed in the literature given above, where the negative exponent is however larger than the $\alpha = 0.5$ of the Bruggeman assumption in equation 4.6. Here, the aim was to measure at comparable electrode porosities so that the data of figure 4.23 (right) spans only a limited porosity range where no fit of α is done. The error bars in the figure give an impression of what tolerance can be achieved in a manual production process as it was the case here. Note that the relative error is high for thin electrodes where e. g. NMC electrodes have an average thickness which is not much bigger than individual particles and hard to measure. Furthermore, each data point represents the superposition of an impedance measurement of two individual (though carefully selected) electrodes which have a remaining variation. We would expect less scatter for high quality commercial electrodes. The variation in any production process and the variety of influence parameters such as material type, recipe, mixing, coating, drying, calendering and cell setup limits the significance of comparing obtained tortuosity values to literature values, but a rough estimation can be done.

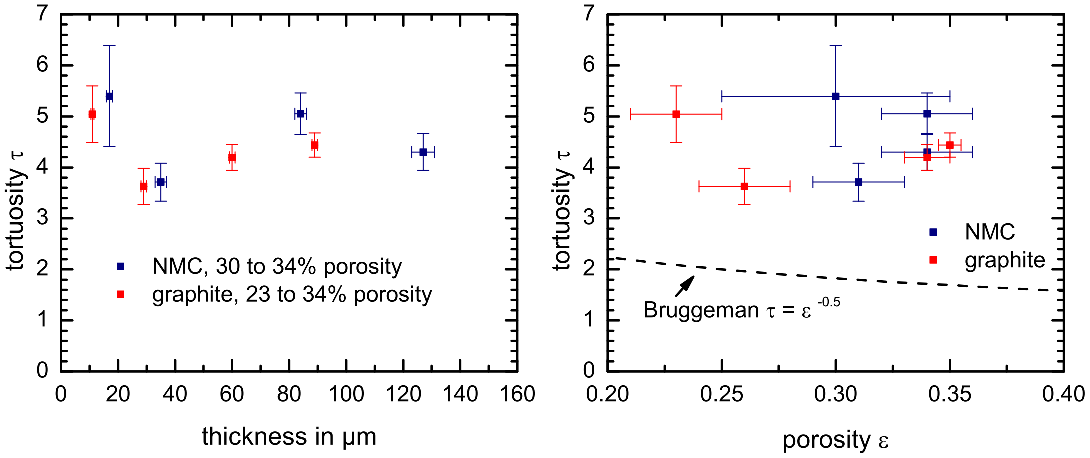

Figure 4.23.: Electrode tortuosity calculated from blocking TLM (from R_{ion}) vs. electrode thickness (left) and porosity (right), results for graphite and NMC.

For NMC, Ebner at al. reconstruct tortuosity values of around 2 at 33% porosity

[76] (calculated from $\epsilon^{-\alpha}$) from tomography which are probably not directly comparable to electrochemically measured impedance values due to bottleneck and surface chemistry effects. In a previous study [54] we measured NMC electrodes with tortuosities of around 3.8 at 0.33% porosity. This is a little lower than the above obtained 4.6 but still within the error bars and remaining differences due to different preparation.

Tortuosity of a graphite electrode was e. g. measured by DuBeshter et al. [72] who obtain $\tau = 3.7$ at 22% porosity with a gas diffusion method. Ebner et al. reconstruct tortuosities between 2 to 10 in parallel and perpendicular direction to the electrode foil for flaky graphite at 33% porosity. The dependence of tortuosity on particle shape and orientation was also highlighted in the work by Cericola and Spahr [80] who measured electrodes made of a variety of graphite types. Tortuosity at 33% porosity was found to vary from $\tau = 17.8$ for ultra flaky to around 8 for flaky to 3.6 for mild-round graphite particle morphology. For potato-shaped graphite, we measured a tortuosity of 5.4 previously. The value of 4.3 obtained here lies within reasonable deviation from the two latter measurements, again considering the variety of factors that influence the tortuosity of a real manually prepared electrode.

In conclusion, we have shown cycling data and performance limitations of electrodes of different thickness. Various classical explanation approaches reaching from ohmic and HFR to LFR impedance values have been discussed, but it was shown that a complete dynamic transport model is needed to fully describe the electrode performance. The modeling itself is not the scope of this work, but the major input parameter tortuosity can be measured by the blocking TLM method which was demonstrated here.

This said for the study of liquid phase limitations, we now turn to the analysis of solid phase transport processes. In the following the lithiation of graphite particles and the movement of lithiated phases in the solid are studied with the the help of neutron scattering.

5. SANS study of battery electrodes

5.1. Lithiation of graphite

5.1.1. Graphite as anode material

It was graphite that enabled today's Li-ion batteries when Sony introduced it as an anode material in 1991 [19]. Graphite forms graphite intercalation compounds with alkali metals [84, 85] and intercalates Li-ions safely and reversibly and is a reliable alternative to Li metal as a counter electrode. Li metal is undesired because it forms dendrites during reversible cycling of a battery that present a risk of internal short-circuit and electrolyte degradation. The intercalation of Li-ions into graphite has long been known [86] but only since 1990 has the electrochemical intercalation been studied in detail, e. g. by Dahn et al. [87, 88].

Potential and thermodynamical phases

Figure 5.1 shows the potential between 0.4 and 0.01 V upon lithiation and delithiation of a typical artificial graphite anode material. Lithiation starts from pure C and arrives at a maximum of LiC_6 with a theoretical capacity of 372 mAh/g [89]. According to Gibbs' phase rule, the plateaus in potential represent regions of two coexisting phases. In the steep regions between the plateaus only a single phase with solid solution behavior is present. Traditionally up to six phases have been identified, also named stages, because they intercalate the Li-ions in every n^{th} slab between parallel graphene sheets of the graphite lattice. At beginning of lithiation Li-ions are mixed in solid solution like manner into the graphite in the phase 1L (L for liquid). Liquid-like means that there is no in-plane order but Li will distribute in the respective slab. Then during the first plateau, there is a transition to the phase 4L. And further to a phase 3L and further to 2L up to a state of charge of ca. 25% [88, 90]. The identification of phase 2L with LiC_{24} [91] or LiC_{18} [92] has been debated and also the staging of these phases is questioned [93] in favor of mixed phases with a continuous d-spacing shift. The precise determination of phases in a real experiment may of course be hindered by kinetic barriers or overvoltage and insufficient resolution in x-ray data. The last two stages are

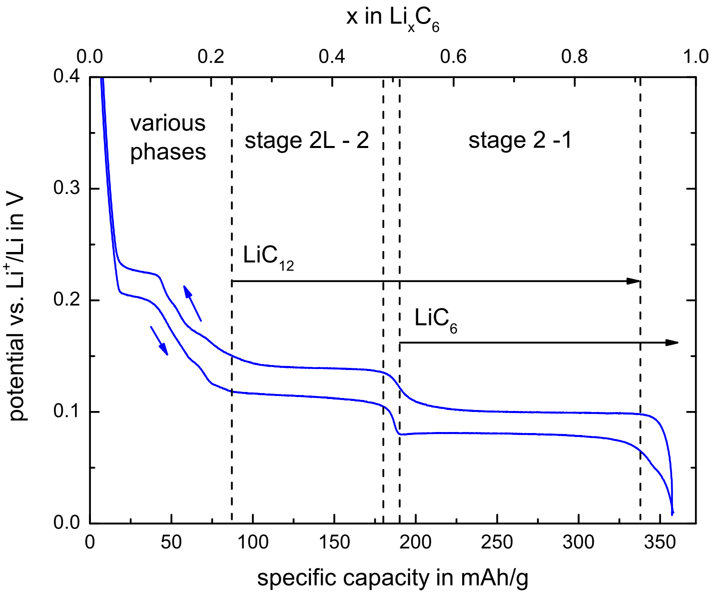

Figure 5.1.: Graphite vs. Li^+/Li half cell. Potential vs. capacity for artificial graphite. Rate C/50, areal capacity 2.1 mAh/cm^2, porosity 55%, electrolyte LP572.

nevertheless most important and well confirmed. The broad plateau just above 0.11 V (lithiation) marks the transition from 2L to stage 2, i. e. LiC_{12}. And the broad plateau at 0.08 V is the transition from LiC_{12} to stage 1, i. e. LiC_6. At the very end of lithiation near 0 V Li metal can be present but this is normally avoided by a careful balancing of the total amount of available Li in a full cell. In a half cell, i. e. graphite vs. lithium, precipitation of metallic Li, also called Li plating, is avoided by carefully monitoring the potential with a reference electrode or by slow cycling.

The relevant graphite 2H is a layered material, constructed from the parallel graphene sheets or basal planes with hexagonal orientation of the individual carbon atoms, compare figure 5.2. The depicted unit cell contains 4 atoms. The stacking is ABAB where every second basal plane is shifted. The space group is then $P\,6_3/m\,m\,c$. [95, 96]. LiC_{12} is space group $P\,6/m\,m\,m$ and stacking is AAαAAα where α denotes the Li-layer in every second interslab. Finally, LiC_6 is $P\,6/m\,m\,m$ and stacking is AαAα because now every interslab is filled with Li ions. In figure 5.2 (b) the hexagonal unit cell is shown with the orientation of a- and c-axis. The corresponding lattice parameters are given in table 5.1. From graphite to the fully lithiated LiC_6 the volume increases by only 13%. This explains the good stability of graphite in commercial Li-ion cells.

In x-ray diffraction studies, see figure 5.3, the major reflections from graphite can

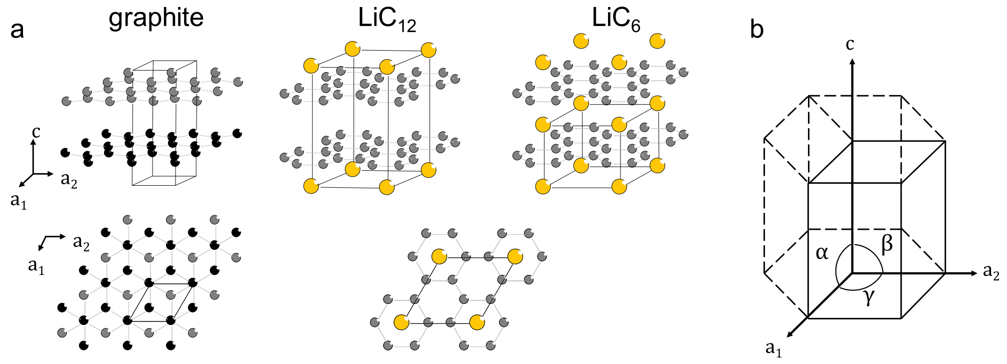

Figure 5.2.: a) Crystal structure of graphite, LiC_{12} and LiC_6, perspective view and projection along c-axis b) hexagonal/trigonal unit cell. Structures redrawn with data from Dolotko et al. [94].

be seen at 3.35 Å, LiC_{12} at 3.53 Å and LiC_6 at 3.70 Å, in accordance with the literature (see table 5.1, [87, 97]). The phase separation of stage 1 and stage 2 is clearly observed. The phases are stable (at least on the timescale of the experiment) and coexist in the bulk of the graphite particle.

phase	lattice parameters in Å [94]	unit cell vol. in Å^3 ($a^2 c \sin 60$)	No. of C atoms per unit cell	No. of Li atoms per unit cell	unit cell vol. rel. to graphite	calc. density in g/cm^3	1st order reflection	d-spacing in Å[87]
graphite $P6_3/mmc$ ABAB	a=2.463 c=6.722	35.31	4	0	1.00	2.26	(002)	3.355
LiC12 $P6/mmm$ AAαAAα	a=4.294 c=7.034	112.32	12	1	1.06	2.23	(002)	3.526
LiC6 $P6/mmm$ AαAα	a=4.317 c=3.700	59.72	6	1	1.13	2.20	(001)	3.7

Table 5.1.: Graphite and its lithiated stages and properties.

Phase transformation

The thermodynamics, i. e. the energetically allowed presence of the staged phases is clear from various experiments and calculations, as reviewed by Dresselhaus et al. [85] and many others. But the kinetics and how exactly one phase transforms

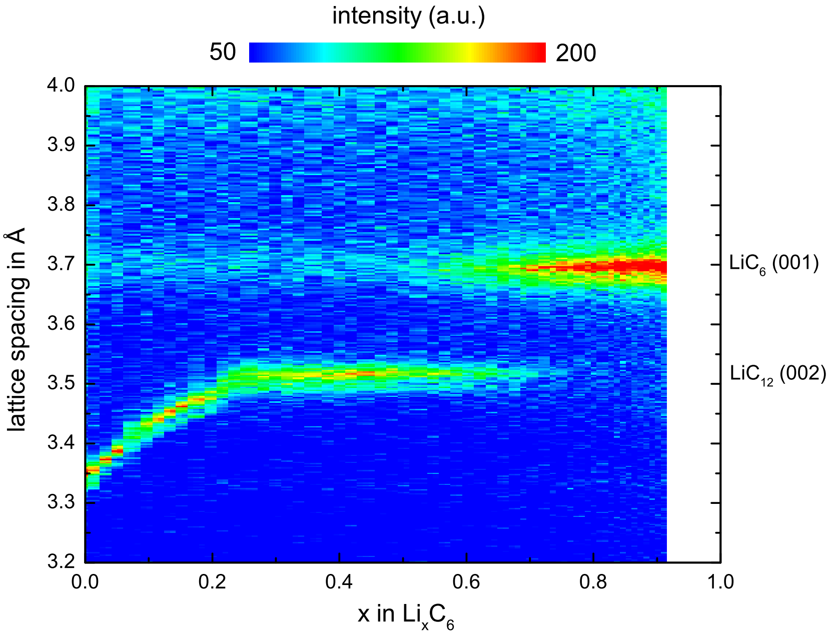

Figure 5.3.: Operando XRD patterns of Li vs. graphite pouch cell. Rate C/5, areal capacity 1.6 mAh/cm^2, electrolyte LP572; cell ID "sept26", see appendix B.5. In cooperation with S. Seidlmayer.

to another has long been questioned. Already in 1969 Daumas and Hérold proposed their model of intercalation islands [98]. They proposed that Li-ions will not intercalate in the same n$^{\text{th}}$ interslab throughout the whole crystallite, but that there are "Daumas-Hérold" domains with the correct staging locally but shifted into another interslab at larger distances. This means that every interslab is partly filled with Li-ion islands. And the model can explain faster Li diffusion and lithiation by means of moving boundaries that use every interslab in contrast to the standard model where either long detours from the edge plane or very slow Li diffusion through basal planes have to be overcome. Simulations, e. g. by Krishnan [99] confirm this rationale. They also claim that the large variety in measured Li diffusivities [100] might also be explained by the stage dependent moving boundary conditions. Recently the intercalation reaction has been observed optically in a sulfuric acid graphite intercalation compound by Dimiev et al. [101]. For this system the domain model was also confirmed and the moving of the phase transformation front from the outside to the inside of a very thin graphite layer could be observed.

Heß et al. [90] studied the voltage plateaus of a very thin electrode of graphite particles (typical battery artifical graphite, median size 3.3 µm) on lithiation and delithiation. For very thin electrodes, overpotentials from the salt concentration gradient and from electronic conduction should not occur, and the authors relate overpotentials directly to the kinetics of lithiation of the particles, i. e. solid diffusion of Li in the graphite. This is justified by comparison to models based on the well-known porous media theory [40]. For high rates, they find that the transitions of the higher phases (4L, 3L, 2L) occur at the same capacity value as before whereas the transitions to stage 2 and 1 occur much earlier on the capacity axis which explains the overall capacity limitation. For delithiation the transition to the higher phases occurs even at values that represent more capacity than is thermodynamically possible. A possible explanation is the coexistence of several phases in the graphite particle and a piecewise lithiation from outside to inside. For lithiation one can imagine a situation as depicted in figure 5.4. Here, 2L is still present in the inner particle but stages 2 and 1 are advancing from the edge towards the center. The minimal energy interface might also have a certain angle rather than being orthogonal to the graphite sheets. The boundary moves by diffusion of Li-ions in the interslab. The fact that several phases exist is a result of the kinetic limitation of Li-ion diffusion. As said in terms of potential, limited diffusion of intercalated Li into the interior of the particle leads to a local overpotential which enables the formation of the next higher or lower phase. Seen from the outside, the so-called “shrinking annuli”model features moving rings or better three-dimensional shells of stage 1, 2 and also the higher ones that move into the particle. For delithiation, the same model applies: Li is extracted at the edge and the Li-poor phases propagate from outside to inside of the particle. The capacities until the stage 1 and 2 transition are again lower at high rates, but higher phases retain most of their attributed capacity or even have higher capacity spans. Coexistent phases and a larger margin for overpotential until the upper cut-off is reached can explain this. The authors link this also to the differences in Li diffusivity where the liquid-like phases are expected to achieve higher values. The exact description of the coexistent phases and their interfaces is difficult and parameters such as temperature and defects have strong influence. But it is clear, that in a system that shows this type of multi-phase behavior, diffusion cannot be understood by the simple Fick’s law.

5.1.2. Models of batteries and lithiation

Porous electrode models

Therefore researchers have started to adjust common porous electrode models to staged-diffusion in solid electrode materials. The classic porous electrode model, as introduced by Newman, Doyle and Fuller [40, 55], can simulate the charging and discharging of a battery in a pseudo two-dimensional geometry, commonly in

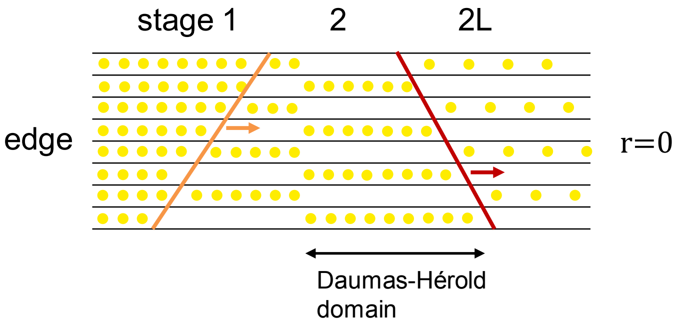

Figure 5.4.: Li intercalation into graphite according to the shrinking annuli model by Heß et al. [90]

the x-dimension from anode to cathode and in a second dimension that represents the radial dimension of the solid active materials, see figure 4.6. Transport in the liquid electrolyte and the two solid phases is modeled by differential equations. The porous nature of the materials is considered by using effective values of the transport parameters as discussed in chapter 4.1. Charge and mass conservation as well as boundary conditions are considered and Butler-Volmer relations link solid and liquid domain by controlling the charge transfer currents at the surface as a function of overpotential. In the classical models the Li distribution in the solid is modeled by Fick type diffusion and gradients may build up in the radial dimension but no phase transitions occur. Many authors in the literature have used these models to simulate the overpotential from salt gradients in the electrolyte plus the contributions from Li-ion gradients in the solid materials [66, 102]. Inhomogeneity in lithiation of the active materials can thus occur in the two model dimensions. Inhomogeneity across the thickness of the electrode is caused mostly by the salt concentration gradient or salt depletion in the liquid electrolyte phase. The liquid phase polarization effect is illustrated in a simulation in figure 5.5 (left) which leads to low lithiation in the solid (right). Electronic conductivity could also play a role but is mostly weaker than the electrolyte contribution. This causes the top layer of the electrode next to the separator to be lithiated first and a lithiation front is moving from particle to particle across the electrode. Harris et al. have demonstrated this experimentally for very thick electrodes [103]. Pietsch et al. [104] have shown x-ray tomography data from very thick graphite electrode and correlated volume change to lithiation. On the order of 100 µm the electrodes were however quite homogeneously lithiated. The second inhomogeneity contribution is within a particular particle, in the classical models in the "representative" average particle and its radial dimension. It is this gradient of Li concentration in the solid that we investigate in this work.

Upon fast lithiation with slow diffusion in the solid, Li concentration gradients build up in the solid and it takes some time to get the Li from the surface shell to the interior, resulting in lithiation from the outside to the inside. Bernardi et al. [105] simulate overpotential contributions in the classical framework by using an experimentally motivated step function for the open circuit potential. For the agglomerate secondary particle delithiation is shown to occur from outside to inside, so that the particle has a preferentially delithiated shell that is progressing inwards.

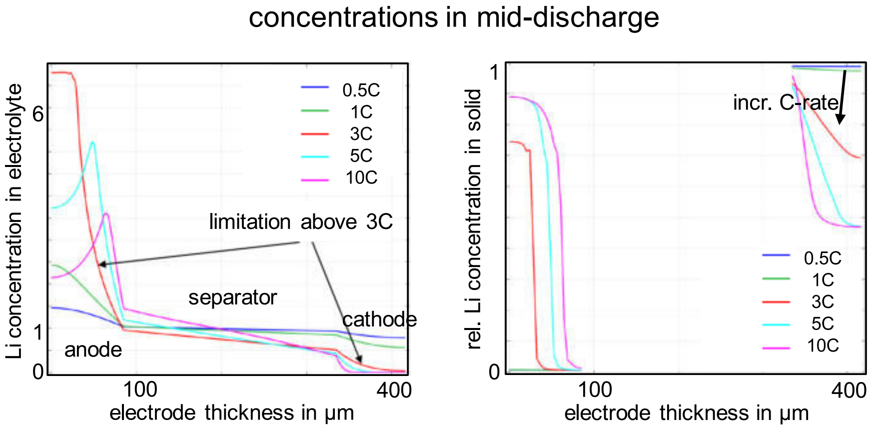

Figure 5.5.: Typical Li concentration gradients in electrolyte (left) and solid (right) during discharge of a graphite/NMC cell with increasing rate, anode areal capacity 4.2 mAh/cm^2, cathode areal capacity 3.4 mAh/cm^2, porosities 33%, simulated with COMSOL by Stephan Kosch (ExZellTUM). Li concentration in arbitrary units.

Advanced models with phase separation

For the correct simulation of phase transitions more advanced models have been developed. Ferguson and Bazant [106] reformulate the battery simulation by using a phase field approach and by using concentration dependent chemical potentials for each phase. First, the motivation was to understand the two-phase behavior of $LiFePO_4$ which was debated in numerous qualitative and quantitative models before [107–109]. But also graphite as a multi-phase material has attracted interest [110] and the experimentally observed phase separation in an extended electrode could be reproduced. Bohn et al. [111] also used a thermodynamical model based on chemical potential and a free energy function plus the classical differential equations to model the behaviour of phase changes in graphite. It was shown that this model can better predict stress and strain in graphite particles during cycling, whereas simpler models have focussed on gradients or moving boundaries [112]. Bohn et al. assume three lithiated phases (from the open circuit potential plot) and show how the lithated phases move into the particle from the particle surface, thus a moving boundary emerges from the model. A lithiation at a rate of 0.7 C in a standard graphite electrode of 100 µm thickness shows low inhomogeneity across the electrode (overpotential below the difference between thermodynamic potentials of the phases) but indeed reveals the coexistence of two phases inside the particle and the presence of a lithiation front moving into the particle.

In summary, it is known that graphite is a multi-phase material where some of the phases or stages coexist during cycling. XRD shows which phases are present, but not where they are or how they are distributed spatially. Literature suggests that the lithiation of graphite particles occurs from outside to inside. The aim of this work is to measure the radial distribution of Li in the graphite particles. As shown above, the most significant signal can be expected from the two last stages 2 and 1, LiC_{12} and LiC_6. They are not overlapping and exist over a relatively long capacity range.

Imaging lithiation fronts in particles

As already mentioned above, there is numerous work on the general existence of distinct phases during the lithiation of graphite and also other multi-phase materials. But that research is mostly based on volume averaging methods such as x-ray or neutron diffraction and no information on the spatial distribution of lithiated phases is given. This has obviously not hindered graphite from becoming the dominating anode material. However, the high volume expansion of possible future anode materials such as silicon or germanium makes them very sensitive against cracking from stress during (de)lithiation and a deeper understanding of lithiation fronts moving through the particle is very desirable. First transmission electron microscopy experiments on silicon [113], graphene coated silicon [114] and on Ge [115] have been conducted and allow to follow the lithation of individual particles directly and in situ. Bordes et al. have studied silicon by time-of-flight secondary ion mass spectrometer imaging and mapped the Li distribution [116]. Here, we apply SANS to get spatial information (but averaged over the whole sample) from lithiation of graphite. Future application to novel anode materials seems possible.

5.2. Small-angle neutron scattering theoretical background

5.2.1. Classical SANS theory

Instrument and technique

Small-angle neutron scattering (SANS) is a powerful technique to study systems at length scales of one to several hundred nanometers non-destructively [117, p. 731]. The SANS-1 instrument of the Forschungreaktor München II (FRM II) neutron source at the Heinz Maier-Leibnitz Zentrum (MLZ) in Garching uses cold neutrons with a selectable wavelength of 4.5 Å to 20 Å to study scattering of a sample at low angles of a few degrees, which are given by a sample-detector distance of up to 20 m and a detector area of 1 m^2 [118–120]. The principle is shown in figure 5.6: The incoming beam is scattered at the sample position and evaluated at the detector under all accessible scattering angles 2θ.

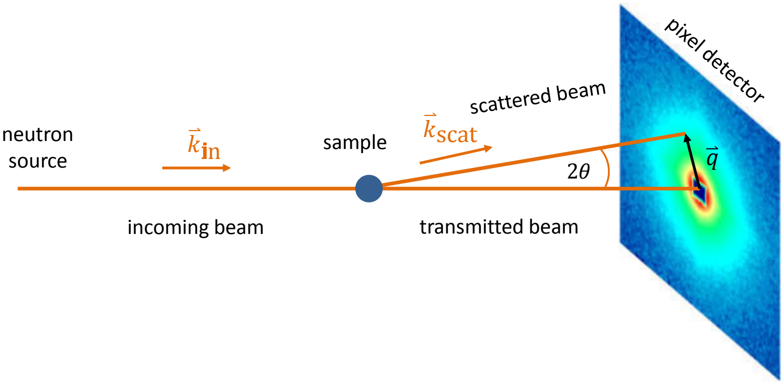

Figure 5.6.: Scheme of the SANS setup and detector raw data. Scheme inspired by [117].

The weak interaction of neutrons with the nuclei of the sample results in a high penetration depth which allows to study many systems in situ during operation without opening or destroying them [121, p. 23]. Also, the relative strength of neutron interaction for lighter elements is enhanced and more suitable for the study of a number of elements, in particular Li. This is a major advantage of neutrons compared to x-ray radiation.

Scattering theory for single particle

In the context of quantum mechanics, a microscopic particle like a neutron can be described as a wave function, which is a solution to the Schrödinger-equation and in general a function of position $\vec{r}$ and time t. The simplest wave function is a plane wave and a physical particle is best represented by a wave package of plane wave contributions. We introduce a simple plane wave ψ which is moving in the direction of $\vec{k}$ [122, p. 57]:

$$\psi(\vec{r},t) = e^{i(\vec{k}\vec{r}-\omega t+\phi)} \tag{5.1}$$

where the wave vector $|\vec{k}| = 2\pi/\lambda$ and the angular frequency $\omega = |\vec{k}|v$ yield direction and dynamics of the wave with wavelength λ and phase velocity v. ϕ is a general phase shift. De Broglie linked the momentum p of a traveling particle with the wave vector via $|\vec{k}| = p/\hbar$. Taking the square of this complex wave function yields physical observables, i.e. probability densities. For a stationary scattering problem we can omit the time dependence. Imagine a single particle or wave being scattered at a spherically symmetric potential at the center of the coordinate system. The simplest solution to this scattering problem can be given as the superposition of an incoming plane wave and a scattered circular wave, so that at large distances from the scatter potential at the center:

$$\psi(\vec{r},t) \overset{r\to\infty}{=} e^{i\vec{k}_{\text{in}}\vec{r}} + f(\vartheta,\varphi)\frac{e^{ik_{\text{scat}}r}}{r} \tag{5.2}$$

with the scattering amplitude factor f and the absolute values r and k of the respective vectors [122, p. 505]. This is true if the potential decays faster than $1/r$ at $r \to \infty$. The probability to find the scattered particle at a certain infinitely small solid angle $d\Omega(\vartheta,\varphi)$ is then the square of the magnitude of f, which is also named differential scattering cross section $d\sigma/d\Omega$ and is given in units of m^2:

$$\frac{d\sigma}{d\Omega} = |f(\vartheta,\varphi)|^2 \tag{5.3}$$

The differential scattering cross section is proportional to the number of particles scattered per second into $d\Omega$ divided by the number of particles that arrive at the sample per second per sample area. The total scattering cross section can be calculated by integrating over the whole solid angle 4π. In azimuthal symmetry and with a scattering sample centered at the origin (compare figure 5.7) of the spherical coordinate system, $f(\vartheta)$ will only depend on the polar angle ϑ. It is the angle between the incoming beam and the scattered beam. By definition, this angle is often called 2θ. For elastic scattering, i. e. $|\vec{k}_{\text{in}}| = |\vec{k}_{\text{scat}}|$ [117, p. 732], we can relate the momentum transfer q to 2θ by:

$$\vec{q} = \Delta\vec{k} = \vec{k}_{\text{scat}} - \vec{k}_{\text{in}} \tag{5.4}$$

$$q = |\vec{q}| = \frac{4\pi}{\lambda}\sin\theta \tag{5.5}$$

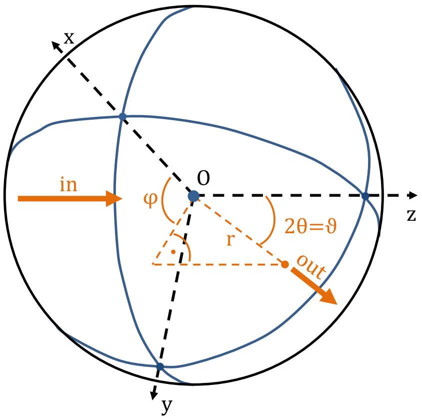

Figure 5.7.: Scattering from a spherically symmetric potential at the center of the coordinate system. Incoming wave in z-direction.

In neutron scattering it is common to use the scattering vector $\vec{q}$ (with unit 1/length) instead of the ambiguous θ or 2θ to plot the scattered intensity as a function of the "scattering angle". Using the Born approximation we can write f as a Fourier transformation of the interaction potential V:

$$f(\vec{q}) \propto \int V(\vec{r}) e^{-i\vec{q}\vec{r}} d^3r \tag{5.6}$$

Another Ansatz uses the standard expansion of a wave function in spherical waves and Legendre polynomials keeping only the s-wave part with vanishing angular momentum of the wave function. This is possible at low energies, i. e. if λ is relatively large compared to the effective radius of the interaction potential. This is true for the typical wavelength of cold neutrons of 10^{-10} m compared to the small nuclei radii of $< 10^{-14}$ m and thus point-like interaction. We then arrive at $f = -b$ which is the so called scattering length and has the unit of length [122, p. 516 and 547]. Combining these two results we can deduce a pseudo potential for this simple case which has the same solution for f:

$$V \propto b\,\delta(\vec{r}) \tag{5.7}$$

with the Dirac-δ function [123, 124]. The scattering length b is a measure of how the particle potential interacts with the incoming wave, i. e. it characterizes the range of interaction.

Scattering theory for ensemble of particles

For an ensemble of N nuclei at positions $\vec{r}_\mathrm{i}$ we can write:

$$V(\vec{r}) \propto \sum_{\mathrm{i}=1}^{N} b_\mathrm{i}\delta(\vec{r} - \vec{r}_\mathrm{i}) \tag{5.8}$$

$$f(\vec{q}) \propto \sum_{\mathrm{i}=1}^{N} b_\mathrm{i} e^{-i\vec{q}\vec{r}_\mathrm{i}} \tag{5.9}$$

or, if we go from discrete point-like particles b_i to a continuous distribution of scattering lengths we can write [117, p. 746]:

$$V(\vec{r}) \propto \rho(\vec{r}) \tag{5.10}$$

where $\rho(\vec{r})$ is the locally averaged scattering length divided by the volume over which averaging is performed: this volume may be a molecule or a region with dimensions up to the minimum resolvable distance which is of the order of nanometers, compare [121, p. 230] [125]. ρ is the so called scattering length density (SLD) and has the unit of m^{-2}. This is possible because the typical neutron wavelength does not resolve individual atoms and the sum can be replaced by integration over the sample volume.

Finally the scattering amplitude can be written as:

$$f(\vec{q}) \propto \int_{\mathrm{V_{sample}}} \rho(\vec{r}) e^{-i\vec{q}\vec{r}} d^3r \tag{5.11}$$

We normalize the microscopically defined differential cross section (i. e. per atom) $d\sigma/d\Omega = |f(\vec{q})|^2/N_\mathrm{atom}$ to the macroscopic differential cross section $d\Sigma/d\Omega$ by dividing by the irradiated sample volume V and get the probability to find a particle, scattered from a given sample volume with N_atom atoms.

$$\begin{aligned} \frac{d\Sigma}{d\Omega}(\vec{q}) &= \frac{N_\mathrm{atom}}{V}\frac{d\sigma}{d\Omega} \\ &= \frac{1}{V}|f(\vec{q})|^2 \\ &= \frac{1}{V}\, f \cdot f^* \\ &= \frac{1}{V}\int_\mathrm{V}\int_\mathrm{V'} \rho(\vec{r})\rho(\vec{r'}) e^{-i\vec{q}(\vec{r}-\vec{r'})} d^3r\, d^3r' \end{aligned} \tag{5.12}$$

In a typical case, an assembly of N identical particles which are correlated in space, we write by statistically averaging over all particle orientations [117, p. 748]:

$$\begin{aligned} \frac{d\Sigma}{d\Omega} &= \frac{1}{V}\left\langle \int_V \rho(\vec{r})e^{-i\vec{q}\vec{r}}d^3r \int_{V'} \rho(\vec{r}')e^{+i\vec{q}\vec{r}'}d^3r' \right\rangle \\ &= \frac{1}{V}\left\langle |\int_V \rho(\vec{r})e^{-i\vec{q}\vec{r}}d^3r|^2 \right\rangle \end{aligned} \tag{5.13}$$

We write the SLD as the sum of a reference average ρ_0 (e. g. from solvent) and a fluctuation $\rho = \rho_0 + \Delta\rho$, thus:

$$\begin{aligned} \frac{d\Sigma}{d\Omega} &= \frac{1}{V}\left\langle |\underbrace{\int_V \rho_0 e^{-i\vec{q}\vec{r}}d^3r}_{\text{vanishes}} + \underbrace{\int_V \Delta\rho(\vec{r})e^{-i\vec{q}\vec{r}}d^3r}_{\Delta\rho\neq 0 \text{ only in particle volumes}} |^2 \right\rangle \\ &= \frac{1}{V}\left\langle |\int_{\text{all}\,V_\text{P}} \Delta\rho(\vec{r})e^{-i\vec{q}\vec{r}}d^3r|^2 \right\rangle \\ &= \frac{1}{V}\left\langle |\sum_i^N e^{-i\vec{q}\vec{r}_\text{i}} \cdot \int_{V_\text{P}} \Delta\rho(\vec{u})e^{-i\vec{q}\vec{u}}d^3u|^2 \right\rangle \end{aligned} \tag{5.14}$$

First, the contribution from ρ_0 is zero. This is often called Babinet's principle, meaning that only differences in SLD or contrast matter, not the absolute values. All the information on differences is contained in $\Delta\rho$ and we can continue with this function without loss of information. More precisely, we can say that ρ_0 is constant everywhere and the Fourier transform of a constant is a delta function $\delta(\vec{q})$. For $\vec{q} \neq 0$ this is zero. Second, the space vector could be separated into a part pointing to the center of mass of a particle i and and a position vector inside the particle : $\vec{r} = \vec{r}_\text{i} + \vec{u}$. We can then integrate over only one particle and sum up with a phase factor from the particle centers. Executing the square operation, we arrive at:

$$\begin{aligned} \frac{d\Sigma}{d\Omega} &= \frac{1}{V}\left\langle \sum_i^N \sum_j^N e^{-i\vec{q}(\vec{r}_\text{i}-\vec{r}_\text{j})} \cdot \int_{V_\text{P}}\int_{V_\text{P}} \Delta\rho(\vec{u})\Delta\rho(\vec{v})e^{-i\vec{q}(\vec{u}-\vec{v})}d^3u\,d^3v \right\rangle \\ &= \underbrace{\frac{N}{V}\frac{1}{N}\left\langle \sum_i^N \sum_j^N e^{-i\vec{q}(\vec{r}_\text{i}-\vec{r}_\text{j})} \right\rangle}_{\equiv S(\vec{q})} \cdot \underbrace{\int_{V_\text{P}}\int_{V_\text{P}} \Delta\rho(\vec{u})\Delta\rho(\vec{v})e^{-i\vec{q}(\vec{u}-\vec{v})}d^3u\,d^3v}_{\propto P(\vec{q})} \end{aligned} \tag{5.15}$$

For a typical (on large scale) unordered isotropic and homogeneous two phase system, the difference $\Delta\rho^2$ can be extracted from the second term and we arrive at the general expression for the SANS scattering cross section [117, 126]:

$$\frac{d\Sigma}{d\Omega} = \frac{N}{V}\, S(\vec{q})\, V_{\mathrm{P}}^2\, \Delta\rho^2\, P(\vec{q}) \tag{5.16}$$

The first term, the structure factor S, denotes the inter-particle interaction or correlation. In contrast, the second term represents the intra-particle properties of the scattering potential expressed through the scattering length density and the so called form factor P. The same concept is often applied to scattering from crystals, where S represents the lattice structure and P the atomic properties. However, in SANS the concept is applied on a much larger scale, i. e. to particles and their interaction. Written separately:

$$P(\vec{q}) = |\frac{1}{V_{\mathrm{P}}} \int_{V_{\mathrm{P}}} e^{-i\vec{q}\vec{r}} d^3r|^2 \equiv |F(\vec{q})|^2 \tag{5.17}$$

$$S(\vec{q}) = \frac{1}{N} \left\langle \sum_i^N \sum_j^N e^{-i\vec{q}(\vec{r}_{\mathrm{i}}-\vec{r}_{\mathrm{j}})} \right\rangle = 1 + \frac{1}{N} \left\langle \sum_i^N \sum_{i\neq j}^N e^{-i\vec{q}(\vec{r}_{\mathrm{i}}-\vec{r}_{\mathrm{j}})} \right\rangle \tag{5.18}$$

For a simple system consisting of two phases, e. g. N dilute, i. e. uncorrelated, particles with volume V_{P} embedded in a matrix, S is unity and equation 5.16 can be simplified to:

$$\frac{d\Sigma}{d\Omega} = \frac{N}{V}\, V_{\mathrm{P}}^2\, \Delta\rho^2\, P(\vec{q}) \tag{5.19}$$

where $\Delta\rho^2 = (\rho_{\mathrm{P}} - \rho_{\mathrm{matrix}})^2$ is the square of the difference in scattering length density of the two phases. The factor $\Delta\rho^2$ is describing the scattering contrast of two phases and describes the change of typical SANS signals, as we will see below. In general, one can define the following squared scattering contrast factor between two phases A and B:

$$\Delta\rho^2 = (\Delta\rho)^2 = (\rho_{\mathrm{A}} - \rho_{\mathrm{B}})^2 \tag{5.20}$$

However, we have to be careful about the vanishing ρ_0 contribution. The theoretically sharp delta peak at $q = 0$ has a finite width which is connected to the overall sample size, the dimensions of which are normally much higher than the largest scale probed by the scattering experiment. But one has to also consider the later defined coherence volume, which is typically smaller than the sample size. The width of the zero q peak is of the order of the inverse coherence length. Assuming a coherence length of 100 nm we get a peak width of around 10^{-3} Å^{-1}, which still is small.

For isotropic scattering $d\Sigma/d\Omega$ does not depend on the angle φ (compare figure 5.7) but only on ϑ resp. q which is the magnitude of $\vec{q}$.

Calculating scattering length densities

The SLD of a molecule or chemical complex consisting of x_i atoms of type i can be calculated from the tabulated scattering length values b_i of the individual atoms and the molecular volume $V_\mathrm{molec,P}$ or from molar volume $V_\mathrm{molar,P}$ and Avogadro's number via:

$$\rho_P = \frac{1}{V_\mathrm{molec,P}} \sum x_\mathrm{i} b_\mathrm{i} = \frac{N_\mathrm{A}}{V_\mathrm{molar,P}} \sum x_\mathrm{i} b_\mathrm{i} \tag{5.21}$$

Equation 5.16 shows how one can tune the contrast by changing the particle and the surrounding matrix with varying scattering length density differences. A commonly used technique is to exchange isotopes such as hydrogen and deuterium, which have a very different SLD and enable good contrast between labeled and unlabeled species [117, p. 751]. The scattering length has been measured for many atoms and can be found in the literature, e.g. [121]. It is important to note that b relates to the coherent part of scattering only.

This is because we can split up the scattering into two contributions: coherent and incoherent scattering. We write $d\Sigma/d\Omega$ using equation 5.9 and 5.12 for individual scatter centers:

$$\frac{d\Sigma}{d\Omega} = \frac{1}{V} \sum_\mathrm{i}^{N} b_\mathrm{i} e^{-i\vec{q}\vec{r}_\mathrm{i}} \sum_\mathrm{j}^{N} b_\mathrm{j} e^{+i\vec{q}\vec{r}_\mathrm{j}} \tag{5.22}$$

But even for chemically identical atoms the interaction with neutrons and thus the scattering length b can be different due to differences in isotope or spin. Imagine b of these atoms to be split into an equal average (e. g. over isotope or spin) contribution $\langle b \rangle$ and a standard deviation from this value $(b - \langle b \rangle)^2$ (not correlated between atom positions), then we arrive at:

$$\frac{d\Sigma}{d\Omega} = \frac{1}{V} \left(\langle b \rangle^2 |\sum_\mathrm{i}^{N} e^{-i\vec{q}\vec{r}_\mathrm{i}}|^2 + N \left\langle (b - \langle b \rangle)^2 \right\rangle \right) \tag{5.23}$$

The first term is the q-dependent coherent scattering which gives us information on the sample structure, the second term is the incoherent scattering which gives a constant background. For coherent scattering, phase differences ($\phi = -i\vec{q}\vec{r}$) do play a role and complex scattering amplitudes are summed up. For incoherent scattering, only intensities, i. e. squared amplitudes, from all the atoms are summed up and phase relations are lost. The summation yields N times a q-independent factor from each atom. Both contributions add up to the total cross section of an atom, which is also tabulated. In typical experiments incoherent background mostly stems from incoherent hydrogen scattering [127, p 4.12ff.]. As mentioned above, the structural information in SANS experiments is contained in the q-dependent coherent contribution and all scattering formulae will normally refer to this. This conclusion remains valid also after the transition from sum to volume integral, as already shown above, due to the fact that neutrons do not resolve individual atoms.

5.2.2. SANS applications

In the derivations above, a SANS experiment probes the sample by measuring its scattering signal as a function of scattering angle or q. When combining equation 5.5 with the well-known Bragg law, here $\lambda = 2l \sin\theta$, we get a simple rule of thumb relating q to a typical length scale of $l = 2\pi/q$ [117, p. 732]. With this estimation, the q-range of the experiment can be compared to the typical length scale in the sample.

But not every peak can be attributed to a length clearly. Instead, one has to look at the form and structure factors of equation 5.16. Analytic solutions can be found for simple systems. From the general definition of the factors in equation 5.17 and 5.18, we can already see the following asymptotic behaviors:

$$\begin{aligned} P(q \to 0) &= 1 \\ P(q \to \infty) &= 0 \\ S(q \to \infty) &= 1 \end{aligned} \tag{5.24}$$

Dilute systems

For dilute systems with no inter-particle correlation we have already seen that $S = 1$ and the macroscopic cross section is dominated by the form factor in equation 5.19. Some form factors are given in the following.

Sphere

For a dilute mixture of small monodisperse spheres only the form factor $P = |F|^2$ is shaping the intensity at the detector. The expression for F is well known and can be written for spheres with a radius R [128]:

$$F_{\text{sphere}}(q, R) = \left(3\frac{\sin(qR) - qR\cos(qR)}{(qR)^3}\right) \tag{5.25}$$

Guinier approximation

At small angles, i.e. small q (precisely $qR < 1$), and again with dilute colloids one can use a low-q expansion and get a form factor of [128] [117, p. 756] [125, p. 5.19]:

$$P(q) = F^2 \propto e^{-\frac{(qR_\mathrm{g})^2}{3}} \tag{5.26}$$

$$\frac{d\Sigma}{d\Omega}(q, R_\mathrm{g}) = \frac{N}{V} V_\mathrm{p}^2 \Delta\rho^2 \cdot e^{-\frac{(qR_\mathrm{g})^2}{3}} \tag{5.27}$$

with the radius of gyration R_g which is related to the radius R of a sphere by $R_\mathrm{g} = \sqrt{3/5}R$ [129]. In the Guinier regime, plotting the logarithm of the intensity versus q^2 thus yields the squared radius of gyration R_g^2 as slope and the particle radius can be determined.

Porod limit

At large angles, i. e. large q ($qR > 10$), small distances are probed. A common image is, that e. g. for a particle in a surrounding matrix not the whole particle but only the local interface is probed. For compact particles this interface looks locally flat and has no shape as shown in figure 5.8, left. Again, we can develop $P(q)$ for large q and arrive at the macroscopic cross section:

$$\begin{aligned}\frac{d\Sigma}{d\Omega}(q) &= \frac{1}{V} 2\pi\Delta\rho^2 A_\mathrm{surf}\, q^{-4} \\ &= \phi_\mathrm{part} 2\pi\Delta\rho^2 \frac{A_\mathrm{surf}}{N \cdot V_\mathrm{part}} q^{-4}\end{aligned} \tag{5.28}$$

with A_surf being the total sum of surface area of all particles in the sample, and in the latter expression $\phi_\mathrm{part} = NV_\mathrm{part}/V$ being the volume fraction of particles [117, p. 758] [130] [125, p. 5.18] [131].

Simple fractal

Systems are not always compact but may have complicated structures. If these structures are self similar on varied length scales, they are called fractal, compare figure 5.8, right. At large q, the Porod equation can be generalized to an exponential q-dependence and a background correction, and then typically reads:

$$\frac{d\Sigma}{d\Omega}(q) = c_1 q^{-n} + c_0 \tag{5.29}$$

where the background c_0 is typically understood as incoherent background. This equation is often used to fit experimentally obtained data. The exponent $n = 6 - D$ gives information on the properties of the system, where D is considered as the fractal dimension of the system.

The following classification can be made [132, p. 227] [130]:

$$\begin{array}{lr} n = 4 & \text{smooth surface} \\ n = 3\,\text{to}\,4 & \text{rough, fractal surface} \\ n = 2\,\text{to}\,3 & \text{mass fractal} \end{array}$$

So, even if no specific features in $d\Sigma/d\Omega\,(q)$ can be seen, the slope of the logarithmic plot still gives information about the system's structure. Note, that at large q the structure factor approaches unity, which is why the total macroscopic cross section follows directly from P, here.

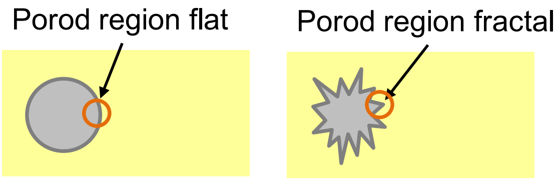

Figure 5.8.: Illustration of the effectively measured region in Porod regime.

Concentrated, correlated particle systems

For correlated systems, where inter-particle interaction cannot be neglected, the situation is more complicated because we have to consider the structure factor S as well. From equation 5.18:

$$\begin{aligned} S &= 1 + \frac{1}{N}\left\langle \sum_{i}^{N} \sum_{i \neq j} e^{-i\vec{q}(\vec{r}_{\mathrm{i}} - \vec{r}_{\mathrm{j}})} \right\rangle \\ &= 1 + \frac{N}{V} \int_V (g(\vec{r}) - 1) e^{-i\vec{q}\vec{r}} d^3 r \end{aligned}$$

with the pair-correlation function $g(\vec{r})$ which describes the probability to find a particle at a given distance from another one [117, p. 748]. It is often an exponential function of the particle-particle interaction potential. A maximum in the S-function is suggestive of a certain preferred inter-particle distance, but with a caveat. Figure 5.9 (a) and (b) shows how both, S and F contribute to a signal.

The general laws that were derived above for $S = 1$ can be tested under correlation. The Porod law was derived for large q, where by definition the structure factor approaches unity, thus the large q Porod law remains valid. For the Guinier law this does not hold and it can in general not be used in these conditions.

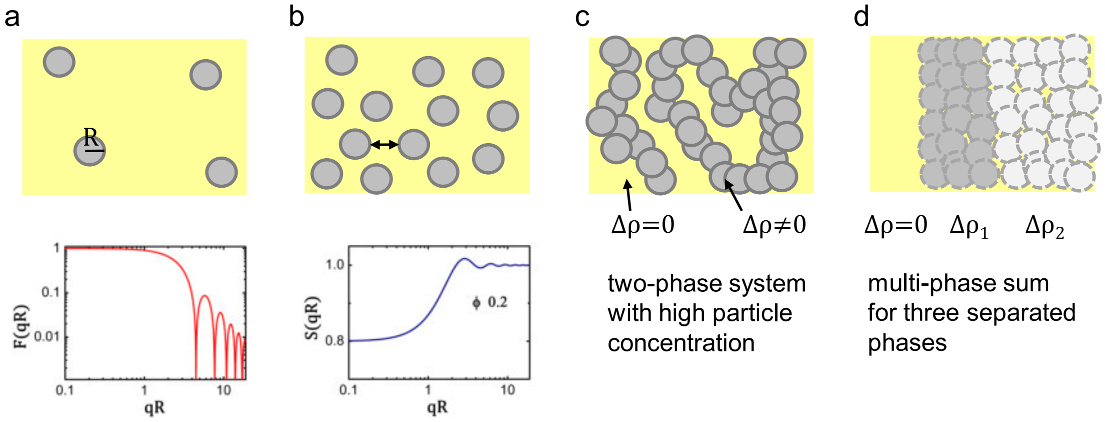

Figure 5.9.: Form and structure factors: a) F vs. qR for dilute spheres , b) S vs. qR for correlated spheres (inspired by [125]), c) concentrated system of two phases and d) separated domains of three-phase system.

Complicated mass fractal

It is a tedious task to get analytical solutions of the general scattering integral, but by using symmetries and other data, for many systems a more or less simple equation can be derived. Fractal concepts cannot only be applied to surfaces but also to mass distributions. One could think of a porous structure with self-similar packing of particles - e. g. small crystals packed to particles which are again packed to form an electrode. For a fractal distribution of mass, Teixeira and Schmidt [130, 133] give the following fit formula:

$$\frac{d\Sigma}{d\Omega} = \frac{d\Sigma}{d\Omega}(0)\frac{\sin((D-1)\arctan(q\,\chi_{\mathrm{i}}))}{(D-1)\,q\,\chi_{\mathrm{i}}\,(1+q^2\,\chi_{\mathrm{i}}^2)^{(D-1)/2}} \tag{5.30}$$

where D is again the fractal dimension and χ_{i} is a rough measure of the size of the fractal structures, i. e. the primary particles. Note that the $\Delta\rho^2$-dependence is still in the prefactor $d\Sigma/d\Omega(0)$.

$$\chi_{\mathrm{i}}^2 = \frac{2R_{\mathrm{g}}^2}{D(D+1)} \tag{5.31}$$

is the connection to the radius of gyration [130]. In [16], we have used these relations to fit mass fractals to cathode particles.

5.2.3. SANS for large battery active material particles

Dense, non-particulate multiphase systems

There are systems, e. g. water-oil emulsions, solids with inhomogeneities, or large-particle systems, where the concept of individual particles embedded in a solvent matrix does not make sense anymore. This case is illustrated in figure 5.9 (c). We can still use Babinet's principle but we can no longer separate form and structure factor. In a homogeneous multi-phase system $\rho(\vec{r})$ will be a partially continuous function that takes the constant ρ values of the phases in their respective volume shares. We can expand the integral 5.13 with two phases in their respective volumes V_1,V_2, against a reference phase in the residual volume, as shown in figure 5.9 (d):

$$
\begin{aligned}
\frac{d\Sigma}{d\Omega} =& \frac{1}{V} \left\langle |\int_V \rho(\vec{r}) e^{-i\vec{q}\vec{r}} d^3r|^2 \right\rangle \\
=& \frac{1}{V} \left\langle |\int_{V_1} \Delta\rho_1 e^{-i\vec{q}\vec{r}} d^3r + \int_{V_2} \Delta\rho_2 e^{-i\vec{q}\vec{r}} d^3r|^2 \right\rangle \\
=& \frac{1}{V} \left\langle \Delta\rho_1^2 \int_{V_1}\int_{V_1} e^{-i\vec{q}(\vec{r}-\vec{r'})} d^3r d^3r' \right. \\
& + \Delta\rho_2^2 \int_{V_2}\int_{V_2} e^{-i\vec{q}(\vec{r}-\vec{r'})} d^3r d^3r' \\
& \left. + 2\Delta\rho_1\Delta\rho_2 \,\mathrm{Re}[\underbrace{\int_{V_1}\int_{V_2} e^{-i\vec{q}(\vec{r}-\vec{r'})} d^3r d^3r' \,]}_{\equiv \tilde{S}_{\mathrm{ij}}(\vec{q})} \right\rangle
\end{aligned}
\tag{5.32}
$$

where V is the irradiated volume and Re[ ] is the real part (from change in the order of the volume integration). In this expression, the contrast $\Delta\rho$ can be extracted. The result is a sum of squared and mixed terms of $\Delta\rho_{\mathrm{i}}$,$\Delta\rho_{\mathrm{j}}$ times a q-dependent scattering function $\tilde{S}_{\mathrm{ij}}(\vec{q})$ (compare also [125, p. 5.21], [134] and [132, p. 319]):

$$
\frac{d\Sigma}{d\Omega} = \frac{1}{V} \left\langle \Delta\rho_1^2 \tilde{S}_{11}(\vec{q}) + \Delta\rho_2^2 \tilde{S}_{22}(\vec{q}) + 2\Delta\rho_1\Delta\rho_2 \,\mathrm{Re}[\tilde{S}_{12}(\vec{q})] \right\rangle \tag{5.33}
$$

The $\tilde{S}_{\mathrm{ij}}$ are related by the fact, that the volumes are incompressible. As before (compare equation 5.17) we can normalize the scattering functions to their respective integration range so that we can write:

$$
\frac{d\Sigma}{d\Omega} = \frac{1}{V} \left\langle V_1^2 \Delta\rho_1^2 \tilde{S}'_{11}(\vec{q}) + V_2^2 \Delta\rho_2^2 \tilde{S}'_{22}(\vec{q}) + 2V_1V_2 \,\Delta\rho_1\Delta\rho_2 \,\mathrm{Re}[\tilde{S}'_{12}(\vec{q})] \right\rangle \tag{5.34}
$$

with

$$\tilde{S}'_{\mathrm{ij}}(\vec{q}) = \frac{1}{V_{\mathrm{i}}V_{\mathrm{j}}}\tilde{S}_{\mathrm{ij}}(\vec{q}) \tag{5.35}$$

In the pure terms we see some analogy to equation 5.19, considering the limit of one particle where V_{i} is V_{P} and $\tilde{S}'_{\mathrm{ii}}(\vec{q})$ is just $P(\vec{q})$. In the general case, however, $\tilde{S}'_{\mathrm{ij}}$ are integrated over the respective phase volumes and may have a complicated, oscillating behavior.

For additional insight, we can look at the Porod regime, i. e. at large q. In the battery systems with large micrometer-sized particles, most of the q range can be considered to be in the Porod regime and we expect similar behavior as in the 1+1-phase (solid plus electrolyte) particle system above. We rewrite the Porod law, referring to phase volumes and identifying a factor which is equivalent to $\tilde{S}'_{\mathrm{ii}}(\vec{q})$:

$$\left.\frac{d\Sigma}{d\Omega}\right._{\mathrm{Porod}}(q) = \frac{1}{V}V_{\mathrm{i}}^{2}\Delta\rho^{2}\,\underbrace{2\pi\frac{A_{\mathrm{surf}}}{V_{\mathrm{i}}^{2}}\,q^{-4}}_{\tilde{S}'_{\mathrm{Porod}}(q)} \tag{5.36}$$

Imagine the following thought experiment: We have a system with a constant background phase and a solid material where the phase can change between two phases. Strictly speaking, this is a (1+2)-phase system. Starting with only one solid phase, more and more of the solid is transformed to the other phase and the overall 1+1-phase system transforms into a 1+2-phase system with background phase plus two solid phases. When the whole solid has been transformed, we have a 1+1-phase system again. Start and end point of this system are well described by the single-phase Porod formula, given above. One can assume that in a first approximation A_{surf} varies with $V_{\mathrm{i}}^{2/3}$. When inserting $\tilde{S}'_{\mathrm{Porod}}(q)$ in equation 5.34 - in the 1+1-phase case, where only pure terms are present, we see that the macroscopic scattering cross section is proportional to q^{-4}, $\Delta\rho^{2}$ and a function containing the phase volumes V_{i}. The phase volumes can also be expressed as volume fractions. Going back to the general case, for the transition, i. e. the multi-phase region, we expect $d\Sigma/d\Omega$ to be a continuous, say “smooth”, function of all these variables.

Thus, the total scattering contribution is a function of volume fractions, $\Delta\rho^{2}$ and mixed $\Delta\rho$ terms, each times a q-dependent function. We can use this to explain the overall change in scattered intensity during operando battery cycling experiments. If we assume that when going from a two phase situation to the other two phase situation (i. e. background plus one solid phase) all the structural parameters remain constant, i. e. the phase volume V_{i} is the same (neglecting minor volume change), the change in scattering stems from the change in $\Delta\rho_{\mathrm{i}}^{2}$, only. In summary the scattering will thus vary by the squared differences in SLD with a “smooth” transition between the background plus one solid 1+1-phase situations.

Integral measures

In general, expressions for q-dependent scattering can be further simplified by integration over q resp. scattering angle. These quantities describe how a sample scatters "overall" and are represented by relatively simple expressions. The first property is just the integral over q, the integrated intensity Γ:

$$\text{Integrated intensity: } \Gamma = \int_{q_{\min}}^{q_{\max}} \frac{d\Sigma}{d\Omega}(q)\, dq \tag{5.37}$$

which is, after the assumptions above, also proportional to $\Delta\rho^2$ and the volume fractions. The second is the integral $\int q^2\, d\Sigma/d\Omega(q)\, dq$, the so-called Porod invariant [135]. From equation 5.11 where ρ quasi is the Fourier coefficient follows with Parseval's identity, that if we integrate over $\vec{q}$, the result is proportional to the average of the squared coefficient ρ. Taking into account spherical coordinates and Babinet's principle, we arrive at [128, p. 75 - 81], [136, p. 46, 52 - 55]:

$$\text{Porod invariant: } \int_{0}^{\infty} q^2 \frac{d\Sigma}{d\Omega}(q)\, dq = 2\pi^2 \left\langle \Delta\rho^2 \right\rangle \tag{5.38}$$

For a 1+2-phase system we can express the average as :

$$\left\langle \Delta\rho^2 \right\rangle = (\rho_2 - \rho_1)^2 \phi_2 \phi_1 + (\rho_2 - \rho_0)^2 \phi_2 \phi_0 + (\rho_1 - \rho_0)^2 \phi_1 \phi_0 \tag{5.39}$$

with SLDs ρ and volume fractions ϕ of the phases one and two and a background phase (labelled "0"). Again we get an expression that is proportional to $\Delta\rho^2$ and the volume fractions.

SANS-1 setup and finite resolution

All the measurements were conducted at the SANS-1 experiment in the beam guide experiment hall at the MLZ in Garching [137]. In the FRM II, neutrons are produced from nuclear fission of highly-enriched uranium. Around the core a moderator of heavy water D_2O slows down fast neutrons. Further moderation is achieved by the cold neutron source, where cooled deuterium D_2 thermalizes the neutrons to 25 K [138]. These neutrons are fed into various neutron guides. For SANS-1, an s-shaped neutron guide of $(50\,\text{mm})^2$ feeds cold neutrons to the experiment setup which is depicted in figure 5.10. A rotating wavelength selector allows to choose a wavelength between 4.5 and 20 Å by varying the rotation speed. A wavelength spread $\Delta\lambda$ of 10 % is chosen. Polarizers and spin flippers allow further preparation of the beam, but are not relevant in this work. Downstream follows a collimation length of up to 20 m and related apertures of 10 mm diameter before the beam passes a pinhole of 8 mm diameter as well as the sample and arrives at the detector of $1\,\text{m}^2$, which can be positioned at 1.2 to 20 m from the sample. The detector is an assembly of 128x128 He^3 tubes with an achievable spatial resolution of $(8\,\text{mm})^2$. Collimation length and sample detector distance are normally chosen to be equal to improve resolution and intensity. The accessible q range can be calculated with equation 5.5 and is between $10^{-3}\,\text{Å}^{-1}$ and $1\,\text{Å}^{-1}$ [118, 119].

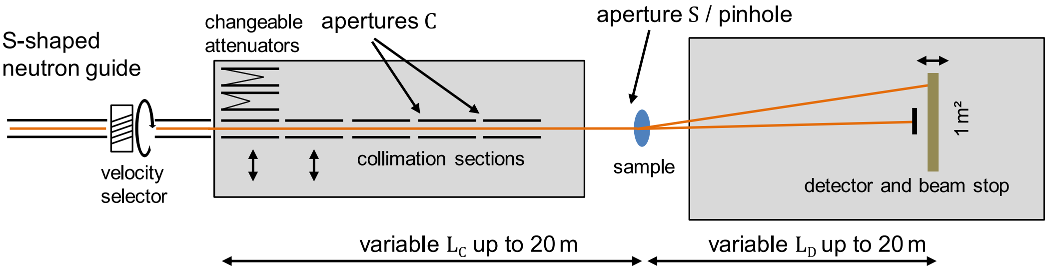

Figure 5.10.: Scheme of the SANS-1 instrument setup. Pinhole 8 mm diameter. Adapted from Heinemann et al. [137]

The resolution at the detector can also be calculated. Δq is the minimum difference that can be distinguished at the detector, the simplest q-resolution function is given by the derivative of equation 5.5:

$$\left(\frac{\Delta q}{q}\right)^2 = \left(\frac{\Delta\lambda}{\lambda}\right)^2 + \left(\frac{2\Delta\theta}{2\theta}\right)^2 \tag{5.40}$$

In general, also other geometrical contributions have to be taken into account [139] [125, p. 5.11]. But for our experiments with large particles q-resolution, is not crucial and is not discussed in detail. The polydispersity of typical particle ensembles has a similar effect: the intensity as a function of q is smeared out, either through uncertainty in q or in radius $\propto 1/q$. In thick samples, also multiple scattering can occur and complicate the analytic interpretation further.

Finite interaction volume given by coherence length

Until now, we have assumed perfect plane waves for the derivation of the scattering intensity equations. In reality this is not true due to at least two reasons. First, particles like neutrons are not described by plane waves with unique $\vec{k}$ but rather by a wave package, which has a certain longitudinal and transverse extension. Second, this wave package is shaped by the geometry and optics of the beam setup. Two simple estimations for longitudinal and transverse coherence lengths can be deduced from the wavelength spread $\Delta\lambda$ and the source broadening, e. g. the broadening after the collimation aperture with diameter d_C.

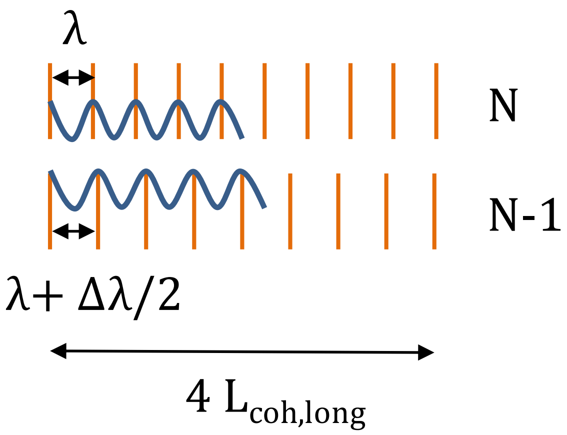

Figure 5.11.: Illustration of longitudinal coherence length.

Longitudinal coherence

Figure 5.11 shows the distance, after which the central-λ wave and the lengthened $\lambda + \Delta\lambda/2$ wave are in phase again. This distance is thus associated with a phase difference of 2π. If we define a phase difference of $\pi/2$ as maximum allowable phase difference for coherence, the longitudinal coherence length $l_{\mathrm{coh,long}}$ is:

$$4l_{\mathrm{coh,long}} = N\lambda = (N-1)(\lambda + \frac{\Delta\lambda}{2}) \tag{5.41}$$

so that

$$l_{\mathrm{coh,long}} = \lambda(\frac{1}{4} + \frac{\lambda}{2\Delta\lambda}) \approx \frac{\lambda^2}{2\Delta\lambda} \tag{5.42}$$

Transverse coherence

Figure 5.12 illustrates how we can deduce the transvere coherence length from source broadening. We have two apertures, the first with a diameter d_{C} after collimation (SANS-1, 10 mm) and the second just in front of the sample with diameter d_{s} (SANS-1, 8 mm). Their distance is the collimation length L (e. g. a few meter). Now, what is the phase relation of these partial waves at the sample where they interact? At point A, we look at the wave fronts of path 1,2 and 3 which meet at an angle α and β. The question is, how far we can go in transverse direction, before reaching a maximum distance between the wave fronts of $\lambda/4$, i. e. a phase difference of $\pi/2$.

This transverse distance is defined as transverse coherence length $l_{\mathrm{coh,trans}}$. In the typical case we write:

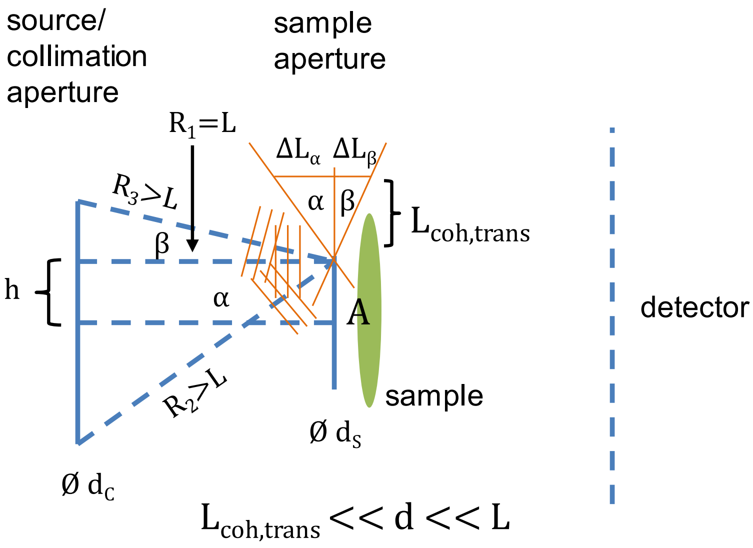

Figure 5.12.: Geometric sketch indicating maximum transverse coherence length due to source broadening.

$$\begin{aligned} \tan\,\alpha &= \frac{\frac{d_\mathrm{C}}{2}+h}{L}, \quad \tan\,\alpha = \frac{\Delta L_\alpha}{l_\mathrm{coh,trans}} \\ \tan\,\beta &= \frac{\frac{d_\mathrm{C}}{2}-h}{L}, \quad \tan\,\beta = \frac{\Delta L_\beta}{l_\mathrm{coh,trans}} \end{aligned} \tag{5.43}$$

$$\text{thus } \Delta L_{\alpha/\beta} = \frac{\frac{d_\mathrm{C}}{2}\pm h}{L}\, l_\mathrm{coh,trans} \tag{5.44}$$

We set the summed up ΔL equal to $\lambda/4$:

$$\Delta L = \frac{d_\mathrm{C}}{L}\, l_\mathrm{coh,trans} = \frac{\lambda}{4} \tag{5.45}$$

and arrive at:

$$l_\mathrm{coh,trans} = \frac{\lambda L}{4 d_\mathrm{C}} \tag{5.46}$$

This calculation gives a good estimate of the geometric contributions to coherence length. The experimental coherence length may also depend on further factors, such as beam guide properties and optics, as e. g. discussed in [140]. Also the definition of coherence (here $\phi = \pi/2$) may vary in the literature, so do pre-factors (1/2, 1/4, ...) [125, 127].

Transverse and longitudinal coherence length combine to the coherence volume, i. e. the volume where coherent wave interaction can take place at the sample. Coherent interaction means that we deal with superposition of complex wave amplitudes and that interference effects occur, so that the above derived scattering equations hold. On a larger scale, the whole sample volume is covered by these independent coherence volumes that add up incoherently by adding the intensity, i. e. the square of the wave amplitude. For this incoherent sum or superposition, interference does not occur and the overall intensity scales linearly with the added intensities [125, p. 5.13]. For the typical SANS-1 setup with medium 8 m collimation length and a wavelength of 6 Å ± 10 %, we get a longitudinal coherence length of 3 nm and a transverse coherence length of 120 nm. The larger of the two coherence lengths limits the maximum reach of interfering interaction between different atoms or SLDs. It is this volume V_{coh}, where $|f|^2$ is evaluated. Regions outside this diameter will only add up incoherently according to the $|f|^2$ in their respective vicinity, as shown in figure 5.13.

Scattering from coherence volume and its dependence on material phases

We can rewrite the scattering equations considering this finite interaction volume. In the first situation the coherence volume V_{coh} is much larger than the individual particles. In order to compute all the contributions, we mesh the sample space and calculate the coherent interaction in the coherence volume $V_{\text{coh,k}}$ centered at this mesh element k, as depicted in figure 5.13 (a). Then we incoherently sum up the contributions from all coherence volumes $V_{\text{coh,k}}$ where k runs over all mesh elements. Since the coherence volume is much larger than the chosen mesh element volume, each element was counted more than once and we have to correct for the number of mesh elements per coherence volume. This gives the scaling factor $V_{\text{mesh}}/V_{\text{coh}}$, where V_{mesh} is the mesh element volume. This makes sure that the result is not dependent on the choice of mesh. Putting all together, equation 5.12 can be rewritten:

$$\begin{aligned}\frac{d\Sigma}{d\Omega}(\vec{q}) &= \frac{1}{V}\frac{V_{\text{mesh}}}{V_{\text{coh}}}\sum_{\text{mesh k}}^{N_{\text{mesh}}} |f|^2 \\ &= \frac{1}{V}\frac{V_{\text{mesh}}}{V_{\text{coh}}}\sum_{\text{mesh k}}^{N_{\text{mesh}}} \int_{V_{\text{coh,k}}}\int_{V_{\text{coh,k'}}} \rho(\vec{r})\rho(\vec{r'})e^{-i\vec{q}(\vec{r}-\vec{r}')}d^3r\,d^3r'\end{aligned} \tag{5.47}$$

where N_{mesh} is the number of mesh elements. For an ensemble of particles using similar assumptions as in the derivations above, e. g. separating intra- and inter-particle contributions, we arrive at:

$$
\begin{aligned}
\frac{d\Sigma}{d\Omega}(\vec{q}) &= \frac{1}{V}\frac{V_{\text{mesh}}}{V_{\text{coh}}}\sum_{\text{mesh k}}^{N_{\text{mesh}}}\left\langle\sum_{i,j}^{N_{\text{P,coh}}} e^{-i\vec{q}(\vec{r}_{\text{i}}-\vec{r}_{\text{j}})}\right\rangle \int_{V_{\text{P}}}\int_{V_{\text{P}}} \Delta\rho^2 e^{-i\vec{q}(\vec{u}-\vec{v})} d^3u\, d^3v \\
&= \frac{1}{V}\frac{V_{\text{mesh}}}{V_{\text{coh}}}\cdot N_{\text{mesh}} \underbrace{\left\langle\sum_{i,j}^{N_{\text{P,coh}}} e^{-i\vec{q}(\vec{r}_{\text{i}}-\vec{r}_{\text{j}})}\right\rangle}_{N_{\text{P,coh}}S_{\text{coh}}(\vec{q})} \underbrace{\int_{V_{\text{P}}}\int_{V_{\text{P}}} \Delta\rho^2 e^{-i\vec{q}(\vec{u}-\vec{v})} d^3u\, d^3v}_{V_{\text{P}}^2\Delta\rho^2 P(\vec{q})} \\
&= \frac{1}{V}\frac{V}{V_{\text{coh}}}\cdot N_{\text{P,coh}}\cdot S_{\text{coh}}(\vec{q})\cdot V_{\text{P}}^2\Delta\rho^2 P(\vec{q}) \\
&\overset{V_{\text{coh}}=V}{\rightarrow} \frac{1}{V}\cdot N_{\text{P}}\cdot S(\vec{q})\cdot V_{\text{P}}^2\Delta\rho^2 P(\vec{q})\,,
\end{aligned}
\tag{5.48}
$$

where $N_{\text{P,coh}}$ is the number of particles inside a single coherence volume and $\vec{r}_{\text{i}}$, $\vec{r}_{\text{j}}$ denote the centers of these particles. We assume that the particles are so small that they are either inside or outside the coherence volume. The average denotes averaging over all possible orientations (e. g. over time) as before. We can identify the well known expressions for S and P. For small particles P will be the same as before, but S is restricted to particles inside the coherence volume, as indicated by the label “coh”. For many statistically distributed particles in the coherence volume the expressions S_{coh} and P will not depend on the chosen k and be the same for all shifted coherence volumes and we can evaluate the sum by multiplying with the mesh number N_{mesh}. If V_{coh} approaches the total sample volume V, equation 5.48 simplifies to the general SANS equation 5.16. Therefore, in a standard SANS experiment coherence does not play a role because particles and all interesting interactions are usually much smaller than the coherence volume.

However, when measuring large micrometer-sized battery particles, we have to take the coherence volume into account and keep in mind, that we will always see the overall incoherent sum of individual coherent contributions from coherence volumes, see figure 5.13 (b). Again, the way to compute this properly is to mesh the sample and add up the contributions. If the mesh is chosen fine enough, the result should converge to a stable value for total intensity that is not dependent on the numerical method, a requirement in all finite element simulations. We apply this concept to the multi-phase equation 5.34:

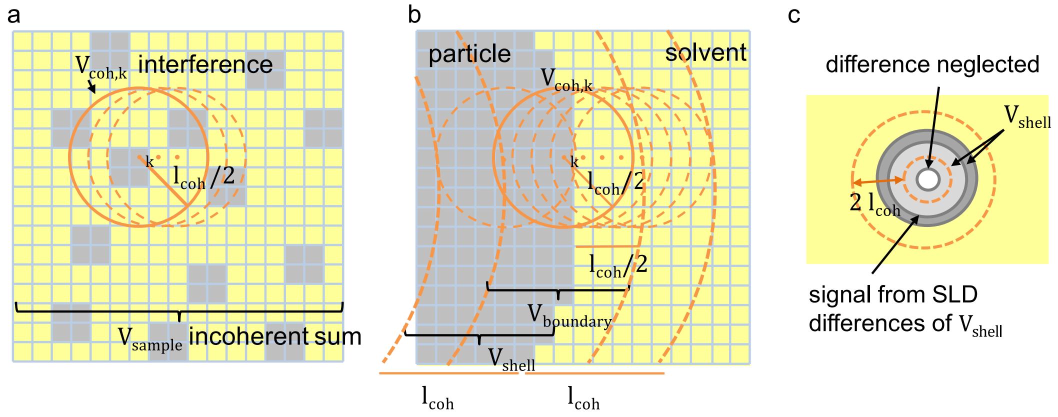

Figure 5.13.: a) Adding up contributions from the coherence volumes centered at each mesh element for small particles. b) and c) situation for a large particle. The coherence length is probing SLD differences in the outer shell - we neglect differences inside particle.

$$\begin{aligned}
\frac{d\Sigma}{d\Omega}(\vec{q}) &= \frac{1}{V}\frac{V_{\mathrm{mesh}}}{V_{\mathrm{coh}}}\sum_{\mathrm{mesh\ k}}^{N_{\mathrm{mesh}}} \underbrace{\left\langle \sum_{\mathrm{phases\ i,j}} V_{\mathrm{i}}V_{\mathrm{j}}\Delta\rho_{\mathrm{i}}\Delta\rho_{\mathrm{j}}\tilde{S}'_{\mathrm{ij}}(\vec{q})\right\rangle}_{\text{restricted to coh. vol.}} \\
&\to c_0 + \frac{1}{V}\frac{V_{\mathrm{mesh}}}{V_{\mathrm{coh}}}\sum_{\mathrm{mesh\ k'}}^{N_{\mathrm{m.,bound}}} \underbrace{\left\langle \sum_{\mathrm{phases\ i,j}} V_{\mathrm{i}}V_{\mathrm{j}}\Delta\rho_{\mathrm{i}}\Delta\rho_{\mathrm{j}}\tilde{S}'_{\mathrm{ij}}(\vec{q})\right\rangle}_{\substack{\text{restricted to coh. vol.}\\ \text{centered within boundary zone}}} \\
&= c_0 + \frac{1}{V}\frac{V_{\mathrm{bound}}}{V_{\mathrm{coh}}}N_{\mathrm{P}} \underbrace{\frac{1}{N_{\mathrm{m.,bound}}}\sum_{\mathrm{mesh\ k'}}^{N_{\mathrm{m.,bound}}} \left\langle \sum_{\mathrm{phases\ i,j}} V_{\mathrm{i}}V_{\mathrm{j}}\Delta\rho_{\mathrm{i}}\Delta\rho_{\mathrm{j}}\tilde{S}'_{\mathrm{ij}}(\vec{q})\right\rangle}_{\substack{\text{average over all mesh positions k'}\\ \text{within boundary zone}}}
\end{aligned} \tag{5.49}$$

where N_{P} is the number of particles and $\langle\,\rangle$ denotes averaging over short-time fluctuations; $i = j$ is allowed and for $i \neq j$ we have to take $\mathrm{Re}[\tilde{S}'_{\mathrm{ij}}(\vec{q})]$ as before. In equation 5.49, we made a specific assumption: We only sum up over mesh elements that lie within a boundary zone V_{bound}, $N_{\mathrm{m.,bound}}$ being the number of mesh elements in the boundary zone for all particles. For our system, the SLD differences in the interior of the particle between the lithiated phases are relatively small compared to the SLD difference of each lithiated phase to the surrounding electrolyte, as shown later. So, when summing up the contributions from all coherence volumes we can restrict the range of relevant coherence volumes to those which have their centers in a boundary zone V_{bound}. V_{bound} is illustrated in figure 5.13 (b) and extends to half the coherence length on either side of the particle surface. The constant incoherent background is considered in the factor c_0. We finally get:

$$\begin{aligned}\frac{d\Sigma}{d\Omega}(\vec{q}) =& c_0 + c_1 \cdot \frac{1}{V}\frac{V_{\mathrm{shell}}}{V_{\mathrm{coh}}} N_{\mathrm{P}} \ldots \\ & \frac{1}{N_{\mathrm{m.,bound}}} \sum_{\text{mesh k'}}^{N_{\mathrm{m.,bound}}} \underbrace{\left\langle \sum_{\text{phases i,j}} V_{\mathrm{i}} V_{\mathrm{j}} \Delta\rho_{\mathrm{i}} \Delta\rho_{\mathrm{j}} \tilde{S}'_{\mathrm{ij}}(\vec{q}) \right\rangle}_{\substack{\text{restricted to} \\ \text{coh. vol. of boundary zone}}}\end{aligned} \tag{5.50}$$

where V_{shell} was inserted which is that part of the particle which lies within a distance of $l_{\mathrm{coherence}}$ from the particle surface. For large particles $V_{\mathrm{shell}} \approx V_{\mathrm{bound}}$. Further, the factor c_1 was introduced which accounts for asymmetry in the coherence volume (longitudinal vs. transverse coherence length) and for possible overlap of a coherence volume reaching to neighboring particles. This factor c_1 must not be confused with the factor used in the Porod equation 5.29; the term c_{x} is used for general factors throughout this text. It is V_{shell} where any change in contrast signal emerges, see figure 5.13 (c).

In total, $d\Sigma/d\Omega$ is a smooth function of squared and mixed $\Delta\rho$ contributions and the phase volumes, evaluated and averaged over coherence volumes of the boundary zone. For the 1+1-phase situation (electrolyte plus solid) scattering contributions are given by $\Delta\rho^2$ weighed by its squared phase volume and averaged over the relevant coherence volumes. When a second phase is created, the transition to this 1+2-phase situation (electrolyte plus two solid phases), is expected to be a smooth function, weighing the SLD differences by the respective phase volume fractions in all $V_{\mathrm{coh,k}}$. If all of the first phase transforms to the second, we are back at the 1+1-phase situation with exactly the same structure factors. The only difference lies in $\Delta\rho^2$. Furthermore, on the length scale of the coherence length, we can also safely neglect any change in the structure factors due to expansion of the graphite particle upon lithiation. The shape of the particle remains unchanged. The restriction of coherent interaction to the coherence volume does also simplify the treatment of a real battery system with multiple material layers such as pouch foil, anode, separator and cathode. The thickness of each of these layers is typically larger than the coherence length and the total scattering will just be an incoherent sum of the scattering contributions from these layers.

The concept of coherence length can also be applied to the integral measures. For the first integral measure, the integrated intensity, we get a similar result as above:

$$\Gamma = \int \frac{d\Sigma}{d\Omega}(q)\, dq \overset{\text{single-phase}}{\rightarrow} c_0' + c_1 \frac{1}{V} \frac{V_{\text{shell}}}{V_{\text{coh}}} N_{\text{P}} \cdot \Delta\rho_1^2 \quad \underbrace{\left\langle V_1^2 \int \tilde{S}_{11}'(q)\, dq \right\rangle}_{\substack{\text{average over all coherence} \\ \text{volumes within boundary zone,} \\ \text{average over all particles}}} \tag{5.51}$$

with a $\Delta\rho_\text{i}^2$ (phase to electrolyte) dependence from coherence volume for the single-phase regions. In equation 5.51 we have assumed that $d\Sigma/d\Omega$ resp. $\tilde{S}_{11}'$ effectively depends on q rather than on $\vec{q}$ because we deal with isotropic scattering here. The averaged term with the phase volume V_i and $\tilde{S}_\text{ii}'(q)$ is the same at all single-phase situations, no matter if V_shell is completely phase 1 or phase 2. The transition in-between is more complicated due to the mixed terms in V and $\tilde{S}'$. For the Porod invariant, we get in analogy to equation 5.38:

$$\text{Porod invariant:}$$
$$\int_0^\infty q^2 \frac{d\Sigma}{d\Omega}(q)\, dq = c_1 \frac{V_{\text{shell}}}{V} N_{\text{P}} \cdot \quad \underbrace{2\pi^2 \cdot \langle\langle \Delta\rho^2 \rangle\rangle}_{\substack{\text{average over all coherence} \\ \text{volumes within boundary zone,} \\ \text{all particles}}} \tag{5.52}$$

where we averaged $\langle \Delta\rho^2 \rangle$ over many boundary coherence volumes. Here, $\langle \Delta\rho^2 \rangle$ is given by:

$$\begin{aligned} \left\langle \Delta\rho^2 \right\rangle &= \frac{1}{V_{\text{coh}}} \int_{V_{\text{coh}}} (\rho(\vec{r}) - \bar{\rho})^2 d^3 r \\ &= (\rho_2 - \rho_1)^2 \phi_2 \phi_1 + (\rho_2 - \rho_0)^2 \phi_2 \phi_0 + (\rho_1 - \rho_0)^2 \phi_1 \phi_0 \end{aligned} \tag{5.53}$$

where $\bar{\rho}$ is the mean scattering length density in V_coh and we have used equation 5.39 for a two-solid phase (plus electrolyte) situation, with ϕ_i being the volume fraction of phase i in V_coh. Again we have a dependence on the $\Delta\rho^2$ values and the respective volume fractions in V_coh which are related to the volume fractions in V_shell (for the two solid phases). But we still have to average over many coherence volumes centered within the boundary zone:

$$\langle\langle \Delta\rho^2 \rangle\rangle = \frac{1}{N_{\text{m.,bound}}} \sum_{\text{mesh k'}}^{N_{\text{m.,bound}}} \langle \Delta\rho^2 \rangle \tag{5.54}$$

This can be done numerically and the result is again a "smooth" function of the variables. Figure 5.14 shows an example of a 1+2-phase system (two solid plus electrolyte) with a number of possible coherence volumes indicated by an orange bar (in one dimension). In figure 5.14 (a), seven coherence volumes relevant for averaging are illustrated. In the same manner but with 70 coherence volumes a numerical averaging of $\langle \Delta\rho^2 \rangle$ as defined in equation 5.20 was done for a number of steps (solid phase 2 moving into the particle) and the result is shown in figure 5.14 (b). First there is only phase 1 (1+1-phase), then phase 2 moves in from the left (1+2-phase) until all the solid volume is phase 2 (1+1-phase) in the last step. The averaged $\langle\langle \Delta\rho^2 \rangle\rangle$ shows the expected smooth transition. The relative difference between the two-phase end points is equal to the relative difference in $\Delta\rho^2$, as expected. $(\rho_2 - \rho_0)^2$ to $(\rho_1 - \rho_0)^2$ is -16% of the initial, matching the 16% drop in the figure. The MATLAB script can be found in appendix B.1.

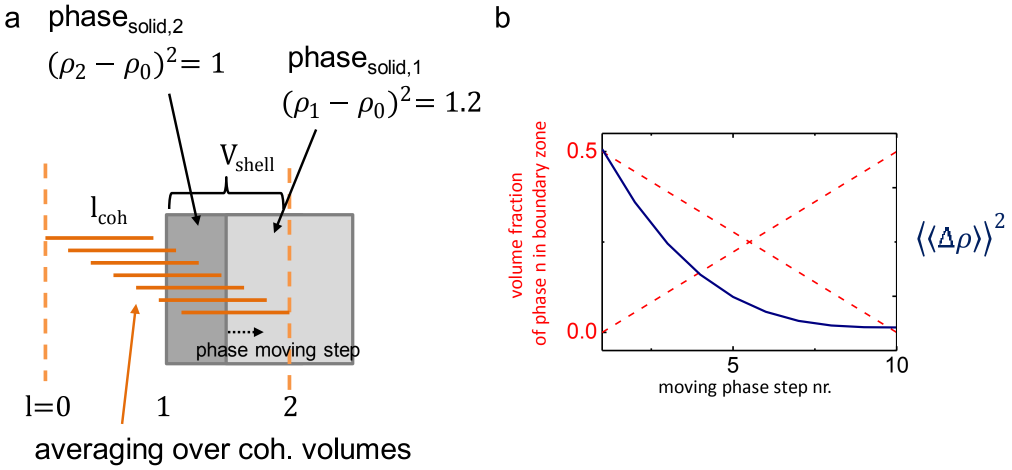

Figure 5.14.: a) Averaging over an ensemble of coherence volumes (here in 1D). b) Numerical simulation of $\langle\langle \Delta\rho^2 \rangle\rangle$ (Porod invariant) for two solid phases with different contrast to electrolyte $\Delta\rho = \rho_{1/2} - \rho_0 = 1.2$ resp. 1, as chosen arbitrarily. Numerical calculation with 70 overlapping coherence volumes indicated by the red lines which limit the range of coherent interaction and contrast. Contributions from these are added up and then normalized. Simulated for 10 steps in time. In the beginning, space right of $l = 1$ is occupied by phase 1 (1+1-phase), space left is electrolyte. Phase 2 is created and moves into the particle, producing a 1+2-phase (electrolyte and two solid) situation. In the end only phase 2 is present (1+1-phase). Difference end point to start point is $\propto (\rho_2 - \rho_0)^2 - (\rho_1 - \rho_0)^2$.

Total scattering cross section

In a last step, in order to get the total macroscopic scattering of the battery, we have to sum up the contributions of all the components in the battery. Since the components like pouch foil, separator, Cu and Al foil, electrolyte and active materials are separated by distances which are large compared to l_{coh}, we can simply add up the individual contributions incoherently. This simple superposition holds true for $d\Sigma/d\Omega(\vec{q})$ as well as for the integral measures, e. g. $\int d\Sigma/d\Omega(q)dq$. We can write the integrated intensity as superposition of contributions from relevant interfaces:

$$\begin{aligned}\Gamma_{\text{total}} = & \int \frac{d\Sigma}{d\Omega}(q)\, dq_{\,\text{cathode/electrol}} \\ & + \int \frac{d\Sigma}{d\Omega}(q)\, dq_{\,\text{anode/electrol}} \\ & + \int \frac{d\Sigma}{d\Omega}(q)\, dq_{\,\text{separator/electrol}} \\ & + \int \frac{d\Sigma}{d\Omega}(q)\, dq_{\,\text{pouch/air}} \\ & + \int \frac{d\Sigma}{d\Omega}(q)\, dq_{\,\ldots}\end{aligned} \tag{5.55}$$

The individual integrated intensity contributions from all the interfaces that are within one coherence volume are given by 5.51. In the case individual particles cannot be identified, the factor $c_1 V_{\text{shell}}/V_{\text{coh}} N_{\text{P}}$ reduces to $V_{\text{shell}}/V_{\text{coh}}$, where the shell volume is determined by the coherence length reaching into the actual structure. The weight of these contributions is thus determined by the volume share (via $V_{\text{shell}} \cdot N_{\text{P}}$), the surface area (via V_{shell}) and $\Delta\rho^2$. We restrict the multi-phase behavior in the coherence volumes of each contribution (i, j in the $\Delta\rho_{\text{i}}$ and $\tilde{S}'_{\text{ij}}$) to only two phases at the interface, e. g. one solid phase and electrolyte. By this method we can calculate start, intermediate and end point of the battery system (NMC and graphite particles with homogeneous phase at least in the shell) which are connected by a smooth transition. Later, we will see that $\Delta\rho^2$ values of the interface of the active materials to the electrolyte dominate the scattering. If we assume this for now and if we put all other contributions (including incoherent background from electrodes and other material) into background constant c'_0, we get:

$$\begin{aligned}\Gamma_{\text{total}} = & c_1 \frac{1}{V} \frac{V_{\text{shell}}}{V_{\text{coh}}} N_{\text{P}} \cdot \Delta\rho_1^2 \left\langle V_1^2 \int \tilde{S}'_{11}(q)\, dq \right\rangle_{\text{cathode/electrol}} \\ & + c_1 \frac{1}{V} \frac{V_{\text{shell}}}{V_{\text{coh}}} N_{\text{P}} \cdot \Delta\rho_1^2 \left\langle V_1^2 \int \tilde{S}'_{11}(q)\, dq \right\rangle_{\text{anode/electrol}} \\ & + c'_0\end{aligned} \tag{5.56}$$

Here, c_1,V_{shell},N_{P},V_1,$\tilde{S}'_{11}$ are specific to the indicated interfaces, but for simplicity indices have been omitted. We can simplify by defining the factor $c_2 = c_1 \cdot 1/V \cdot V_{\text{shell}}/V_{\text{coh}} \cdot N_{\text{P}} \cdot \langle V_1^2 \int \tilde{S}'_{11}(q)\, dq \rangle$:

$$\Gamma_{\text{total}} = c_2 \Delta\rho^2{}_{\text{cathode/electrol}} + c_2 \Delta\rho^2{}_{\text{anode/electrol}} + c'_0 \tag{5.57}$$

Now, all geometric information is contained in the factors c_2. When going from the 1+1-phase state (e. g. fully discharged particle) via a multi-phase state to another 1+1-phase state (say, fully charged particle), the factor c_2 will be the same at start and end. The only difference lies in $\Delta\rho^2$. Thus, we can compute the difference in integrated intensity by:

$$\begin{aligned}\Delta\Gamma_{\text{total}} =&c_2(\Delta\rho_{ch}^2 - \Delta\rho_{dch}^2)_{\text{ cathode/electrol}}\\ &+ c_2(\Delta\rho_{ch}^2 - \Delta\rho_{dch}^2)_{\text{ anode/electrol}}\end{aligned} \tag{5.58}$$

with “ch” denoting the charged and “dch” the discharged state of the battery. In summary, even if we do not know the microscopic structure of all the components in the beam to compute c_2 ab initio, we can still calculate the difference in integrated intensity which is just proportional to the weighed difference in $\Delta\rho^2$ which occurs on the length scale of coherence length. The geometry factor c_2 can be fitted to experimental data or derived from comparing individually measured battery components.

Applications of SANS to battery systems

Battery electrodes with typically micrometer-sized particles in different states of lithiation represent complicated multiphase systems. Since the particles are very large, generally Porod behavior is observed. Mass fractals might also play a role, if one refers to inner structure of particles. In a similar way, porous systems have been analyzed [141] [133], e.g. polymers [142], carbons [143] and coals [126] [144] [145], explosives [146] and various sand stones. In the literature, few SANS studies on battery materials exist. Bridges et al. study SEI evolution in nano-sized pores of carbon [147] by SLD change, where they implicitly assume a $\Delta\rho^2$ dependence of scattering from the SEI constituents weighed by their volume fractions. Wang et al. [148] show first results of the scattering data of a half cell during cycling, without giving a full explanation of the observed phenomena.
The research of this thesis led to the first publication of an in situ scattering experiment with a working battery, where changes in integrated properties are interpreted by the change in contrast as argued above [16]. Data of this publication and additional experiments are presented in the following.

Other neutron scattering techniques related to battery systems

In the recent years a variety of other neutron techniques has been applied to study lithium-ion batteries. Due to the high penetration of neutrons, also commercial batteries can be studied in situ and operando. The most common neutron technique to study batteries has been neutron diffraction (at larger angles) which has been used to analyze phases and structure of anode and cathode in commercial batteries [92, 94, 96, 149, 150]. Senyshyn et al. studied graphite [93] and Zinth et al. [97] focussed on Li plating. These techniques allow to monitor phase transformations in the material but do not yield information on their spatial distribution, similar to XRD. Recently spatially resolved diffraction was used [151]. Others have used neutron imaging or radiography to measure the concentration of Li and the geometry non-destructively [152, 153]. Neutron depth profiling to measure Li concentration was demonstrated recently by Zhang et al. [154]. However, spatial resolution here was limited to tens of µm. It is more the macroscopic distribution of Li across the electrode that has been studied. In its ability to image the local phase contrast on the µm scale and below, SANS remains unique.

5.3. Results of SANS operando experiments

5.3.1. Experimental setup

The data presented here were measured in three campaigns at the SANS-1 instrument in August 2013 (together with November 2013 and February 2014), September 2014 and September 2015. The following measurement setups were used with a neutron wavelength of 6 Å:

1. High resolution:
   sample detector distance (sd) = 20 m,
   beam collimation length (col) = 20 m,
   q-range = 0.014 - 0.192 nm^{-1}

2. Medium resolution:
   sd = 8 m,
   col = 8 m,
   q-range = 0.068 - 0.934 nm^{-1}

3. Low resolution:
   sd = 1.6 m,
   col = 4 m,
   q-range = 0.393 - 4.333 nm^{-1}

Operando measurements were always done with the medium resolution settings. The cells were made from a stack of a single-side coated anode on Cu foil, a separator and a single side coated cathode on Al foil. These stacks were assembled in pouch cells of ca. 6x6 cm^2, electrolyte was added and the cell was vacuum sealed at 50 mbar as also shown in section 3. Table 5.2 shows an overview of all measured cells. Measurement times varied from 10 min to later only 3 min for one data file in operando measurements. Materials and cell properties such as loading and porosity are comparable for all cells, except one deliberately overbalanced cell. Parameters were chosen close to real-life cells with an areal capacity of around 3 $\mathrm{mAh/cm}^2$. All experimental details of the cells are given in appendix B.5. For anode capacity (anode is geometrically oversized) only that part of capacity is considered that is opposite to the cathode. Unless stated otherwise the cells underwent formation of typically two cycles at C/10.

Cycling of the cells was controlled by a Biologic VSP or SP-200 potentiostat. SANS files and potentiostat data were synchronized later, the error in synchronization is not larger than a few seconds in all data shown. The NMC-111/graphite full cells were cycled between 3 to 4.2/4.3 V and graphite/Li was cycled between 0.01 to 1.5 V. Generally, low C-rates were chosen (C/5, C/3 or C/2). Charging was usually CC plus a CV phase. Discharging was CC only for some and CC plus CV for others (z5). The cycling data of all measured cells, which are also identified by the cell ID in the figures, is shown in appendix B.2.

cell ID	cell type	description	date	measurem. time per SANS scatter file in min	limiting electrode area in cm^2	graphite areal capacity in mAh/cm^2, based on 360
epb	pouch	empty pouch bag	May 13	total 88		
0p10	pouch	inactive materials (pouch, Al, Cu, separator, electrolyte)	Aug 13	total 88	9.0	
1p1	pouch	full cell graphite/NMC	Aug 13	total 88	9.0	1.88
0p2a	pouch	full cell without NMC	Aug 13	total 88	12.25	2.12
0p2b	pouch	full cell without graphite	Aug 13	total 88	9.0	1.84
nov1	pouch	full cell graphite/NMC	Nov 13	10	9.0	2.97
nov1	pouch	full cell graphite/NMC	Feb 14	10	9.0	2.97
z5	pouch	full cell graphite/NMC	Sep 14	3	9.0	0.88
z8	pouch	full cell graphite (overbalanced)/NMC	Sep 14	3	9.0	5.00
sept26	pouch	half cell Li/graphite	Sep 15	3	6.76	1.63
sept33	pouch	Li/Li cell	Sep 15	3	6.76	
						porosity 50 ±5%

Table 5.2.: Overview of measured sample cells in SANS experiments. Compare also appendix B.2. NMC is NMC-111.

5.3.2. Signal and data reduction

So, how can we link the material properties of lithiated graphite to the observed SANS signal? First, the neutron passes the sample and arrives at a certain pixel of the detector where it is detected as a count. Figure 5.15 shows the raw data for all measured counts during 10 min from a typical pouch cell. Pixels in real space are shown and one can see the shadow of the beam stop in the middle. One can also see a slight cross in the data, almost aligned with the axes. This is probably from the weak anisotropic scattering from the separator.

The main scattering contribution from the cell is however isotropic and depends only on the scattering angle θ or magnitude of the scattering vector $\vec{q}$, respectively. This is used in the following data reduction procedure.

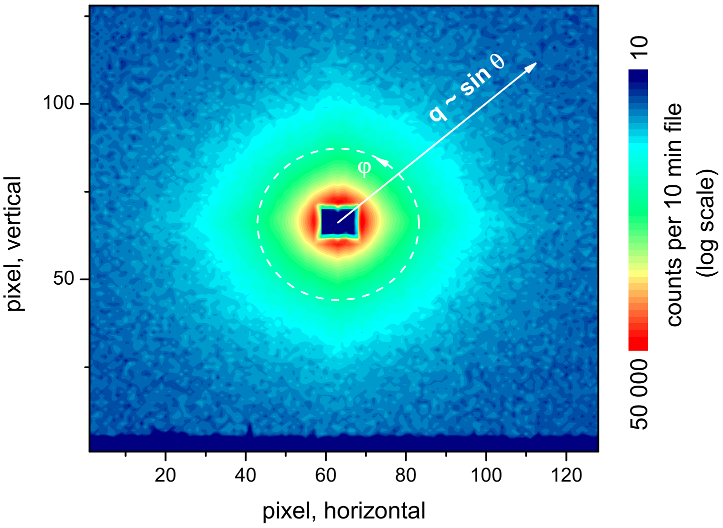

Figure 5.15.: Raw data counts at detector from a pouch cell scattering experiment. The dark rectangle in the middle is the shadow of the beam stop. A slight anisotropy from the separator can be seen. Integrating over ϕ yields the intensity $I(q)$ where q is the magnitude of the scattering vector and proportional to the sine of the scattering angle θ. File taken in 10 min measurement time (cell nov1, first run).

Experimental data reduction

Linking $d\Sigma/d\Omega$ to the experimentally observed count rate $I_{\text{meas}}(q)$ at the detector pixel as illustrated in figure 5.6 can be done in several ways. Details on data reduction are given in appendix B.3. First, the raw data with counts per pixel is corrected for detector dead time and for the incoming intensity which is detected at a monitor in the beam. We also have to normalize for the irradiated sample volume and arrive at:

$$\frac{d\Sigma}{d\Omega} = \frac{I_{\text{meas}}(q)}{I_0\, A\, T\, t\, \Delta\Omega}\,. \tag{5.59}$$

(T is transmission, t is thickness, A irradiated surface, and I_0 incoming flux in neutrons per second per area, typically calculated from beam monitor signal) [125, p. 5.10]. Transmission of the sample is also considered. Also, the effect of electronic noise is subtracted by comparing to a measurement of an absorbent, e. g. B_4C. Furthermore, we can normalize to the absolute scattering cross section of a known standard like a 1 mm thick water sample. Additional scaling factors take into account the experimental setting (collimation length and sample detector distance).

The resulting reduced data should in theory allow a comparison of absolute scattering cross sections measured at different times and settings or even SANS instruments. Due to the large number of parameters some care though has to be taken. In this research mostly one sample (the cell) is measured many times in the same setting and we are only interested in relative changes, so that scaling does not play a role in most of the following analysis. All cell data is then normalized only to deadtime and monitor beam intensity, i. e. to empty beam. The only exception is the broad range scattering of the following section which was scaled to 1 mm of water. The relative contributions of the components are of course valid for all normalizations.

The two dimensional data set can be reduced further because we are only interested in the q-dependence. Therefore a radial averaging over φ in figure 5.15 yields intensity or better (absolute) scattering cross section per solid angle $d\Sigma/d\Omega$ as a function of q. The unit is cm^{-1}.

Typical pouch cell scattering data

Figure 5.16 shows a typical scattering signal from the graphite/NMC-111 pouch cell. The curve mainly follows a Porod scattering even for low q-values with a constant background from incoherent scattering at high q, as given in equation 5.29. As already mentioned, Porod scattering is typical for scattering at structures that are larger than the yardstick $d = 2\pi/q$, so that here nearly all q values are regarded as "large" from the sample's perspective. This means that the structure factors $\tilde{S}'_{11}(q)$ in equation 5.57 follow a Porod behavior $\propto q^{-4}$ as given in equation 5.36.

We can analyze which materials in the beam contribute to the scattering signal. In a full pouch cell, the beam passes a layer of Al-polymer foil, the Cu current collector foil and graphite active material and the separator - the latter two filled with electrolyte in the pores. Then, the beam passes the other electrode, either NMC on Al or Li foil, and a second layer of Al-polymer foil. Since the coherence length is in the range of hundred nanometer, we can safely assume that all components add up incoherently, as in equations 5.55 and 5.57. The outer layers (pouch casing) are contributing very weakly and scatter two orders of magnitude less, except for the incoherent background, which is only a factor of two less. To get the contribution of all inactive materials including metal foils, separator and electrolyte, a dummy cell with everything except active material electrodes was measured. This cell is roughly a factor of three below the measured full cell, so we can conclude that scattering from the active materials is dominant. The q-independent incoherent background is at low absolute values and does not contribute much to the invariant and integrated intensities that will be calculated in the following.

In order to analyze the contributions of the active material of the electrodes further,

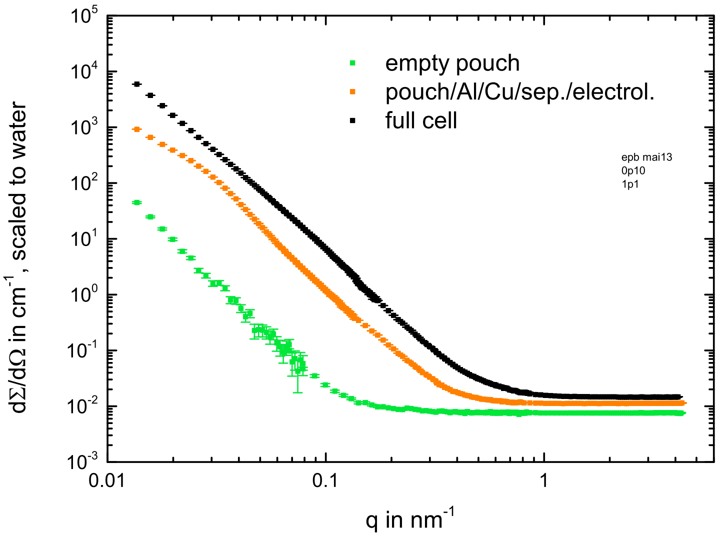

Figure 5.16.: $d\Sigma/d\Omega(q)$ scaled to absolute level vs. 1 mm water. Contributions of pouch foil (2 foils), all inactive materials and a full cell with graphite anode and NMC cathode. Error bars shown. Integrated intensities in the evaluated medium q-range from 0.11 to 0.89 nm^{-1}: empty pouch $0.7 \cdot 10^{-9}\,\text{nm}^{-2}$, all inactive materials $4.4 \cdot 10^{-9}\,\text{nm}^{-2}$ and full cell $18.7 \cdot 10^{-9}\,\text{nm}^{-2}$.

two more cells were built. One cell contained everything including Cu foil except graphite (and binder), the other contained everything including Al foil except NMC (plus binder and little carbon black). When subtracting the inactive material cell data from one of these and the reminder is the pure active material contribution from either anode or cathode. These two contributions together with the inactive material signal are shown in figure 5.17. We can add up anode and cathode contribution plus the inactive material to arrive at a simulated full cell which matches well with the independently measured full cell (within 15% error).

A detailed analysis of the electrode signals shows that the anode follows very well a Porod behavior whereas the cathode data shows a little kink at $q = 0.1\,\text{nm}$. The fitting method here follows [16], but a different data set is used. Details are also given in appendix B.3. The fitted curves are plotted as a line in figure 5.17, in the color of the respective anode or cathode data points. For the anode, $d\Sigma/d\Omega(q)$ can be fitted according to equation 5.29 with a slope of $n \approx 3.9$ which represents a moderately rough fractal surface, near the Porod value $n = 4$. This is in accordance to the impression from the images in figure 3.1 which show potato-shaped and slightly rough graphite particles.

Furthermore, $d\Sigma/d\Omega(q)$ of the cathode can be fitted with a superposition of a

Porod-like background contribution (equation 5.29 with $n = 4$, fixed in this case) and a mass fractal contribution according to equations 5.30 and 5.31 with a fractal dimension of $D = 2.98$ and a radius of gyration of $R_\mathrm{g} = 77.4\,\mathrm{nm}$. The mean radius of gyration can be converted to a mean particle diameter of around 200 nm (see section 5.2.2). This compares reasonably well to the size of the primary NMC particles which are shown in figure 3.2. The dimension D of the mass fractal is close to 3 which is expected for a random globular agglomeration of spherically shaped particles. Besides, part of the cathode SANS signal can be ascribed to carbon black particles with a primary particle diameter of the order of 40 nm and a cluster length of the order of several hundred nm.

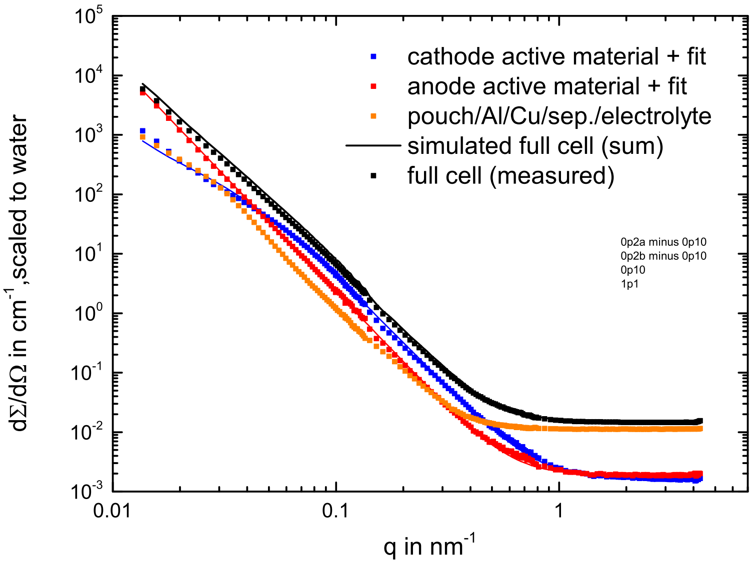

Figure 5.17.: $d\Sigma/d\Omega(q)$ scaled to absolute level vs. 1 mm water. Contributions of inactive materials and of anode and cathode active material alone - this data was gained by subtracting the inactive material signal from cells where either only anode or cathode active material was present. The sum of active materials and inactive materials yields values close to the measured full cell. Error bars are smaller than symbols and omitted. Integrated intensities in the evaluated medium q-range from 0.11 to $0.89\,\mathrm{nm}^{-1}$: cathode NMC $11.3 \cdot 10^{-9}\,\mathrm{nm}^{-2}$ and graphite anode $6.1 \cdot 10^{-9}\,\mathrm{nm}^{-2}$.

The classical SANS analysis, i. e. fitting $d\Sigma/d\Omega(q)$ to a function determined by the shape and distribution of particles, is not applied here for this kind of battery sample because the particles are too large and no distinct features are observed. But one can use the fact that the scattering signal is a function of the $\Delta\rho^2$ of the scattering materials, see equation 5.57. Upon cycling of the battery, the distribution of Li and lithiated phases changes and we can generally expect a change of the materials in the beam. Figure 5.18 shows that indeed the scattering power of the sample is changing upon lithiation. The difference is significant and except for the first two data points, the error bars are reasonably small.

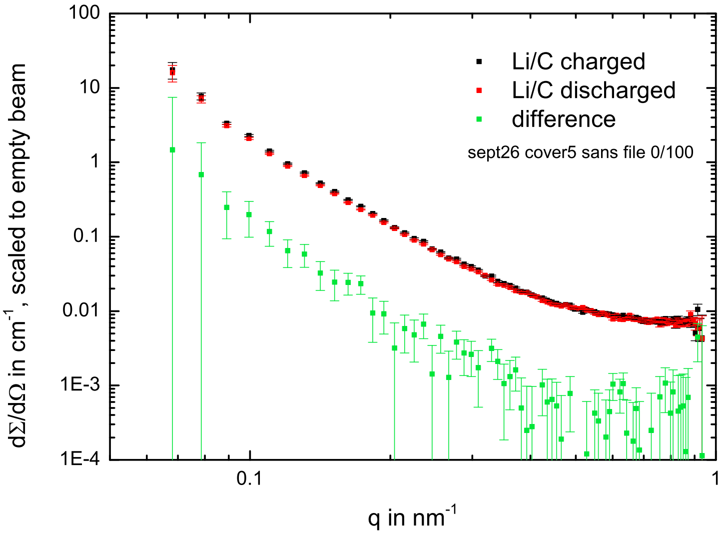

Figure 5.18.: $d\Sigma/d\Omega(q)$ scaled to empty beam. Li/C half cell (cell ID sept26) at charged (graphite delithiated) and discharged (graphite lithiated) state. Difference in signal with error bars. Medium q-range.

To get a measure of the overall scattering power of a sample, we can calculate the integral measures that have been defined before. The first is the integrated intensity Γ, defined in equation 5.37. The second is the Porod invariant, defined in equation 5.38. Integrated intensity and Porod invariant are calculated numerically from the data points using the trapezoidal method. An error estimation for both quantities is calculated from the individual errors given for each data point from the SANS raw data, i. e. via the root mean square method. Figure 5.18 shows that the relative error is very high for the first and for the last data point on the q-axis. Therefore, to reduce the error of the integral the first four and the last four data points at low respectively high q are discarded in the following, giving the evaluated medium q-range from 0.11 to 0.89 nm^{-1}.

We have already shown theoretically, that both, integrated intensity and Porod invariant are assumed to be a smooth function that is proportional to $\Delta\rho^2$ in the two-phase regions. Indeed, for a Li/C half cell the two curves have a similar look, as shown in figure 5.19. Both decrease with lithiation and increase again upon delithiation in a similar manner. The error bar however is smaller on the simple integrated intensity and we will thus use this measure in the following data analysis, keeping in mind that all results can also be derived by looking at the classical Porod invariant.

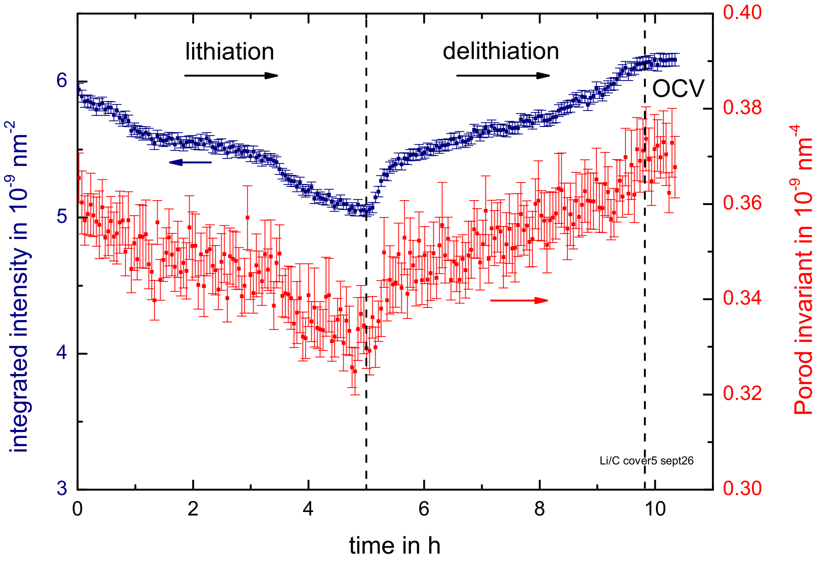

Figure 5.19.: Integrated intensity $\Gamma = \int d\Sigma/d\Omega(q)\,dq$ and Porod invariant $\int q^2\,d\Sigma/d\Omega(q)\,dq$ versus time during lithiation and delithiation (at C/5) of graphite vs. Li (cell ID sept26), scaled to empty beam.

The integrated intensity Γ for the evaluated medium q-range of the data of figure 5.16 is $0.7 \cdot 10^{-9}\,\mathrm{nm}^{-2}$ for the empty pouch background, $4.4 \cdot 10^{-9}\,\mathrm{nm}^{-2}$ for the dummy cell with all inactive materials and $18.7 \cdot 10^{-9}\,\mathrm{nm}^{-2}$ for the full cell. Together, all inactive materials make up only 23% of the full cell figure. The active material integrated intensities from 5.17 are $11.3 \cdot 10^{-9}\,\mathrm{nm}^{-2}$ for the cathode NMC particles and $6.1 \cdot 10^{-9}\,\mathrm{nm}^{-2}$ for the anode graphite, in relative terms 65% and 35% of the active materials. Summing up the integrated intensity contributions in a model full cell we can assume 23% for inactive background, 50% ($= 77\% \cdot 65\%$) for cathode and 27% ($= 77\% \cdot 35\%$) for anode.

We will see that for a variety of cells the integrated intensity (and equally the Porod invariant) is varying as a function of state of charge. During rest periods the signal remains constant and varies only within the error range, see e. g. figure 5.19 at the end of delithiation. Possible explanations for this operando SANS scattering data will be discussed in the following.

Scattering length density

As already mentioned, scattering in a battery system occurs at the separated layers of active and inactive material. Contributions by pouch, separator, anode and cathode add up incoherently. Active materials are the only components that change during the in situ experiment by shuttling Li-ions from one electrode to the other. Active material particles change with respect to chemical composition by (de)intercalating Li-ions. The arrangement and morphology of the particles is not expected to change much during the first cycles. NMC and graphite are established battery materials that can undergo thousands of cycles in commercial batteries. There is of course a slight change in volume of the particles - ca. 10% for graphite [94] and 1% for NMC [155]. In the first approximation this influence is however neglected. The experimental data below will show that indeed this assumption holds true.

We have seen that the scattering cross section and integrated intensity are functions of the scattering length density. This material constant can be calculated for relevant battery materials in lithiated and delithiated state. SLD (ρ) values are shown in the fourth and seventh column of table 5.3. Note that density and therefore volume change is already considered in the calculation. The calculation was done with the SLD calculator of the SASfit program [123]. As deduced in equations 5.32, 5.50 and 5.51, the scattering cross section or integrated intensity is (for two adjacent phases) proportional to the relative contrast factor, which is the squared difference of the SLDs of the adjacent phases, $\Delta\rho^2 = (\rho_1 - \rho_2)^2$.

Relevant phases that have to be compared are the phases within the active particle and all phases with respect to surrounding electrolyte. $\Delta\rho^2$-values for the relevant material pairs are given in the eighth column of table 5.3. During charging of the full cell, the relative contrast of graphite to the electrolyte changes from $40 \cdot 10^{20}\,\mathrm{cm}^{-4}$ for pure C to $26 \cdot 10^{20}\,\mathrm{cm}^{-4}$ for LiC_6, a change of -34%.

On the cathode side the contrast between the electrolyte and LiNMC as well as between electrolyte and $Li_{0.5}$NMC varies from 6.5 to $8.0 \cdot 10^{20}\,\mathrm{cm}^{-4}$, a change of 23% but on a lower absolute level. The relative contrast between NMC phases within the cathode particle is below $0.08 \cdot 10^{20}\,\mathrm{cm}^{-4}$ and can be neglected. Also the relative contrast between the solid phases within the anode can be neglected as table 5.3 shows: graphite to LiC_{12} and LiC_{12} to LiC_6 have only relative contrast factors below $0.5 \cdot 10^{20}\,\mathrm{cm}^{-4}$. Thus, the dominating scattering contributions stem from the large relative contrast factors of active material to electrolyte. Additionally in a half cell, Li to electrolyte has a relative contrast factor of $4.7 \cdot 10^{20}\,\mathrm{cm}^{-4}$ which is not negligible, so changes of morphology (larger surface) could be visible.

As already discussed in section 5.2.3, the analysis is complicated by the fact that the coherence length is much smaller than the particle diameter. The neutron does not interact with all phases at once but only with those in its vicinity. Therefore,

SoC	**phase A**	density A in g/cm^3	SLD A in 10^{10} cm^{-2}	**phase B**	density B in g/cm^3	SLD B in 10^{10} cm^{-2}	**squared scatter. contrast** $\Delta\rho^2$ in 10^{20} cm^{-4}	$\Delta\rho^2$ rel. to largest value
0%	C	2.27	7.5643	electrolyte	1.15	1.2407	39.99	100%
50%	LiC_{12}	2.23	6.9331	electrolyte	1.15	1.2407	32.40	81%
100%	LiC_6	2.20	6.3597	electrolyte	1.15	1.2407	26.20	66%
0%	LiNMC	4.77	3.7911	electrolyte	1.15	1.2407	6.50	16%
50%	$Li_{0.75}NMC$	4.68	3.9291	electrolyte	1.15	1.2407	7.23	18%
100%	$Li_{0.5}NMC$	4.60	4.0757	electrolyte	1.15	1.2407	8.04	20%
	polypropylene $(CH_2)_n$ (inner pouch, separator)	0.95	-0.3379	electrolyte	1.15	1.2407	2.49	6%
	6-nylon ($C_6H_{11}NO$) (outer pouch)	1.08	0.8025	air	0.00	0.0043	0.64	2%
	Graphite	2.27	7.5643	LiC_{12}	2.23	6.9331	0.40	1%
	LiC_{12}	2.23	6.9331	LiC_6	2.20	6.3597	0.33	1%
	Li	0.56	-0.9232	electrolyte	1.15	1.2407	4.68	
	LiNMC	4.77	3.7911	$Li_{0.5}NMC$	4.60	4.0757	0.08	

Table 5.3.: Overview of SLD values and squared scattering contrast, i.e. the relative contrast factors, for two-phase combinations of typical battery materials. Densities according to structures taken from [94] and [156]. Electrolyte is EC:EMC(3:7) with 1M $LiPF_6$. SLD calculated with SASfit.

we have to evaluate $\Delta\rho^2$ in all of the possible coherence volumes. For two phases (solid plus electrolyte) this is just one $\Delta\rho^2$. For three or more phases the cross section from a single coherence volume is a smooth function of the various $\Delta\rho^2$s and the contributing volume fractions inside the coherence volume. All the possible coherence volumes are added up, now incoherently, so that the total cross section or integrated intensity is of course proportional to the typical coherence volume expressions weighed by the number of relevant coherence volumes. So, for a simple two phase system with particles larger than the coherence length in electrolyte, the total scattering will be proportional to $\Delta\rho^2$ from particle to electrolyte and proportional to the volume fraction of all shells with the thickness of one coherence length.

The coherence length gives us some kind of local $\Delta\rho^2$ resolution. If we imagine the signal from a slowly lithiating particle, we can assess the scattering contributions. All phases deep within the particle give a negligible signal because their $\Delta\rho^2$ values are small. We are left with contributions from the outer shell where electrolyte and active particle coexist in the same coherence volume. I. e. we have a coherent shell in the active particle with the width of one coherence length, as shown in figure 5.20. As long as phases in this shell are changing and as long as they have significant change in $\Delta\rho^2$ to electrolyte, we see a change in overall scattering signal. In a graphite particle system: while a particle is lithiated the SANS signal changes as long as the lithiation front moves through the coherent shell (figure 5.20, a). The SANS signal will remain unchanged when further lithiation occurs deep inside the particle and the shell remains at a stable phase, say LiC_{12} or LiC_6 (figure 5.20, b), because of the low relative $\Delta\rho^2$.

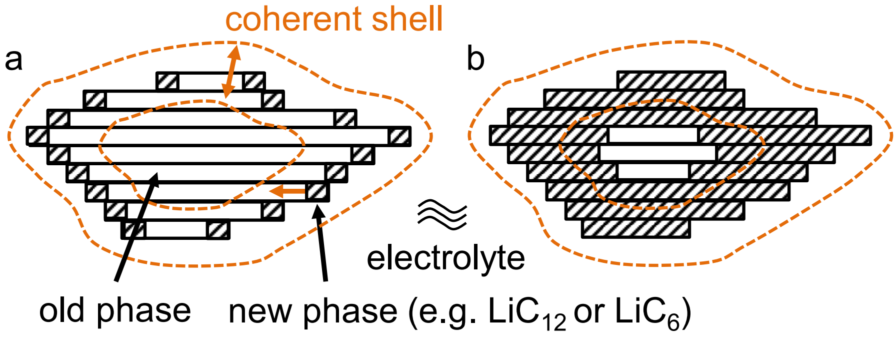

Figure 5.20.: The two different situations for SANS contrast: a) new phase growing across the coherent shell within reach of surrounding electrolyte and b) new phase growing only in the interior of the particle.

5.3.3. Half cell measurements

A half cell with a Li counter electrode is the simplest system to study the lithiation of materials and will be examined first. In this cell, we can directly get the potential of the graphite electrode from the cell voltage. Of course, an assembly with three electrodes, i. e. with a current-free Li reference electrode would be even better because overvoltages may blur the potential signal on the current bearing Li counter electrode. In a pouch cell, it is unfortunately not straightforward to implement reference electrodes and they have been omitted in most of the cells shown. For slow C-rates, the cell potential (current-bearing Li to electrode) should nevertheless give a good estimation of the real electrode potential.

Li contribution to half cell

We have already seen that inactive materials do not substantially contribute to the SANS signal and they are constant anyway. But how would a Li counter electrode influence the signal and how would it change during cycling? To answer this question a reference experiment has been undertaken. A symmetric Li/Li cell was built, brought to the SANS experiment without formation and cycled in the same way as the Li/C half cell, i. e. with the same current. Experimental cycling data is shown in appendix B.2. The cell was cycled for two hours with a current of 2.1 mA corresponding to a rate of C/5 for the Li/C half cell in one direction and for two more hours in the other direction. Thereby Li was stripped at one electrode and plated at the other one and reverse. The SANS integrated intensity (y-axis) is shown in figure 5.21 versus an x-axis that represents the transferred charge mapped to the capacity axis of the Li/C half cell for comparison. The integrated intensity signal increases slightly during initial stripping and plating from and to pristine Li surfaces. The signal increases further also during subsequent reverse cycling. The relative change during charge transfer of 0.4 C is around 3 to 4% in both directions.

A possible explanation for this increase is that during cycling a dendritic or mossy Li micro-structure forms that has a relatively high surface area which gives stronger contrast in neutron scattering. Dendritic Li plating has long been an issue for Li metal and also in graphite anodes and is detrimental to battery lifetime and safety [157]. Recent research suggests that especially during plating mossy structures form from micro-sized dendrites [158, 159]. These dendrites are often badly connected to the substrate and electrical resistance is high so that in reverse mode stripping is actually preferred from the underlying substrate which could be seen sometimes as creation of holes in the surface. So as a consequence, mossy Li can build up over time during repeated cycling. The exact growth and stripping mechanisms depend however on many parameters such as current density, electrolyte

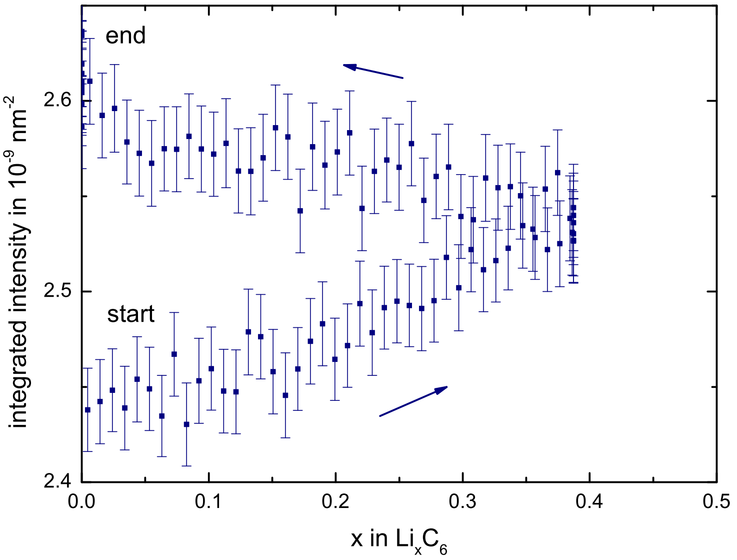

Figure 5.21.: Li/Li pouch cell (cell ID sept33) measured with SANS while shuttling Li with standard C-rate C/5. Capacity axis related to equivalent charge in the Li/C half cell.

and temperature. Figure 5.22 shows the build-up of mossy Li in a Li/Li pouch cell that underwent a formation similar to the Li/C half cell, i. e. two cycles (one cycle defined as a charge transfer equal to the capacity of the reference Li/C cell and reverse) at currents equivalent to C/10 and two cycles at C/5. So this cell had in total around 8 times more charge transferred than in the fresh Li/Li cell measured in situ during the SANS experiment. In figure 5.22 (a) the smooth pristine Li surface (in the upper right) is seen, as well as the patches of mossy Li that formed already from the few formation cycles. Figure 5.22 (b) shows in detail the micro-sized dendrites that form the mossy structure. The dendrites are obviously too big to be seen as an interference pattern in the SANS signal but the higher surface area leads to a higher scattering contribution. In conclusion, there is a contribution to integrated intensity from the creation of mossy high surface area structure on the Li counter electrode.

So, how does the Li scattering contribution compare to the graphite scattering on a total scale? Here, we make a quick estimation of the relative change; in the next section we will turn to a full quantitative analysis. Figure 5.23 shows the change of integrated intensity for both types of cell, Li/Li and Li/C, on the same charge axis. Current density is also equal and both are shown with the same absolute scaling to empty beam, so that it is possible to estimate the influence of Li to the half cell SANS signal. For a charge transfer of 1C the integrated intensity of the

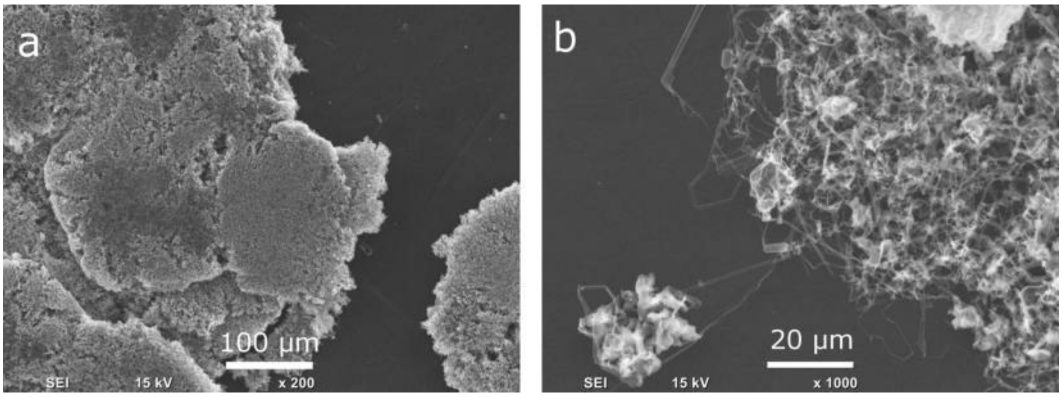

Figure 5.22.: Li/Li pouch cell (cell ID sept21) electrode after formation cycles. a) Fresh, smooth areas (dark) and areas with mossy plated Li are identified on the electrode. b) The zoomed image shows the micro-dendritic structure of the mossy Li.

Li/Li cell changes by ca. +8 to +10% (extrapolated from the slope of the data shown in figure 5.21). In contrast, for the Li/C cell we observe a change of -15% during full charge. In summary, the Li/C half cell seems to be dominated by the decrease in $\Delta\rho^2$ of graphite which is -34%.

In the Li/Li cell there is of course double the amount of Li but the intensity change should be comparable since the transferred charge and thus the amount of newly created mossy Li is equal to the Li/C cell. Mossy Li is created during plating, so in the half cell the Li contribution should only change (increase) during Li plating (on Li), thus during delithiation of graphite, i. e. charging of the half cell. In summary, the overall change of integrated intensity is not caused primarily by Li but we would expect Li to increase the signal slightly on delithiation of graphite. Indeed, data in figure 5.23 confirms that the endpoint of integrated intensity after lithiation and delithiation is higher than at the start. Another evidence that the changes in integrated intensity mostly stem from graphite is given by the fact that any signal from mossy Li is linear in transferred charge, unlike for graphite.

Half cell SANS

We can now turn to the Li/C half cell system in more detail. Figure 5.24 shows the relative change in integrated intensity for the Li/C half cell in detail. Data points are shown with relevant error bars. Additionally a smoothed averaging curve is calculated by the Savitzky-Golay method (3$^{\text{rd}}$ order polynomials). In parallel, the cell potential for lithiation (down to 0.01 V) and then delithiation (up to 1.5 V) of graphite is shown on the same capacity axis which is given as the utilization x in Li_xC_6 based on measured charge transfer set in relation to the amount of active material which was weighed in for the electrode. Further details are given

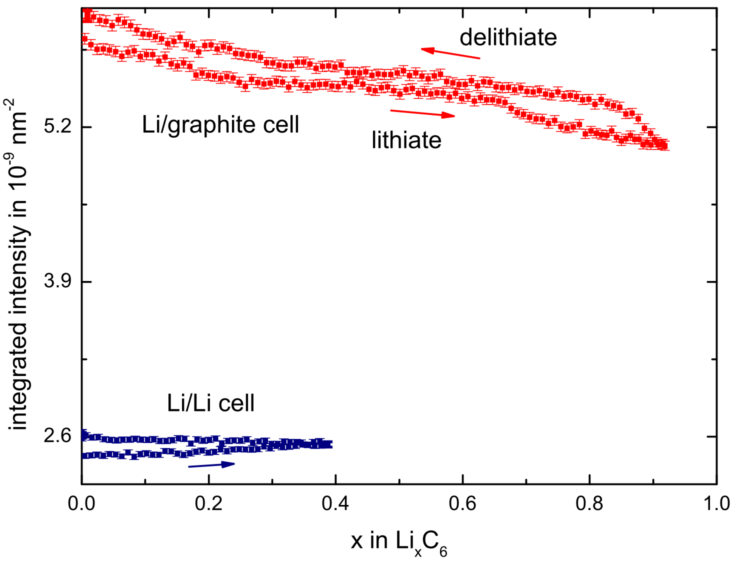

Figure 5.23.: Evolution of integrated intensity signal Γ during charge transfer of 1C for Li/Li pouch cell (sept33) vs. Li/C pouch cell (sept26). The change in Γ from $x = 0$ (fully delithiated) to $x = 1$ (fully lithiated) is $+1.2 \cdot 10^{-9}\,\mathrm{nm}^{-2}$ for the Li/C cell, thus much higher than the variation observed for the Li/Li cell which is only $-0.2 \cdot 10^{-9}\,\mathrm{nm}^{-2}$ from $x = 0$ to an extrapolated $x = 1$.

in appendix B.4; an error of some percent in utilization is plausible. More than 90% of the theoretically expected capacity from anode mass is achieved.

We observe that the integrated intensity of the SANS signal is a function of capacity and is reversible. The curve features plateaus and is slightly different for lithiation and delithiation of graphite so that there is a certain hysteresis. The measured total change in integrated intensity during lithiation is -15% with a plateau at half of this distance. From table 5.3, we see a change in $\Delta\rho^2$ contrast to electrolyte of -19% from C to LiC$_{12}$ and another -15% down to LiC$_6$, so in total -34%.

We can also use equation 5.57 to actually calculate the integrated intensity and get equation 5.60. We know the total integrated intensity value of the Li/C cell and we can estimate the relative shares of the three terms to the sum. For the half cell the components were not measured individually, but one can still give reasonable estimates. First, in the full cell the inactive materials background was measured independently to be between 20 to 30% for a pouch cell, compare figure 5.17. Second, from figure 5.23 we get integrated intensities of $5.9 \cdot 10^{-9}\,\mathrm{nm}^{-2}$ for Li/C and of $2.4 \cdot 10^{-9}\,\mathrm{nm}^{-2}$ for Li/Li. This gives an upper limit for the inactive material plus the Li electrode contribution of $2.4/5.9 = 41\%$. Thus, a choice of 30% contribution

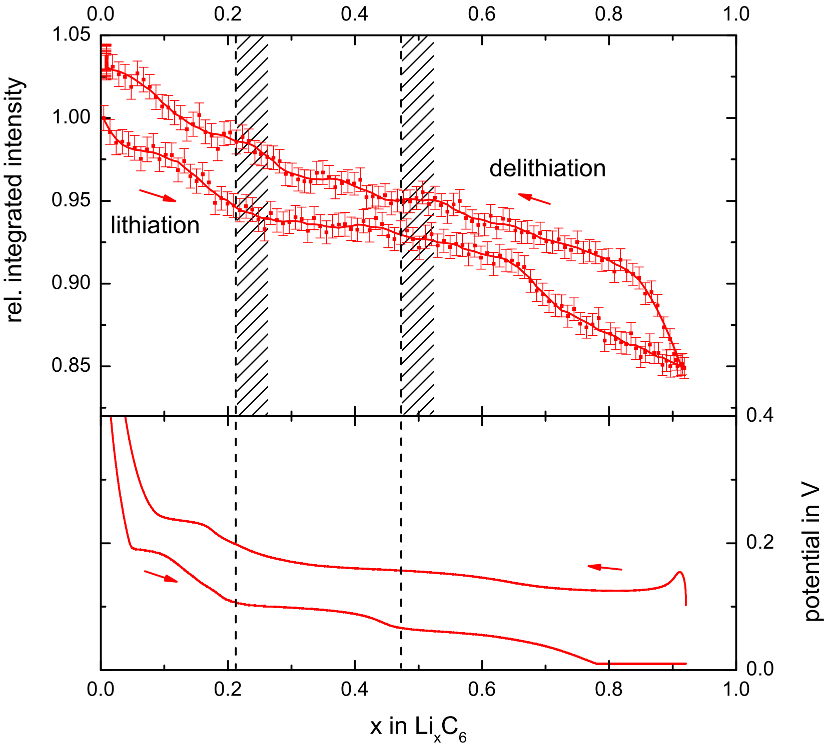

Figure 5.24.: Evolution of integrated intensity signal Γ during lithiation and delithiation (rate C/5) of graphite electrode and related cell potential in a Li/C half cell (cell ID sept26), relative to highest value. Error bars and smoothed curve (Savitzky-Golay) are shown. Areal capacity of the graphite electrode 1.63 mAh/cm^2.

by inactive background materials plus 10% contribution by the lithium electrode in the Li/C half cell seems reasonable. Third, the graphite/electrolyte phases will then contribute the remaining 60%.

When putting in the percentage, the measured total integrated intensity (in delithiated state) and the known $\Delta\rho^2$s into equation 5.60 the only unknowns are the two geometry factors c_2. So, we can calculate them, e. g. $10\% \cdot 5.9/4.68 = 0.126$, units omitted. This reproduces the total integrated intensity in delithiated state and allows us to vary the $\Delta\rho^2$ to study the change upon cycling. Together, the integrated intensity is given by (in units of $10^{-9}\,\text{nm}^{-2}$):

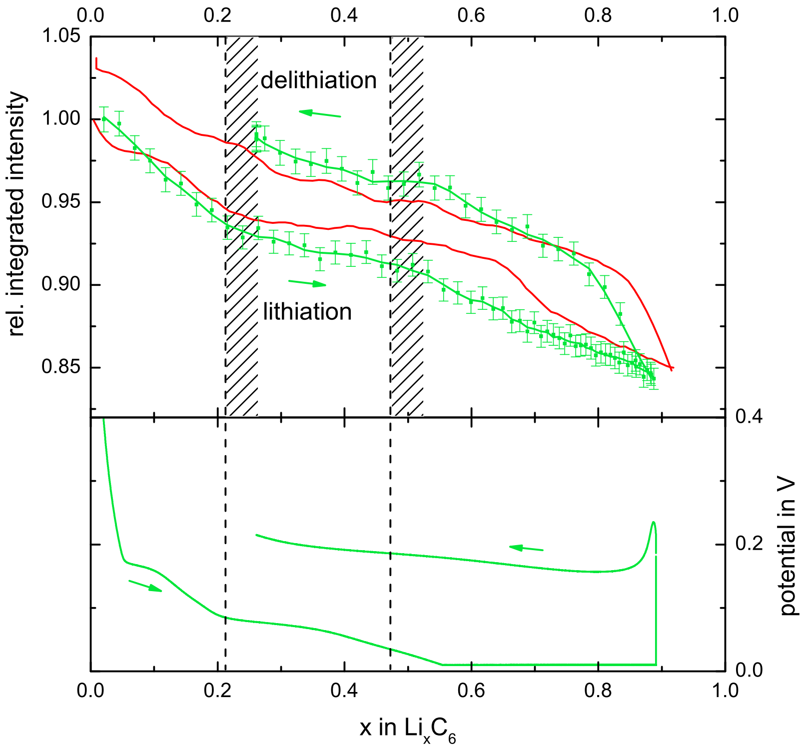

Figure 5.25.: Evolution of integrated intensity signal Γ during lithiation and delithiation of graphite electrode and related cell potential in a Li/C half cell (cell ID sept26, areal capacity 1.63 mAh/cm^2), relative to highest value. Rates C/5 (red) and C/2 (green) are shown. Error bars and smoothed curve (Savitzky-Golay) for C/2 plus smoothed curve for C/5.

$$\begin{aligned}\Gamma_{\text{total}} &= \underbrace{c_0'}_{\text{inactive}\,\equiv 30\%} + \underbrace{c_2 \Delta\rho^2{}_{\text{Li/electrol}}}_{\equiv 10\%} + \underbrace{c_2 \Delta\rho^2{}_{\text{graphite/electrol}}}_{\equiv 60\%} \\ &= 1.77 + \underbrace{0.126\, \Delta\rho^2{}_{\text{Li/electrol}}}_{\Delta\rho^2 = 4.68} + \underbrace{0.089\, \Delta\rho^2{}_{\text{graphite/electrol}}}_{\Delta\rho^2 = 40\ \text{to}\ 26.2} \qquad (5.60) \\ &= 5.9\,(\text{delith})\ \text{to}\ 4.7\,(\text{lith})\,.\end{aligned}$$

The modeled integrated intensity varies from 5.9 (delithiated) to $4.7 \cdot 10^{-9}\,\text{nm}^{-2}$ (lithiated) which is a relative change of -21% and agrees well to the experimentally observed value of -15%. Half-way during lithiation, for $x = 0.5$ in $\text{Li}_\text{x}\text{C}_6$, the calculated relative change is -11% which again reasonably well matches the experimental value of around -7%.

In the following, we want to understand the shape of the integrated intensity signal and compare the existence of plateaus to the theory of a staged lithiation of the graphite particle. First, we can look at the potential curve to identify the formation of the stages. The kinks in the curve, as indicated by the dashed line in figure 5.24, mark the beginning of a stage during lithiation. For delithiation the potential curve is smeared out and plateaus cannot easily be identified. In general, there is an overvoltage of ca. 100 mV at this rate in the pouch cell system, i. e. the difference between lithiation and delithiation potential curve. The shaded area represents some shell volume capacity which is relevant for scattering contrast.

For the same half cell at another C-rate of C/2, figure 5.25, the same trend in integrated intensity can be observed. Note, that the overpotential is higher, smearing out the plateau transitions and driving the potential faster to the lower cut-off during lithiation. Due to restricted measurement time at the reactor facility the experiment was ended before full delithiation was completed. Figure 5.25 shows C/2 data with error bars and C/5 data as above for comparison.

Half cell XRD

In order to confirm again that the beginning of a plateau represents a new phase in the graphite, we have measured the same half-cell in an in situ XRD experiment. The measurement was carried out by Stefan Seidlmayer with a PANalytical Empyrian diffractometer with Mo tube at 40 mA and 55 kV and $\lambda = 0.70932\,\text{nm}$ ($\text{K}_{\alpha1}$ and $\text{K}_{\alpha2}$). One pattern was collected in 6 min. Figures 5.26 and 5.27 show the measured reflections during in situ lithiation and delithiation. As already discussed in section 5.1.1, during lithiation a continuous lattice spacing shift can be observed in the beginning. Above ca. 20% SoC (related to $\text{Li}_\text{x}\text{C}_6$) the 0 0 2-reflection of LiC_{12} is appearing, in good agreement with the onset of the second plateau. After 50% SoC the 0 0 1-reflection of LiC_6 appears, in agreement with the onset of the third plateau even though the voltage is driven down to cut-off fast due to overvoltage.

Figure 5.27 shows the same trend in reverse for delithiation. Starting from 100% SoC at the right, the 0 0 1-reflection of LiC_6 vanishes until 50% SoC is reached. First, the 0 0 2-reflection of LiC_{12} increases where LiC_{12} is the product of LiC_6 transformation and decreases later where LiC_{12} is transformed to lower lithiated phases until it has mostly gone at ca. 25% SoC.

Together, we have confirmed that in the specific half-cell that was measured here, there is indeed a staged transition from lower lithiated phases to the two well known stages and the potential curve indicates the coexistence of two phases.

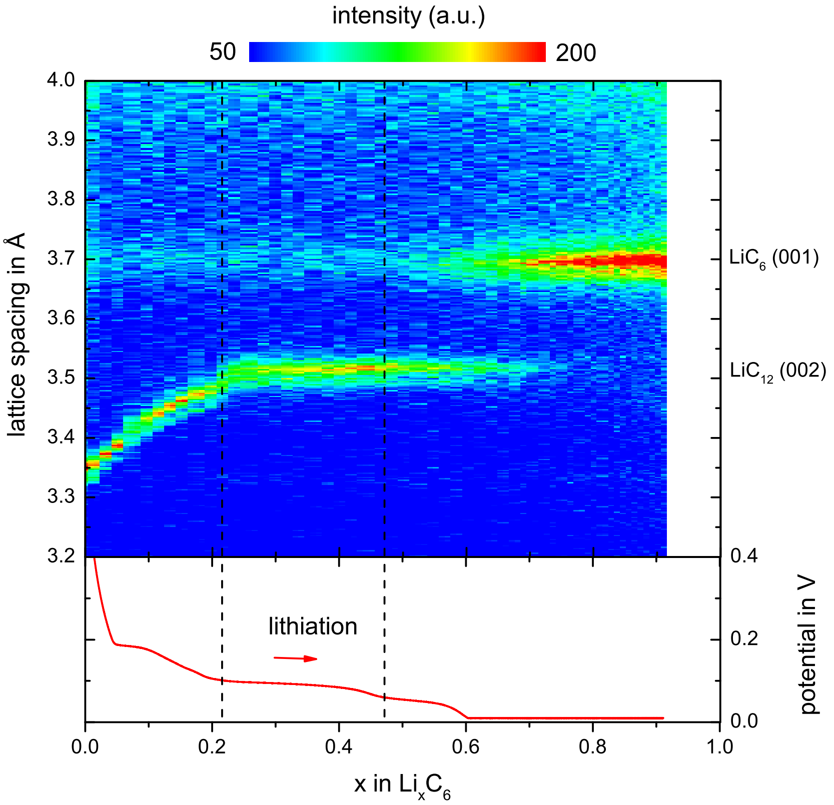

Figure 5.26.: Evolution of X-ray diffraction pattern during lithiation of graphite electrode and related cell potential in a Li/C half cell. Cell ID sept26, cycled at C/5 after the SANS experiments, areal capacity 1.63 mAh/cm^2.

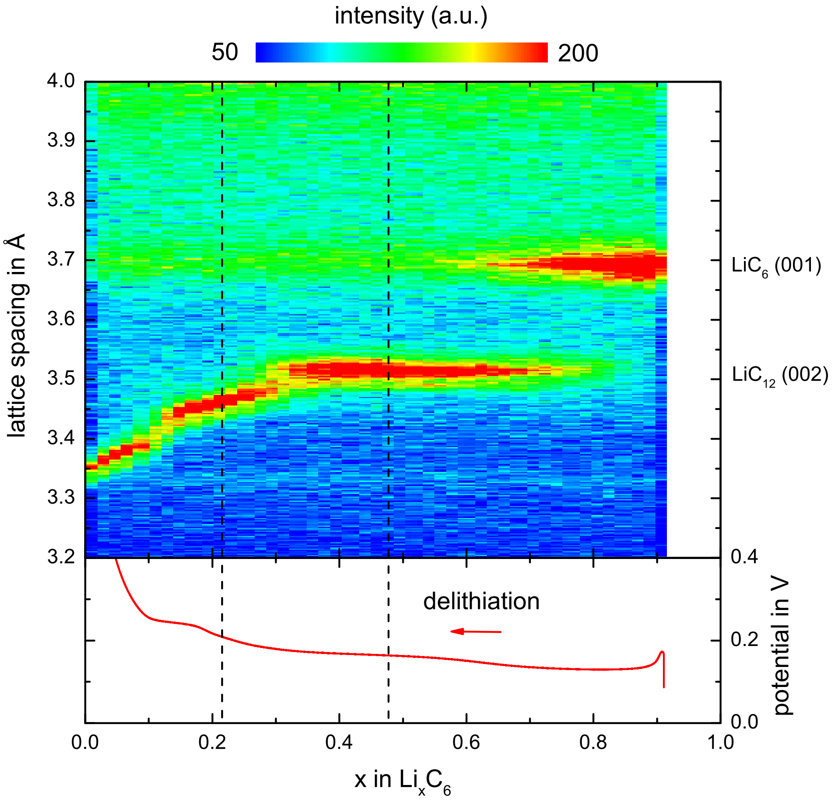

Figure 5.27.: Evolution of X-ray diffraction pattern during delithiation of graphite electrode and related cell potential in a Li/C half cell. Cell ID sept26, cycled at C/5 after the SANS experiments, areal capacity 1.63 mAh/cm^2.

Half cell model and results

Having simultaneous data from potential, XRD and SANS, we will now try to set up a model to explain the observed SANS data. In section 5.3.2, we have already made the hypothesis that the SANS signal changes when there is a phase transformation (and thus a change of SLD) in the outer shell within the coherence length, the "coherence shell". The signal is constant when lithiation and phase transformation occur in the interior of the particle where relative SLD contributions between the phases are negligible and the strong contrast to electrolyte is out of reach.

Lithiation model

Figure 5.28 shows this model approach for the lithiation of a graphite particle via phase propagation from the outside to the inside, from left to right. Above the schematic model curve, smoothed data at a rate of C/5 and C/2 is shown and the lithiation of an exemplary particle is illustrated. The existence of the two main stages is indicated below. First, the particle is lithiated by formation of the lower lithiated phases. Due to the continuous multi-phase behavior we expect no clear geometrical separation of phases and a continuous shift in SLD and contrast. At the point where the whole particle is lithiated to the phase LiC_{18} we reach 33% SoC (SoC defined with respect to the full cell, so $x = 1$ in Li_xC_6 is equivalent to SoC = 1). Further lithiation can only take place if LiC_{12} is formed and this phase propagates from the surface into the particle (first particle image). The phase volume fractions in the relevant coherence volumes and thus the SANS signal will change as long as phase transformations occur in the coherence shell. The SANS integrated intensity will stay constant once the shell is full and lithiation is only taking place in the inside. In an ideal particle we can calculate this to happen earliest at $\mathrm{SoC} \leq 1/3 + (1/2 - 1/3) \cdot C_{\mathrm{rel,shell}}$ (point 1), where $C_{\mathrm{rel,shell}}$ is the relative capacity share of the coherence shell in relation to the whole particle. Here we assumed the particle was fully lithiated by a hypothetical phase LiC_{18} before LiC_{12} was formed. The capacity uptake of the shell during the transformation is proportional to the difference between those two phases. A lower or incomplete lithiation in the interior of the particle shifts point 1 to lower capacities. Then at ca. 50% SoC (point 2), the phase LiC_6 will be formed and again the phase propagates from the surface into the particle (particle image 2 and subsequent). The SANS integrated intensity will change again until the shell is completely transformed to LiC_6. This point is reached at $\mathrm{SoC} \leq 1/2 + 1/2 \cdot C_{\mathrm{rel,shell}}$ (point 3). Subsequent lithiation happens only in the interior of the particle and yields no change in scattering contrast and SANS integrated intensity.

The width of the shell lithiation region is given by the relative volume share of

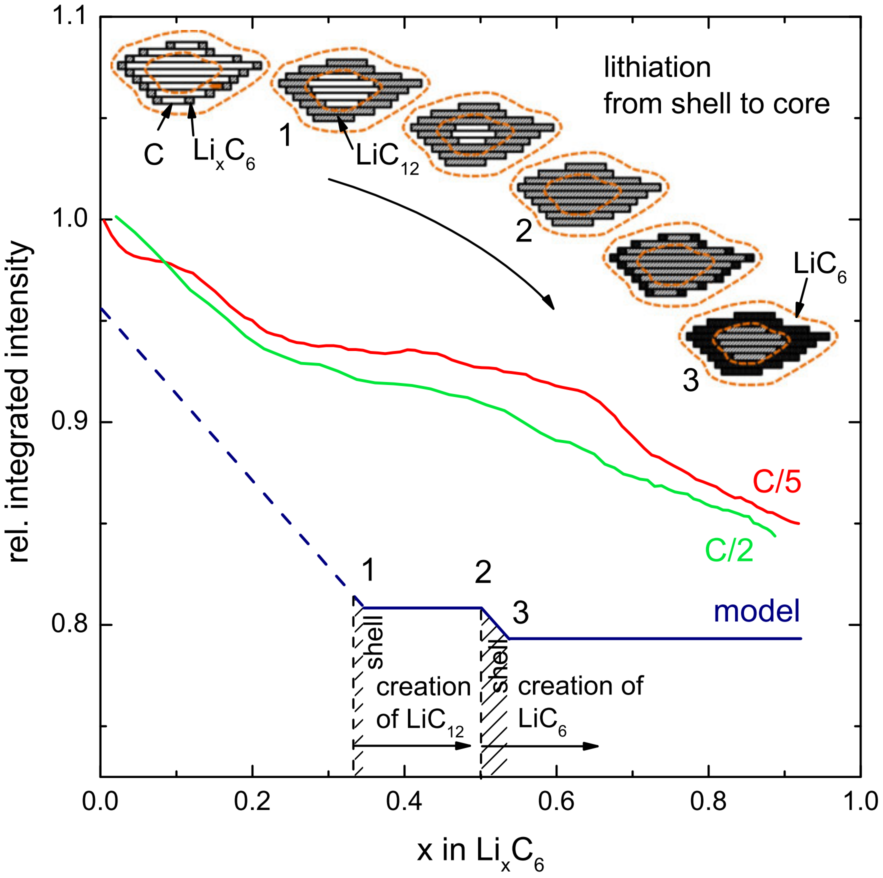

Figure 5.28.: Li/C half cell lithiation. Schematic model in comparison to smoothed experimental data. Single graphite particle illustrated above and coexistent phases below.

the coherence shell $C_{\text{rel,shell}}$. Assuming a coherence length of, say, 200 nm (i. e. the coherence length of 120 nm that was estimated from theory before plus some extra accounting for particle size distribution, roughness and some surface porosity) and a spherical graphite particle of 20 µm diameter, we arrive at a relative volume share of the shell of $C_{\text{rel,shell}} = 6\%$. Point 1, 2, 3 are then calculated with the equations above to be at 34%, 50% respectively 53%. The related capacity is illustrated in the figures by the shaded area. For non-spherical potato-like or even platelet-like shapes this figure will vary in the range of several percent.

In summary, the schematic model explains plateaus in the SANS integrated intensity by the lithiation in the interior of the particle, invisible due to lack of scattering contrast. Changes occur in the beginning at mixed phases and later during lithiation of the outer shell. The two plateaus related to formation of LiC_{12} and LiC_6 in the bulk interior of the particle can be identified in the experimental data for both C-rates. The first plateau correlates quite well in figure 5.28 with point 1 near 30% and 2 near 50%. The second plateau is however much less clear. For C/5 it sets in at above 65% SoC, much higher than expected for the given coherence shell which would end at point 3 near 53% SoC. Furthermore, the experimental curve does not reach a real plateau but is still (though less) decreasing. For C/2 this is even more the case. The steepness decreases near 60% but is still considerable.

As for many systems, the discrete nature of a simple one particle model is smoothed out in the real experiment by factors such as multi-dispersity and all sorts of inhomogeneities. For a thick real-life electrode, as used here, there is of course a significant distribution of particle shapes and sizes and there is also some inhomogeneity in lithiation throughout the electrode. Two major parameters can also shift the characteristic points (1,2,3): A bigger coherence shell volume or a shape with more relative surface volume than a sphere shift the onset of the plateaus (point 1 and 3) to the right to higher capacities. Inhomogeneity in the single particle, i. e. an incomplete lithiation in the inner particle before nucleation of the next phase on the surface, shifts the whole curve to the left to lower capacities. One would expect these inhomogeneity effects to be more pronounced for higher C-rate, in accordance with the experimental results where the plateaus are less prominent for C/2. During lithiation of graphite Li is stripped from the Li counter electrode and we do not expect the build-up of mossy Li that would contribute to a changing (increasing, as shown above) background.

Delithiation model

During delithiation a different trend in SANS integrated intensity is observed. Starting from the right in figure 5.29, the fully lithiated phase transforms to lower lithiated LiC_{12} at the surface which propagates into the particle. Literature (see section 5.1.1) suggests that indeed lower lithiated phases propagate from outside to inside. The delithiation process is thus not just the reverse of lithiation where the core would be delithiated first since it was the latest part which was fully lithiated. Following the outside to inside model, a LiC_{12} surface shell will evolve and scattering contrast and SANS integrated intensity will change immediately. Once the coherence shell is completely transformed to LiC_{12} where $\mathrm{SoC} \leq 1 - 1/2 \cdot C_{\mathrm{rel,shell}}$ (point 1', calculated at 97%) all phase transformation happens in the interior and SANS integrated intensity will stay constant. Below SoC 50% lower lithiated phases than LiC_{12} have to be formed which will probably also start from the surface. Contrast and integrated intensity will change again (point 2'). At even lower SoC a continuous shift will most likely result in a steady change in scattering contrast and integrated intensity until the pure graphite phase is reached.

Experimental data in figure 5.29 shows indeed a steep increase at the start of

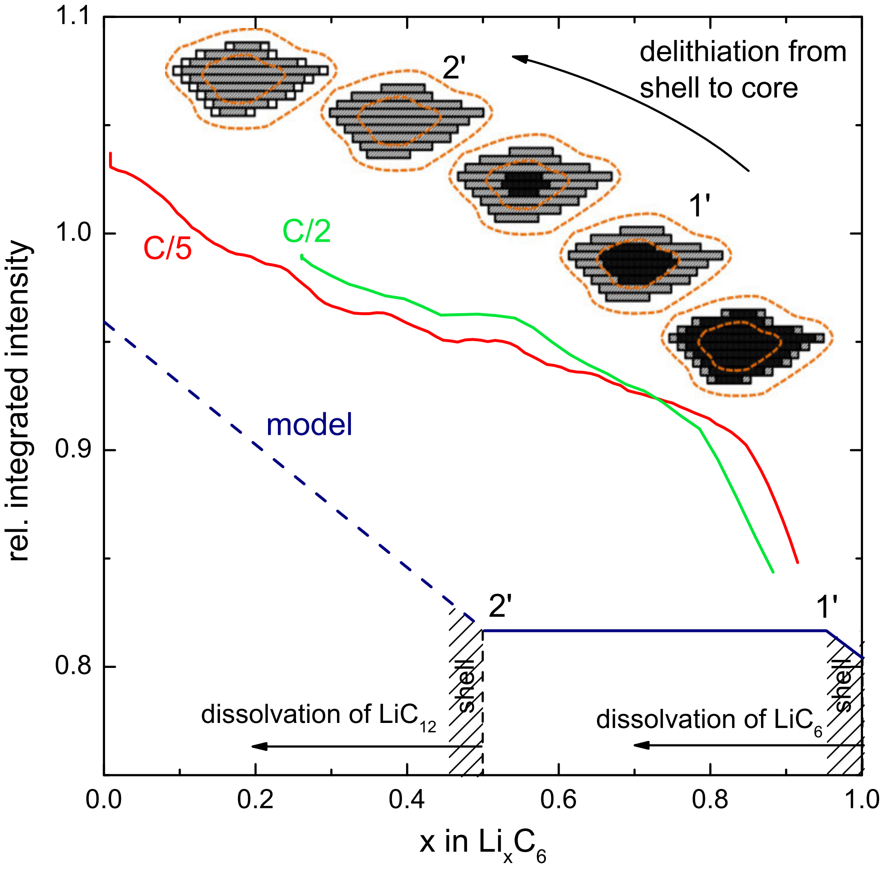

Figure 5.29.: Li/C half cell delithiation. Schematic model in comparison to smoothed experimental data. Single graphite particle illustrated above and coexistent phases below.

delithiation. The end point of lithiation does not reach full utilization $x = 1$. Since there is a virtually endless reservoir of Li on the counter electrode side, loss of active Li should not be a problem but mechanical stress and deterioration can lead to contact loss and loss of active, participating material. In this case, participating particles are expected to be fully lithiated and the non-participating particles are not changing significantly during lithiation. Assuming a fully lithiated particle at the end of lithiation, delithiation can be illustrated as shown in the images in the upper part of figure 5.29. Upon delithiation from 90% SoC to 84 and 80% (depending on C-rate), integrated intensity increases sharply until it levels off with a small slope. Between 50% and 40% SoC the slope increases again, as expected by further delithiation of the surface shell. The fact that the curve in the middle between (ideally) point 1’ and 2’ is not constant but rather increases at a small slope could also partly be explained by the Li contribution. During delithiation

Li metal is re-plated on the Li counter electrode and forms a mossy Li structure which was shown in the Li/Li cell to give an increasing scattering contribution resulting in an increase in the integrated intensity. This could also explain why the lithiation (C/5) reaches a higher relative integrated intensity of 1.04 back at 0% SoC than at start. Additional mossy Li was created in the cycle.

In total, the surface-to-interior phase separated lithiation and delithiation model of the graphite particle together with the concept of coherence length is able to explain the observed SANS integrated intensities qualitatively and also quantitatively (calculated relative changes within 25% error).

5.3.4. Full cell measurements

NMC contribution to full cell

The second part of the experiment is the lithiation of graphite in a full cell versus NMC. Also for this case, we can estimate the contribution to the total measured scattering, e. g. SANS integrated intensity or the Porod invariant. From figure 5.17 we can see that anode and cathode active materials contribute most to scattering. The interesting question is, how they change upon cycling. Table 5.3 shows the change in SLD and the change in contrast $\Delta\rho^2$ versus the surrounding electrolyte. Contrasts in the interior of the particles are neglected because they are small. $\Delta\rho^2$ for graphite versus electrolyte changes from 40.0 to $26.2 \cdot 10^{20}\,\mathrm{cm}^{-4}$ during lithiation (i. e. charging in a full cell) whereas NMC does only change from 6.5 to $8.1 \cdot 10^{20}\,\mathrm{cm}^{-4}$ during charge. Anode and cathode are far away from each other on the length scale of coherence length and therefore they add up incoherently. In summary, we expect the change in integrated intensity to be dominated by graphite. Another aspect is that NMC does not show staging so that no discrete plateaus in SANS integrated intensity are expected to arise from NMC . These could only be explained by the staging behavior of graphite.

Full cell SANS

The results of several full cell measurements at SANS-1 are presented in the following. Parts of the work, done in 2013 and 2014 with the cell ID nov1, were already published together with S. Seidlmayer et al. [16].

Figure 5.30 shows how the integrated intensity of a full cell and also the Porod invariant change during charge (i. e. lithiation of graphite) and discharge (i. e. delithiation of graphite) between 3 to 4.2 V. The trend for both SANS measures is the same, but the relative error of the integrated intensity is much lower and this measure will be studied in the following.

Relative integrated intensity data of the first and also of the second cycle is shown in figure 5.31, but plotted against capacity or utilization x of $\mathrm{Li_xC_6}$. The integrated intensity is normalized to a value of 1 at the first integrated intensity value of each cycle. This allows easy comparison with other cells which are normalized as well. Integrated intensity changes reversibly with charge transfer, i. e. with changes in x. In accordance with the half cell results, the integrated intensity decreases during lithiation of graphite and increases again during delithiation of graphite. Again, two steeper regions and two plateaus can be identified during lithiation and one broad plateau can be identified during delithiation. The shape of the curves for first and second cycle looks very similar and the relative shift in y-direction is only caused by the fact that the first data point of the second cycle was not measured at fully discharged state but nevertheless normalized to 1.

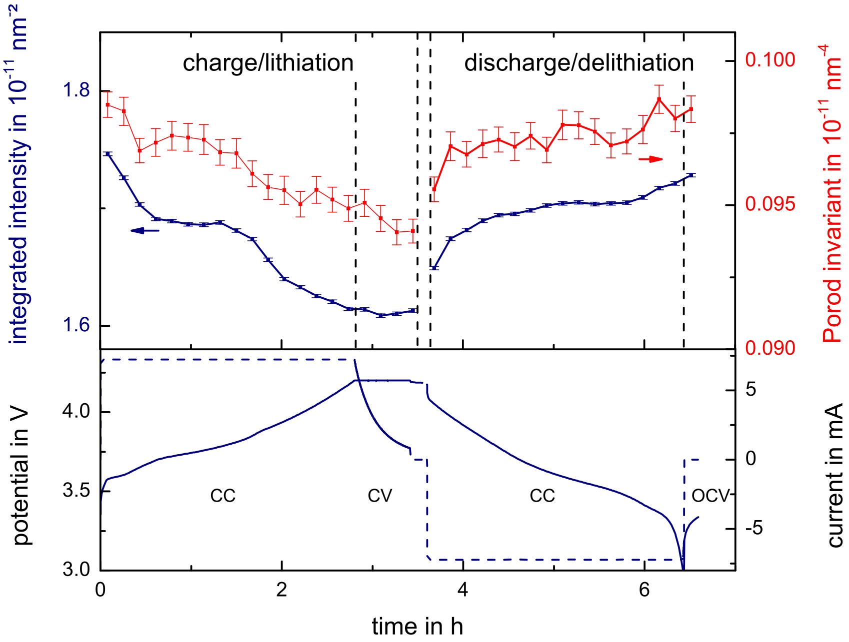

Figure 5.30.: C/NMC-111 full cell (cell ID nov1) integrated intensity Γ and Porod invariant versus time upon charging and discharging. SANS data scaled to 1 mm H_2O. Limiting areal capacity (NMC) of 2.53 mAh/cm^2, LP57 electrolyte. Charge up to 4.2 V (CCCV), discharge down to 3 V (CC).

The total change in integrated intensity during lithiation (always understood as lithiation of graphite in the following) is ca. -8%. We compare this to the theoretical value calculated from equation 5.57. From the experiments in section 5.3.2 we know that all inactive materials contribute 23%, the whole cathode 50% and the anode 27%. Both electrodes contain small amounts of binder which gives low contrast and is neglected.

In the cathode there are however also 2 wt.% of carbon black additive C65 which has a high contrast and a high surface area (62 m^2/g from spec sheet) and is therefore relevant for SANS contrast. Because the coherence length is of the order of 200 nm, the small carbon black particles give a significant scattering contribution. Comparing the surface area contribution per gram of coating, we have surfaces of $0.96 \cdot 0.25 \cdot 10^4\,\mathrm{cm}^2 = 0.24 \cdot 10^4\,\mathrm{cm}^2$ for NMC to $0.02 \cdot 62 \cdot 10^4\,\mathrm{cm}^2 = 1.24 \cdot 10^4\,\mathrm{cm}^2$ for carbon black. Multiplying with the respective $\Delta\rho^2$ factor from table 5.3, we get the intensity contributions. Per gram coating, for NMC we get $0.24 \cdot 10^4\,\mathrm{cm}^2 \cdot 6.5 \cdot 10^{20}\,\mathrm{cm}^{-4} = 1.56 \cdot 10^{24}\,\mathrm{cm}^{-2}$, and for the carbon black contribution we get $1.24 \cdot 10^4\,\mathrm{cm}^2 \cdot 40 \cdot 10^{20}\,\mathrm{cm}^{-4} = 49.6 \cdot 10^{24}\,\mathrm{cm}^{-2}$. Reducing the carbon black contribution arbitrarily by a factor of 5 in order to account for clustered particles, carbon NMC contribution to carbon black contribution has a ratio of 1.6 to 10. Taking into account, that the cathode has only 50% share in the total cell integrated intensity from above, we arrive at only 7% intensity contribution of NMC and 43% of carbon black.

Now, we have all parts to calculate the missing geometry factors c_2, as we did before for the half cell, e. g. for graphite we calculate $27\% \cdot 1.75 \cdot 10^{-11}\,\mathrm{nm}^{-2}/40 \cdot 10^{20}\,\mathrm{cm}^{-4} = 0.012 \cdot 10^{-11}\,\mathrm{nm}^{-2}/10^{20}\,\mathrm{cm}^{-4}$, in the delithiated state, where the total integrated intensity value is known. Here, the full cell value measured for the cycled full cell nov1 was used which is different from the cell measured in 5.17 (differing q-range setup and measurement time). Again, we can vary $\Delta\rho^2$ to get the theoretical value after lithiation. The integrated intensity is given by (in units of $10^{-11}\,\mathrm{nm}^{-2}$):

$$\begin{aligned}
&\Gamma_{\text{total}}\\
&= \underbrace{c_0'}_{\text{inactive}\,\equiv 23\%} + \underbrace{c_0'}_{\text{carbon black}\,\equiv 43\%} + \underbrace{c_2 \Delta\rho^2{}_{\text{NMC/electrol}}}_{\equiv 7\%} + \underbrace{c_2 \Delta\rho^2{}_{\text{graphite/electrol}}}_{\equiv 27\%}\\
&= \underbrace{0.4}_{\text{inactive}} + \underbrace{0.76}_{\text{carbon black}} + \underbrace{0.018\,\Delta\rho^2{}_{\text{NMC/electrol}}}_{\Delta\rho^2 = 6.5\text{ to }8.0} + \underbrace{0.012\,\Delta\rho^2{}_{\text{graphite/electrol}}}_{\Delta\rho^2 = 40\text{ to }26.2}\\
&= 1.75\,(\text{dch})\ \text{to}\,1.62\,(\text{ch})\,.
\end{aligned} \tag{5.61}$$

Here, we have charged the cell and varied the NMC utilization from $x = 1$ to 0.5 (x in $\mathrm{Li_xNi_{0.33}Mn_{0.33}Co_{0.33}O_2}$) and graphite utilization from $x = 0$ to 1 (x in $\mathrm{Li_xC_6}$). The integrated intensity change from 1.75 to 1.62 is a net decrease of 7.7%, very close to the experimentally observed decrease of 8%. At intermediate lithiation during charging, for $x = 0.72$ in $\mathrm{Li_xNMC}$ and $x = 0.5$ (in $\mathrm{V_{shell}}$) in $\mathrm{Li_xC_6}$, the calculated relative integrated intensity change is -4.2% which also agrees fairly well with experimental data of ca. -6%, as seen in figure 5.31 for the first cycle from $x = 0$ to $x = 0.5$. Of course, the theoretical estimation is approximate and confirms only the order of magnitude, but still we are able to get to this figure by simple plausible assumptions which are justified by known parameters of the samples.

Varying C-rate

In another measurement campaign, a second full cell with ID z5 was measured with varying C-rates. Figure 5.32 shows all data of the two full cells for charge/lithiation of graphite. Relative integrated intensity data points are plotted with error bars and a Savitzky-Golay fit line. Both cells are balanced full cells with standard loadings of $3\,\mathrm{mAh/cm^2}$ (cell ID nov1) and $1\,\mathrm{mAh/cm^2}$ (cell ID z5). For the rate

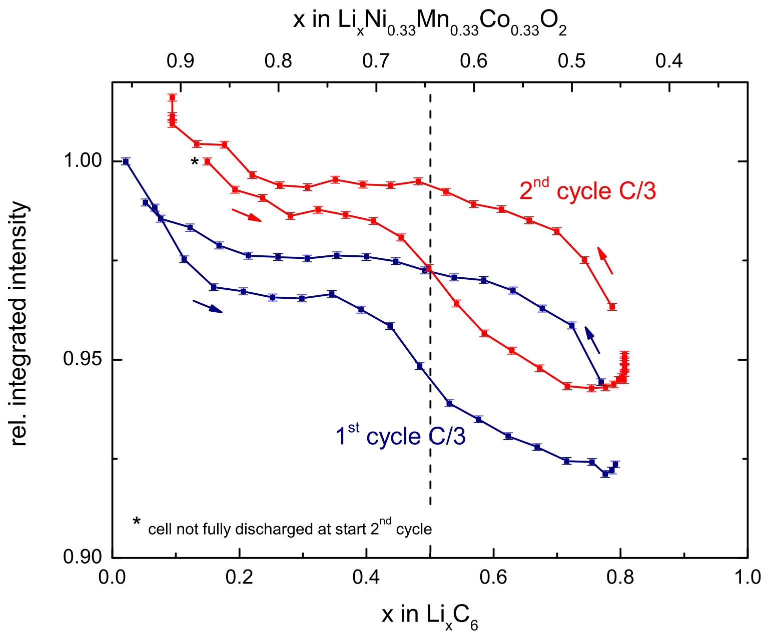

Figure 5.31.: C/NMC-111 full cell (cell ID nov1) relative integrated intensity $\Gamma_x/\Gamma_{x=0}$ upon charging and discharging for first and second cycle at a rate of C/3 (measured after 3 month break). Charge up to 4.2 V (CCCV), discharge down to 3 V (CC).

C/3, the curves look very similar and show the same decrease and feature the same plateaus. The slightly faster rate C/2 results in a shift of the curve to higher utilization x in Li$_x$C$_6$. Note that another discharging experiment was done before this cycle as seen in figure B.4.

Lithiation model

At C/3, the beginning of the first plateau (point 1) is at ca. 20% of SoC and holds until around 40%. Again, we assume that point 1 marks the state where the interior of the particle is lithiated to Li$_{x<0.5}$C$_6$ and the coherence shell is just completely lithiated to LiC$_{12}$, so this is at SoC $\leq 1/3 + (1/2 - 1/3) \cdot C_{\text{rel,shell}}$. Calculating with an assumed 6% share of the shell (referring to LiC$_6$) we arrive at 34% SoC for point 1 which is higher than the 20% measured. One explanation for the deviation could be that the interior of the particle is less lithiated than the assumed phase LiC$_{18}$ (yielding 1/3) here. Point 2 is where the contrast changes again as the outer shell is lithiated further to LiC$_6$ which must definitely happen before SoC $= 1/2$ for a homogeneous lithiation, in good agreement with our data. Finally, point 3 indicates where the coherence shell is completely filled by LiC$_6$, at

SoC $\leq 1/2 + 1/2 \cdot C_{\mathrm{rel,shell}}$ which is ca. 53% with the assumed 6% shell. The second plateau is not as flat as the first in the experimental data, but we see a decline in slope at values of 55 to 65% for C/3. As in the half cell, a bigger coherence shell volume would shift the plateau positions to higher capacities. Inhomogeneity in lithiation shifts them to lower capacities.

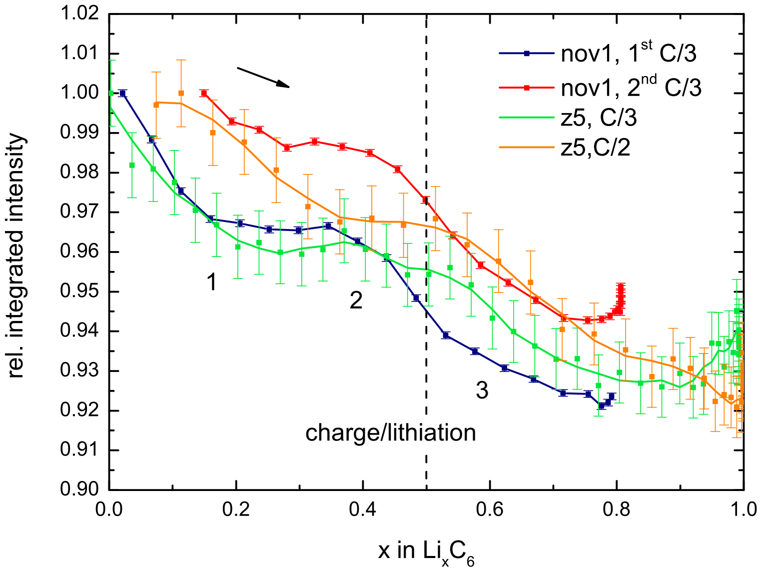

Figure 5.32.: Relative integrated intensity $\Gamma/\Gamma_{\mathrm{max}}$ vs. capacity for two C/NMC-111 full cells during charging. Each curve normalized to maximum value. Cell ID nov1 and z5 with limiting areal capacities (NMC) of 2.53 mAh/cm^2 resp. 0.88 mAh/cm^2, LP57 electrolyte. Charge up to 4.2 V resp. 4.4 V (CCCV), discharge down to 3 V (CC resp. CCCV).

Delithiation model

Data points of the subsequent discharge/delithiation are shown in figure 5.33. The value of integrated intensity rises again to near 1 at 0% SoC for all measurements. The shape of the curve is similar to the half cell results, but now with a more prominent plateau. From the start at highest reached SoC, the integrated intensity rises fast to a plateau from ca. 70 to 80% SoC to around 30 to 25% SoC. From theory, we would expect the delithiation from outside to inside to yield a contrast change right from the beginning until the coherence shell is delithiated to a lower phase, e. g. LiC_{12}. For the 6% shell this point 1' is at SoC $= 1 - 1/2 \cdot C_{\mathrm{rel,shell}}$ which is 97%. The steep beginning (except for cell z5 at SoC $>$ 90%) correlates well with theory, even though the range of increase is broader, probably again

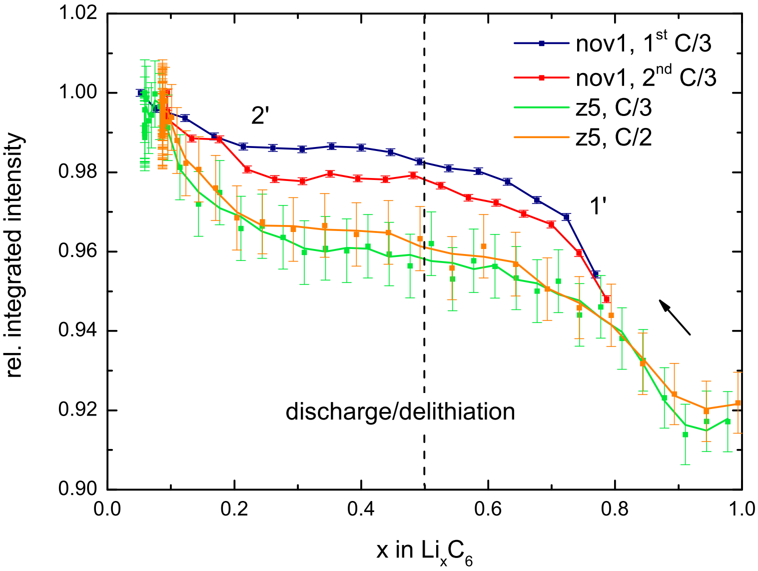

Figure 5.33.: Relative integrated intensity $\Gamma/\Gamma_{\text{max}}$ vs. capacity for two C/NMC-111 full cells during discharging. Each curve normalized to maximum value. Cell ID nov1 and z5 with limiting areal capacities (NMC) of 2.53 mAh/cm^2 resp. 0.88 mAh/cm^2, LP57 electrolyte. Charge up to 4.2 V resp. 4.4 V (CCCV), discharge down to 3 V (CC resp. CCCV).

caused by inhomogeneities and distribution effects in the real system. The end of the plateau is expected at SoC = 1/2 where lower lithiated phases $\text{Li}_{x<0.5}\text{C}_6$ are beginning to form at the surface of the particle. Experimentally we observe a small step around 50% SoC but another plateau extends until around 20% SoC. A possible reason could be that the clear phase separation is not happening and that the outer shell volume is slightly delithiated further between point 1' and 2' leading to a continuous increase in integrated intensity signal and no clear plateau ending except when even lower lithiated phases are reached in the end.

Stepwise charging

To investigate the effect of time on the observed change in integrated intensity as a function of exchanged charge, the full cell z5 was charged at C/3 with two interruptions during which the cell was observed under OCV conditions. Data points of relative integrated intensity and the correlating capacity are plotted vs. time in figure 5.34. These results show that the integrated intensity signal stays constant (within the error bars) during the break and confirm the capacity dependence of Γ.

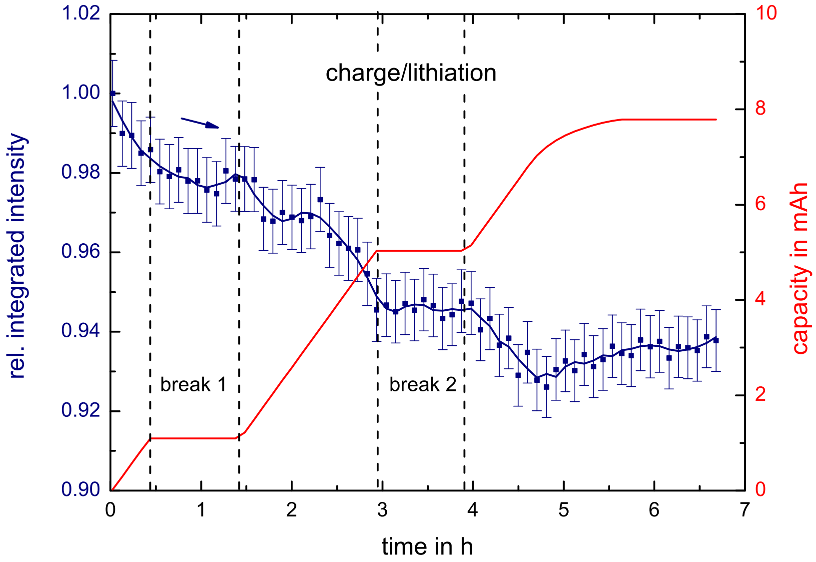

Figure 5.34.: Relative integrated intensity $\Gamma/\Gamma_{\max}$ vs. time for a C/NMC-111 full cell (cell ID z5). Charging at C/3 up to 4.4 V with two OCV breaks and a CV phase at the end. Limiting areal capacity (NMC) of 0.88 mAh/cm^2, LP57 electrolyte.

Plotted vs. capacity or utilization in figure 5.35, the curve looks similar to the other integrated intensity curves during charge. The upper x-axis shows the utilization of NMC in this balanced cell. NMC utilization x in $\mathrm{Li_xNi_{0.33}Mn_{0.33}Co_{0.33}O_2}$ is calculated by setting the transferred charge in relation to the weighted active material mass and is corrected for initial irreversible capacity loss. NMC utilization varies from $\mathrm{Li_{x\approx1}Ni_{0.33}Mn_{0.33}Co_{0.33}O_2}$ to $\mathrm{Li_{x\approx0.5}Ni_{0.33}Mn_{0.33}Co_{0.33}O_2}$ as expected for a balanced cell within the typical voltage range of 3 to 4.4 V. In conclusion, the interruptions have no significant effect on the overall integrated intensity curve and the signal stays constant over the two OCV periods (within the error bars).

Varying anode overbalancing

In order to study the effect of balancing and the influence of the NMC cathode, a third cell was prepared and measured. In this “overbalanced” cell (ID z8) the anode was largely oversized by a factor of 5. Because the Li brought in from the cathode is limiting, this means that the graphite material is largely unused. Graphite is only utilized to around 20%, whereas NMC-111 is utilized normally from $x \approx 1$ to $x \approx 0.5$. Both cells, the normally balanced and the overbalanced cell are shown in figure 5.36 vs. charge transfer plotted as graphite utilization. NMC utilization is also plotted for both as upper x-axis. For the overbalanced cell the integrated intensity

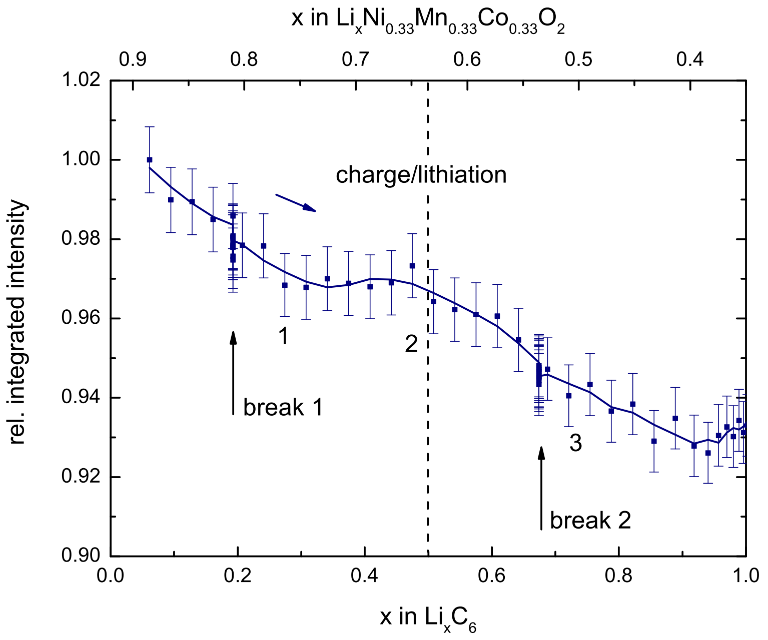

Figure 5.35.: Relative integrated intensity $\Gamma/\Gamma_{\max}$ vs. capacity for a C/NMC-111 full cell (cell ID z5). Charging at C/3 up to 4.4 V with two OCV breaks and a CV phase at the end. The two OCV breaks (all data points from one break are plotted on the same respective x value here) do not alter the trend and confirm the correlation of Γ to capacity. Limiting areal capacity (NMC) of 0.88 mAh/cm^2, LP57 electrolyte. The same break and point positions as in figure 5.34 are indicated.

decreases by 7% during charging and rises back during discharging. The fact that the signal decreases faster than for the normally balanced cell can be understood by the fact that graphite dominates the incoherent sum of the total sample. There is no significant step or plateau feature outside the error bar corridor. This is in accordance with the model that until point 1 at ≈ 33% no distinct phase has formed within the coherence shell which could lead to abrupt contrast differences.

Full cell picture

Figure 5.37 collects all full cell curves for charge and shows the comparison to the lithiation front hypothesis. As for the half cell there are two states. State (a) where a phase is formed in the outer coherence shell of the particle and contrast changes are visible and state (b) where phase formation happens in the inside of the particle and no contrast change is visible from the outside and in the SANS signal.

For discharge, figure 5.38 collects all full cell curves and shows the comparison

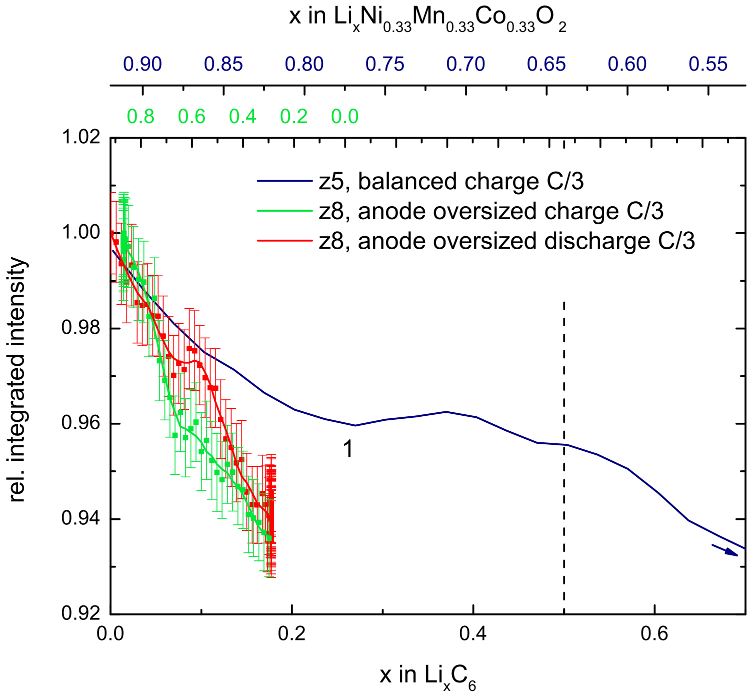

Figure 5.36.: Relative integrated intensity $\Gamma/\Gamma_{\mathrm{max}}$ vs. capacity for normally balanced (cell ID z5) and overbalanced (cell ID z8) C/NMC-111 full cell. Limiting areal capacity at the NMC cathode of 0.88 and 0.86 mAh/cm^2 versus 0.88 resp. 5 mAh/cm^2 at the graphite anode.

to the delithiation front hypothesis. The curves are sligthly shifted due to the different achieved real capacities. Starting from the right, there is a first sharp rise in integrated intensity that is associated to delithiation of the outer shell (a). Subsequent phase transformation in the interior of the particle (b) is invisible to SANS. The continuous transformation to lower lithiated phases leads to a steady increase in intensity. In summary, the findings are similar to the half cell results.

Additional parameters and the SANS signal

Particle size and distribution

Until now, we have assumed that the graphite particles are spherical. However, in reality the shape is more like a potato. This means that the surface area is larger and also that the volume share of the coherence shell could be larger. Thus, the transition region where the SANS integrated intensity changes might be larger: during lithiation point 1 and 3 of figure 5.37 are shifted to the right and during delithiation point 1’ of figure 5.38 is shifted to the left (analogously in the half cell

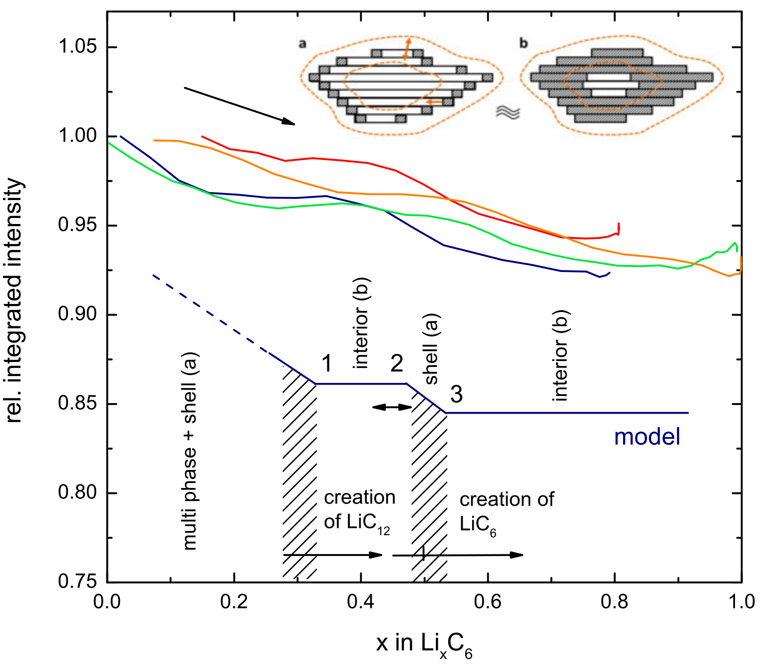

Figure 5.37.: Relative integrated intensity of all full cells during charging in comparison with model curve. Two states can be distinguished: a) a phase is formed in the outer coherence shell of the particle and contrast changes are visible, b) phase formation happens in the inside of the particle and no contrast change is visible from the outside and in the SANS signal.

figures). This is an explanation why the observed width of the transition region is larger than expected from the coherence shell volume which is only a few percent of the total volume.

A second aspect which we have neglected so far is the size distribution of the particles. The mean diameter (as derived from the volume based distribution) times the number of particles in the volume gives the correct amount of active material in the sample. But the spherical surface derived from this diameter does not yield the average surface (even if we would have perfectly spherical particles) due to the size distribution. This is because the volume scales with R^3 but the surface scales approximately with R^2. Also the surface shell of 200 nm scales with the surface, so the estimation that the surface shell makes up 6% of the total volume is only approximate. Here, the mean diameter based on volume is 22 µm whereas the mean diameter based on surface is only 18 µm. Hence the maximum error in the share of the shell $C_{\text{rel,shell}}$ is for sure less than 20%. In this uncertainty, we may include some variance of the shell volume due to coherence volume asymmetry as

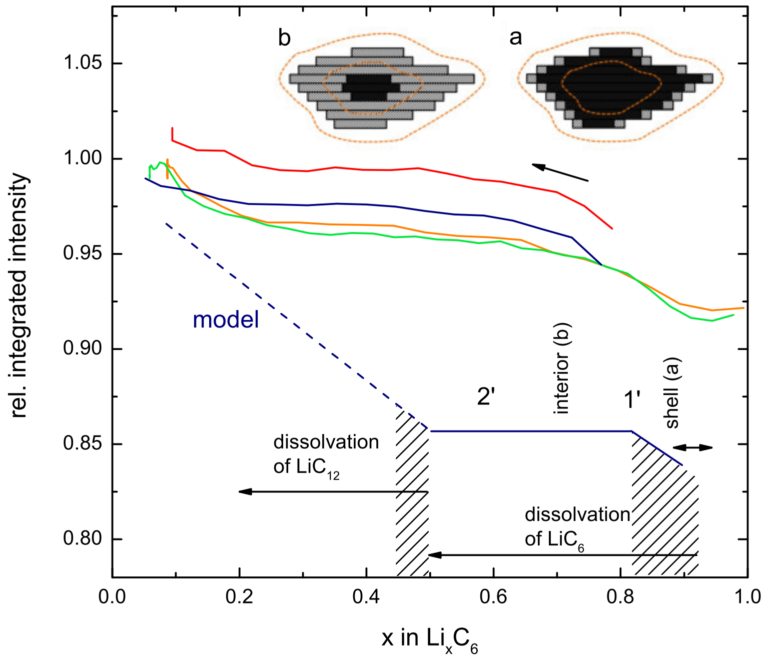

Figure 5.38.: Relative integrated intensity of all full cells during discharging in comparison with model curve. During delithiation of the outer shell (a) integrated intensity changes. Phase transformation in the interior of the particle (b) is invisible to SANS.

well.
Third, the volume change of graphite to LiC$_6$ alone could influence the SANS signal because the surface of all particles and thus V_{shell} increases. However, since the particle density N_P/V decreases at the same time, for small volume change the effect is compensated and can be neglected. Also, the surface and thus integrated intensity would increase with lithiation whereas the opposite is observed in experiment.

Crystallinity and pores

Micrometer-sized synthetic graphite particles are not consisting of one crystal but are formed of crystalline domains that are characterized by a crystalline length. Typical crystal length for synthetic graphite is 30 to 300 nm [90, 160], for the graphite SLP30 by Timcal/Imerys which is comparable to our graphite a value of 200 nm is given in the spec sheet [161]. For flake-like graphite the crystallinity is of course much larger in the basal direction. The propagation of phase transformation inside the particle might be influenced by the crystal boundaries and so would the lithiation behavior on the nanoscale. But for lithiation behavior on the larger scale, the graphite particle is still treated as if it was an homogeneous particle by many authors, e. g. Heß et al. [90]. However, some authors claim complicated lithiation behavior in multi-domain mesocarbon microbeads (MCMB) [162]. In SEM images (figure 3.1), the graphite surface looks rather flat and the basal planes are smooth. But some pores might be present, in particular at the edge planes as shown by Plack et al. [163]. Gulbrekken finds that for SLP30 about one third of the total BET surface area (2 out of $6\,\mathrm{m}^2$) is present in mesopores of 10 nm and more. The graphite used in this study has a BET area of $4\pm0.2\,\mathrm{m}^2$ and we would expect similar pore fractions. The effect of pores in the SANS experiment is that the coherence shell volume is enlarged thus broadening the transition zones, as it is indeed observed in the experiment.

Polarization and homogeneity across electrode

In all the derivations above, we have assumed that all particles in the electrode are at the same potential and undergo de/lithiation simultaneously. A first hint that this assumption is valid for the chosen C-rates here is that the XRD data clearly shows the subsequent and distinguishable phases. Another estimator was introduced by Doyle et al. [40, 90]: the dimensionless figure S_{el} compares the diffusion in the electrolyte in the porous separator and electrode to the amount of Li-ions or charge transferred.

$$S_{\mathrm{el}} = (t_{\mathrm{sep}} + t_{\mathrm{e}})^2 \frac{I}{D_{\mathrm{el}} F (1-\epsilon) c_{\mathrm{solid}} t_{\mathrm{e}}}\,, \tag{5.62}$$

with typically $t_{\mathrm{sep}} = 20\,\mu\mathrm{m}, t_{\mathrm{e}} = 80\,\mu\mathrm{m}$ being the thickness of separator and electrode, F the Faraday constant, $\epsilon = 0.5$ the electrode porosity and $c_{\mathrm{solid}} = 34175\,\mathrm{mol/m}^3$ the maximum concentration of Li in the solid graphite. The diffusion constant in the electrolyte D_{el} is estimated from the measured conductivity $\kappa = 10\,\mathrm{mS/cm}$ at 25°C for 1 M LiPF$_6$ in EC:EMC 3:7 as shown in section 4.1.4 to $D_{\mathrm{el}} \approx 2.6 \cdot 10^{-6}\,\mathrm{cm}^2/\mathrm{s}$. Inserting a typical current density at low C-rates of $I = 1\,\mathrm{mA/cm}^2$, we get $S_{\mathrm{el}} = 0.003$ which is much less than 1. Polarization in the electrolyte across the electrode is thus not a problem at the chosen C-rates.

Phase stability over time and redistribution

One could argue that there is some kind of redistribution and that local difference in SoC across the particle will compensate over time while of course conserving the global charge or Li concentration in the system, i. e. global phase ratios are not affected. On the time scale of a few hours of cycling (and less for relaxation periods) here, no redistribution is however expected and we assume a stable core-shell separation. Harris et al. show that phase separation is stable for hours across electrodes as well as across a single particle [103, 162]. Phase redistribution after plating has been shown to happen on a timescale of 20 h by Zinth et al. [97] which gives an estimate for the speed of other redistributive processes. Also in the model by Bohn et al. stages are stable and the lithiation fronts propagate slowly into the particle with a defined boundary at a C-rate of 0.7 C [111].

Li plating

At high C-rates Li plating can occur when either charge transfer resistance or solid diffusion limitations force the potential to 0 V. Li plating would probably not show up in the integrated intensity signal because the Li signal is smaller and the amount will also be only a few percent of capacity in typical plating situations. The plateau at the beginning of discharge for the full cell z5 could be explained by plated Li that is discharged before the Li from the outer graphite shell is taken out. The diffusion constant D of Li in the graphite helps to estimate whether diffusion is limiting. From Park et al. [58] we take the estimate of $D_{\mathrm{Li,solid}} = 10^{-14}\,\mathrm{m}^2/\mathrm{s}$. Equilibrium is then reached after the characteristic time constant $\tau = x^2/D$, which is of the order of 100 s for a typical particle dimension of 1 µm. For the experiments at low C-rates which take hours this is not limiting.

5.3.5. Conclusion

In conclusion, we have shown first results for the operando measurement of Li-ion pouch cell batteries in a SANS experiment. The system is very complex and the variety and the length scale of materials present in the beam makes it hard to use classical SANS modeling techniques. However, we have demonstrated, that still the difference in SLD from the materials contributes via $\Delta\rho^2$ to the observed differences in SANS signal, best represented by the integrated intensity. By comparison to other background contributions and by half cell and unbalanced cell measurements we have shown that indeed graphite is contributing significantly to the change in SANS signal. The plateau-like features of the integrated intensity curve can finally be explained by the staged and directional lithiation of graphite seen in the SANS experiment with the local resolution feature which is introduced by the locally sampling coherence volume.

6. Summary

In summary, we have presented two aspects of rate limitation in lithium-ion batteries. First, the slow transport in the electrolyte can hinder the charge or discharge which scales heavily with electrode thickness as shown by experimental data here. As discussed, limitations buildup over time via electrolyte polarization and simple ohmic drop methods fail to predict real battery performance under load. The actual high rate performance can only be determined by appropriate electrochemical models which implement the transport processes, e. g. following the work of Newman. A paramount input parameter to these models, the tortuosity, was determined here with a reliable and simple method. Again, the Bruggeman assumption could not be confirmed. The hope is that better input parameters for all kinds of battery electrodes and separators will help to improve simulations in the future. Here, the focus was on rate performance measurements during full cell discharge, but of course charging performance is important too. The avoidance of Li plating during charging is paramount both for lifetime and for safety. Fast charging especially at low temperatures will probably be a major bottleneck for future electric cars and charging performance needs to be studied further in upcoming research. Second, a detailed SANS study was presented here, comprising theory as well as experiments on component and system level. We could show that the change in SANS signal can be explained well by the lithiation of graphite and the propagation of dedicated fronts in the active particles. Also the numbers fit quite well to the theoretically expected change. Thus, SANS has been established as a novel method to study the transport processes in lithium-ion batteries. Though limited in availability and complex in data reduction, SANS is a valuable tool for understanding the lithiation of active materials giving averaged but local information from a whole sample volume. Together with tomographic imaging techniques this could enhance the understanding of current and future battery materials like silicon where expansion during lithiation still leaves many open questions.

Bibliography

[1] L. Galvani, G. Aldini, *De viribus electricitatis*, Apud Societatem Typographicam, **1792**.

[2] A. Volta, J. Banks, *The Philosophical Magazine* **1800**, *7*, 289–311.

[3] R. Korthauer, *Handbuch Lithium-Ionen-Batterien*, Springer, Berlin Heidelberg, **2013**.

[4] The Economist (Jan. 16th), The battery era: A plug for the battery, Newspaper Article, **2016**.

[5] IEA, Global EV Outlook 2016, Report, International Energy Agency, **2016**.

[6] O. Gröger, H. A. Gasteiger, J.-P. Suchsland, *Journal of the Electrochemical Society* **2015**, *162*, A2605–A2622.

[7] M. Anderman, xEV Industry Report, Report, Total Battery Consulting Inc., **2016**.

[8] B. Nykvist, M. Nilsson, *Nature Climate Change* **2015**, *5*, 329–332.

[9] K. G. Gallagher, S. Goebel, T. Greszler, M. Mathias, W. Oelerich, D. Eroglu, V. Srinivasan, *Energy & Environmental Science* **2014**, *7*, 1555.

[10] D. Larcher, J. M. Tarascon, *Nature Chemistry* **2015**, *7*, 19–29.

[11] FraunhoferISI, Gesamt-Roadmap Lithium-Ionen Batterien 2030, Report, Fraunhofer-Institut für System- und Innovationsforschung, **2015**.

[12] D. Aurbach, *Journal of the Electrochemical Society* **2015**, *162*, A2379–A2379.

[13] E. J. Berg, C. Villevieille, D. Streich, S. Trabesinger, P. Novák, *Journal of the Electrochemical Society* **2015**, *162*, A2468–A2475.

[14] D. Andre, S.-J. Kim, P. Lamp, S. F. Lux, F. Maglia, O. Paschos, B. Stiaszny, *Journal of Materials Chemistry A* **2015**, *3*, 6709–6732.

[15] K. Takada, N. Ohta, Y. Tateyama, *Journal of Inorganic and Organometallic Polymers and Materials* **2015**, *25*, 205–213.

[16] S. Seidlmayer, J. Hattendorff, I. Buchberger, L. Karge, H. A. Gasteiger, R. Gilles, *Journal of the Electrochemical Society* **2015**, *162*, A3116–A3125.

[17] D. Linden, T. B. Reddy in *Linden's Handbook of Batteries*, (Eds.: T. B. Reddy, D. Linden), McGraw Hill, New York, **2011**, Chapter 1.

[18] A. J. Bard, L. R. Faulkner, *Electrochemical Methods: Fundamentals and Applications*, 2nd, Wiley, New York, **2001**.

[19] M. Winter, R. Brodd, *Chemical Reviews* **2004**, *104*, 4245–4269.

[20] N. Nitta, F. Wu, J. T. Lee, G. Yushin, *Materials Today* **2015**, *18*, 252–264.

[21] W. Dreyer, J. Jamnik, C. Guhlke, R. Huth, J. Moškon, M. Gaberšček, *Nature materials* **2010**, *9*, 448–453.

[22] M. Salomon in *Linden's Handbook of Batteries*, (Eds.: T. B. Reddy, D. Linden), McGraw Hill, New York, **2011**, Chapter 2.

[23] K. Xu, *Chemical Reviews* **2004**, *104*, 4303–4418.

[24] V. Etacheri, O. Haik, Y. Goffer, G. A. Roberts, I. C. Stefan, R. Fasching, D. Aurbach, *Langmuir* **2012**, *28*, 965–976.

[25] K. Xu, *Chemical Reviews* **2014**, *114*, 11503–11618.

[26] P. Arora, R. E. White, *Journal of the Electrochemical Society* **1998**, *145*, 3647–3667.

[27] M. Broussely, P. Biensan, F. Bonhomme, P. Blanchard, S. Herreyre, K. Nechev, R. J. Staniewicz, *Journal of Power Sources* **2005**, *146*, 90–96.

[28] T. Marks, S. Trussler, A. J. Smith, D. Xiong, J. R. Dahn, *Journal of the Electrochemical Society* **2011**, *158*, A51–A57.

[29] P. Arora, Z. Zhang, *Chemical Reviews* **2004**, *104*, 4419–4462.

[30] M. E. Orazem, B. Tribollet, *Electrochemical Impedance Spectroscopy*, Wiley, Hoboken, New Jersey, **2008**.

[31] V. F. Lvovich, *Impedance Spectroscopy, Applications to Electrochemical and Dielectric Phenomena*, Wiley, Hoboken, New Jersey, **2012**.

[32] J. Illig, M. Ender, A. Weber, E. Ivers-Tiffée, *Journal of Power Sources* **2015**, *282*, 335–347.

[33] S.-M. Park, J.-S. Yoo, *Analytical Chemistry* **2003**, 455 A.

[34] M. Ender, A. Weber, E. Ivers-Tiffée, *Journal of the Electrochemical Society* **2012**, *159*, A128.

[35] K. K. Patel, J. M. Paulsen, J. Desilvestro, *Journal of Power Sources* **2003**, *122*, 144–152.

[36] I. V. Thorat, D. E. Stephenson, N. A. Zacharias, K. Zaghib, J. N. Harb, D. R. Wheeler, *Journal of Power Sources* **2009**, *188*, 592–600.

[37] B. Tjaden, S. J. Cooper, D. J. L. Brett, D. Kramer, P. R. Shearing, *Current Opinion in Chemical Engineering* **2016**, *12*, 44–51.

[38] D. A. G. Bruggeman, *Annalen der Physik* **1935**, *416*, 636–664.

[39] J. Newman, K. E. Thomas-Alyea, *Electrochemical systems*, John Wiley & Sons, **2012**.

[40] M. Doyle, T. F. Fuller, J. Newman, *Journal of the Electrochemical Society* **1993**, *140*, 1526–1533.

[41] C.-H. Kim, S.-I. Pyun, J.-H. Kim, *Electrochimica Acta* **2003**, *48*, 3455–3463.

[42] J.-B. Jorcin, M. E. Orazem, N. Pébère, B. Tribollet, *Electrochimica Acta* **2006**, *51*, 1473–1479.

[43] M. Gaberscek, J. Moskon, B. Erjavec, R. Dominko, J. Jamnik, *Electrochemical and Solid-State Letters* **2008**, *11*, A170.

[44] J. E. B. Randles, *Discussions of the Faraday Society* **1947**, *1*, 11–19.

[45] M. Ender, A. Weber, E. Ivers-Tiffée, *Electrochemistry Communications* **2013**, *34*, 130–133.

[46] M. Eikerling, A. A. Kornyshev, *Journal of Electroanalytical Chemistry* **1999**, *475*, 107–123.

[47] Y. Liu, M. W. Murphy, D. R. Baker, W. Gu, C. Ji, J. Jorne, H. A. Gasteiger, *Journal of the Electrochemical Society* **2009**, *156*, B970.

[48] N. Ogihara, S. Kawauchi, C. Okuda, Y. Itou, Y. Takeuchi, Y. Ukyo, *Journal of the Electrochemical Society* **2012**, *159*, A1034–A1039.

[49] N. Ogihara, Y. Itou, T. Sasaki, Y. Takeuchi, *The Journal of Physical Chemistry C* **2015**, *119*, 4612–4619.

[50] R. De Levie, *Electrochimica Acta* **1963**, *8*, 751–780.

[51] J. Illig, *Physically based Impedance Modelling of Lithium-Ion Cells (PhD thesis)*, *Vol. 27*, KIT Scientific Publishing, **2014**.

[52] H. Wang, M. Yoshio, *Journal of Power Sources* **2012**, *200*, 108–112.

[53] D. Aurbach, *Nonaqueous Electrochemistry*, Taylor & Francis, **1999**.

[54] J. Landesfeind, J. Hattendorff, A. Ehrl, W. A. Wall, H. A. Gasteiger, *Journal of the Electrochemical Society* **2016**, *163*, A1373–A1387.

[55] T. F. Fuller, M. Doyle, J. Newman, *Journal of the Electrochemical Society* **1994**, *141*, 1–10.

[56] K. M. Abraham, *Electrochimica Acta* **1993**, *38*, 1233–1248.

[57] D. Djian, F. Alloin, S. Martinet, H. Lignier, J. Y. Sanchez, *Journal of Power Sources* **2007**, *172*, 416–421.

[58] M. Park, X. Zhang, M. Chung, G. B. Less, A. M. Sastry, *Journal of Power Sources* **2010**, *195*, 7904–7929.

[59] W. Lu, A. Jansen, D. Dees, P. Nelson, N. R. Veselka, G. Henriksen, *Journal of Power Sources* **2011**, *196*, 1537–1540.

[60] H. Zheng, J. Li, X. Song, G. Liu, V. S. Battaglia, *Electrochimica Acta* **2012**, *71*, 258–265.

[61] H. Y. Tran, C. Täubert, M. Wohlfahrt-Mehrens, *Progress in Solid State Chemistry* **2014**, *42*, 118–127.

[62] M. Singh, J. Kaiser, H. Hahn, *Journal of the Electrochemical Society* **2015**, *162*, A1196–A1201.

[63] S. R. Sivakkumar, J. Y. Nerkar, A. G. Pandolfo, *Electrochimica Acta* **2010**, *55*, 3330–3335.

[64] K. G. Gallagher, S. E. Trask, C. Bauer, T. Woehrle, S. F. Lux, M. Tschech, P. Lamp, B. J. Polzin, S. Ha, B. Long, Q. Wu, W. Lu, D. W. Dees, A. N. Jansen, *Journal of the Electrochemical Society* **2016**, *163*, A138–A149.

[65] H. Zheng, G. Liu, X. Song, P. Ridgway, S. Xun, V. S. Battaglia, *Journal of the Electrochemical Society* **2010**, *157*, A1060.

[66] P. Arora, M. Doyle, A. S. Gozdz, R. E. White, J. Newman, *Journal of Power Sources* **2000**, *88*, 219–231.

[67] M. Wang, J. Li, X. He, H. Wu, C. Wan, *Journal of Power Sources* **2012**, *207*, 127–133.

[68] V. P. Nemani, S. J. Harris, K. C. Smith, *Journal of the Electrochemical Society* **2015**, *162*, A1415–A1423.

[69] H. Han, H. Park, K. C. Kil, Y. Jeon, Y. Ko, C. Lee, M. Kim, C.-W. Cho, K. Kim, U. Paik, T. Song, *Electrochimica Acta* **2015**, *166*, 367–371.

[70] N. A. Zacharias, D. R. Nevers, C. Skelton, K. Knackstedt, D. E. Stephenson, D. R. Wheeler, *Journal of the Electrochemical Society* **2012**, *160*, A306–A311.

[71] L. Holzer, D. Wiedenmann, B. Münch, L. Keller, M. Prestat, P. Gasser, I. Robertson, B. Grobéty, *Journal of Materials Science* **2013**, *48*, 2934–2952.

[72] T. DuBeshter, P. K. Sinha, A. Sakars, G. W. Fly, J. Jorne, *Journal of the Electrochemical Society* **2014**, *161*, A599–A605.

[73] M. Ender, J. Joos, T. Carraro, E. Ivers-Tiffée, *Electrochemistry Communications* **2011**, *13*, 166–168.

[74] M. Ebner, F. Geldmacher, F. Marone, M. Stampanoni, V. Wood, *Advanced Energy Materials* **2013**, *3*, 845, Supporting Information.

[75] S. J. Harris, P. Lu, *The Journal of Physical Chemistry C* **2013**, *117*, 6481–6492.

[76] M. Ebner, D.-W. Chung, R. E. García, V. Wood, *Advanced Energy Materials* **2014**, *4*, 1–6.

[77] L. Zielke, T. Hutzenlaub, D. R. Wheeler, I. Manke, T. Arlt, N. Paust, R. Zengerle, S. Thiele, *Advanced Energy Materials* **2014**, *4*, 1301617.

[78] F. Tariq, V. Yufit, M. Kishimoto, P. R. Shearing, S. Menkin, D. Golodnitsky, J. Gelb, E. Peled, N. P. Brandon, *Journal of Power Sources* **2014**, *248*, 1014–1020.

[79] M. Ebner, V. Wood, *Journal of the Electrochemical Society* **2015**, *162*, A3064–A3070.

[80] D. Cericola, M. E. Spahr, *Electrochimica Acta* **2016**, *191*, 558–566.

[81] J. Hattendorff, J. Landesfeind, A. Ehrl, W. A. Wall, H. A. Gasteiger, *ECS Transactions* **2015**, *69*, 135–140.

[82] M. J. Hantel, M. M. Armstrong, F. DaRosa, R. l'Abee, *Journal of the Electrochemical Society* **2017**, *166*, A334–A339.

[83] W. Peukert, *Elektrotechnische Zeitschrift* **1897**, *20*, 20–21.

[84] D. Hwang, H. Zabel, G. Kirczenow, S. Solin, P. Lagrange, A. Magerl, R. Moret, S. Moss, S. Setton, S. Solin, *Graphite Intercalation Compounds I: Structure and Dynamics*, Springer Berlin Heidelberg, **2013**.

[85] M. S. Dresselhaus, G. Dresselhaus, *Advances in Physics* **2002**, *51*, 1–186.

[86] A. Herold, *Bulletin de la Société Chimique de France* **1955**, 999–1012.

[87] J. Dahn, R. Fong, M. Spoon, *Physical Review B* **1990**, *42*, 6424–6432.

[88] J. Dahn, *Physical Review B* **1991**, *44*, 9170–9177.

[89] M. Winter, J. O. Besenhard, M. E. Spahr, P. Novák, *Advanced materials* **1998**, *10*, 725–763.

[90] M. Heß, P. Novák, *Electrochimica Acta* **2013**, *106*, 149–158.

[91] M. A. Rodriguez, M. H. Van Benthem, D. Ingersoll, S. C. Vogel, H. M. Reiche, *Powder Diffraction* **2010**, *25*, 143–148.

[92] N. Sharma, V. K. Peterson, *Electrochimica Acta* **2013**, *101*, 79–85.

[93] A. Senyshyn, O. Dolotko, M. J. Mühlbauer, K. Nikolowski, H. Fuess, H. Ehrenberg, *Journal of the Electrochemical Society* **2013**.

[94] O. Dolotko, A. Senyshyn, M. J. Muhlbauer, K. Nikolowski, F. Scheiba, H. Ehrenberg, *Journal of the Electrochemical Society* **2012**, *159*, A2082–A2088.

[95] O. Hassel, H. Mark, *Zeitschrift für Physik* **1924**, *25*, 317–337.

[96] X. L. Wang, K. An, L. Cai, Z. Feng, S. E. Nagler, C. Daniel, K. J. Rhodes, A. D. Stoica, H. D. Skorpenske, C. Liang, W. Zhang, J. Kim, Y. Qi, S. J. Harris, *Scientific reports* **2012**, *2*, 747.

[97] V. Zinth, C. von Lüders, M. Hofmann, J. Hattendorff, I. Buchberger, S. Erhard, J. Rebelo-Kornmeier, A. Jossen, R. Gilles, *Journal of Power Sources* **2014**, *271*, 152–159.

[98] N. Daumas, A. Hérold, *Comptes Rendus Hebdomadaires Des Seances De L'Academie Des Sciences Serie C* **1969**, *268*, 373.

[99] S. Krishnan, G. Brenet, E. Machado-Charry, D. Caliste, L. Genovese, T. Deutsch, P. Pochet, *Applied Physics Letters* **2013**, *103*, 251904.

[100] K. Persson, V. A. Sethuraman, L. J. Hardwick, Y. Hinuma, Y. S. Meng, A. van der Ven, V. Srinivasan, R. Kostecki, G. Ceder, *Journal of Physical Chemistry Letters* **2010**, *1*, 1176–1180.

[101] A. Dimiev, G. Ceriotti, N. Behabtu, D. Zakhidov, M. Pasquali, R. Saito, J. Tour, *ACS Nano* **2013**, *7*, 2773–2780.

[102] A. Nyman, T. Zavalis, R. Elger, M. Behm, G. Lindbergh, *Journal of the Electrochemical Society* **2010**, *157*, A1236–A1246.

[103] S. J. Harris, A. Timmons, D. R. Baker, C. Monroe, *Chemical Physics Letters* **2010**, *485*, 265–274.

[104] P. Pietsch, D. Westhoff, J. Feinauer, J. Eller, F. Marone, M. Stampanoni, V. Schmidt, V. Wood, *Nature Communications* **2016**, *7*, 12909.

[105] D. M. Bernardi, J.-Y. Go, *Journal of Power Sources* **2011**, *196*, 412–427.

[106] T. R. Ferguson, M. Z. Bazant, *Journal of the Electrochemical Society* **2012**, *159*, A1967–A1985.

[107] V. Srinivasan, J. Newman, *Journal of the Electrochemical Society* **2004**, *151*, A1517.

[108] A. Yamada, H. Koizumi, N. Sonoyama, R. Kanno, *Electrochemical and Solid-State Letters* **2005**, *8*, A409.

[109] J. Wang, X. Sun, *Energy & Environmental Science* **2015**, *8*, 1110–1138.

[110] T. R. Ferguson, M. Z. Bazant, *Electrochimica Acta* **2014**, *146*, 89–97.

[111] E. Bohn, T. Eckl, M. Kamlah, R. McMeeking, *Journal of the Electrochemical Society* **2013**, *160*, A1638–A1652.

[112] X. Zhang, W. Shyy, A. Marie Sastry, *Journal of the Electrochemical Society* **2007**, *154*, A910.

[113] M. T. McDowell, S. W. Lee, W. D. Nix, Y. Cui, *Advanced materials* **2013**, *25*, 4966–85.

[114] L. Luo, J. Wu, J. Luo, J. Huang, V. P. Dravid, *Scientific reports* **2014**, *4*, 3863.

[115] Y. Liu, S. Zhang, T. Zhu, *ChemElectroChem* **2014**, *1*, 706–713.

[116] A. Bordes, E. De Vito, C. Haon, A. Boulineau, A. Montani, P. Marcus, *Chemistry of Materials* **2016**, *28*, 1566–1573.

[117] I. Grillo, *Small-Angle Neutron Scattering and Applications in Soft Condensed Matter*, Springer, Netherlands, **2008**.

[118] R. Gilles, A. Ostermann, C. Schanzer, B. Krimmer, W. Petry, *Physica B: Condensed Matter* **2006**, *385-386*, 1174–1176.

[119] R. Gilles, A. Ostermann, W. Petry, *Journal of Applied Crystallography* **2007**, *40*, 428–432.

[120] S. Mühlbauer, A. Heinemann, A. Wilhelm, L. Karge, A. Ostermann, I. Defendi, A. Schreyer, W. Petry, R. Gilles, *Nuclear Instruments and Methods in Physics Research Section A: Accelerators Spectrometers Detectors and Associated Equipment* **2016**, *832*, 297–305.

[121] G. Kostorz, *Neutron Scattering*, Academic Press, New York, **1979**.

[122] L. D. Landau, E. M. Lifshitz, *Course of theoretical physics*, Elsevier, **2013**.

[123] I. Bressler, J. Kohlbrecher, A. F. Thunemann, *Journal of Applied Crystallography* **2015**, *48*, 1587–1598.

[124] I. Bressler, SASFit Manual Scattering Cross Section, Generic, **2011**.

[125] H. Frielinghaus in *Lectures of the JCNS Laboratory Course*, (Eds.: T. Brückel, G. Heger, D. Richter, G. Roth, R. Zorn), Schriften des Forschungszentrums Jülich, Forschungszentrum Jülich GmbH, Jülich, **2012**, Chapter 5.

[126] G. Sandi, P. Thiyagarajan, K. A. Carrado, R. E. Winans, *Chem. Mater.* **1999**, *11*, 235–240.

[127] G. Roth in *Lectures of the JCNS Laboratory Course*, (Eds.: T. Brückel, G. Heger, D. Richter, G. Roth, R. Zorn), Schriften des Forschungszentrums Jülich, Forschungszentrum Jülich GmbH, Jülich, **2012**, Chapter 4.

[128] A. Guinier, G. Fournet, *Small-angle scattering of x-rays*, Wiley, New York, **1955**.

[129] G. Volkmar, *Zeitschrift für angewandte Physik* **1957**, *9*, 43–55.

[130] J. Teixeira, *Journal of Applied Crystallography* **1988**, *21*, 781–785.

[131] D. Schwahn, D. Richter, M. Lin, L. J. Fetter, *Macromolecules* **2002**, *35*, 3762–3768.

[132] B. Hammouda, The SANS Toolbox, Report, NIST Center for Neutron Research (www.ncnr.nist.gov/staff/hammouda).

[133] P. W. Schmidt, *Journal of Applied Crystallography* **1991**, *24*, 414–435.

[134] Y. B. Melnichenko, G. D. Wignall, *Journal of Applied Physics* **2007**, *102*, 021101.

[135] G. Porod, *Kolloid-Zeitschrift* **1951**, *124*, 83–114.

[136] L. A. Feigin, D. I. Svergun, *Structure Analysis by Small-Angle X-Ray and Neutron Scattering*, Plenum Press, New York, **1987**.

[137] A. Heinemann, S. Mühlbauer, *Journal of large-scale research facilities* **2015**, *1*, A10.

[138] Experimental Facilities H. Maier-Leibnitz Zentrum (MLZ), Report, Forschungs-Neutronenquelle H. Maier-Leibnitz (FRM II) Technische Universität München, **2013**.

[139] J. S. Pedersen, D. Posselt, K. Mortensen, *Journal of Applied Crystallography* **1990**, *23*, 321–333.

[140] C. F. Majkrzak, C. Metting, B. Maranville, J. A. Dura, S. Satija, T. Udovic, N. F. Berk, *Physical Review A* **2014**, *89*.

[141] M. J. Hollamby, *Physical chemistry chemical physics : PCCP* **2013**, *15*, 10566–79.

[142] K. M. Ford, B. G. Konzman, J. F. Rubinson, *Anal Chem* **2011**, *83*, 9201–5.

[143] S. M. Mamun, M. Herstedt, K. Oikawa, T. Gustafsson, T. Otomo, M. Furusaka, T. Kamiyama, H. Sakaebe, K. Edström, *Applied Physics A: Materials Science & Processing* **2002**, *74*, s1028–s1030.

[144] A. P. Radlinski, M. Mastalerz, A. L. Hinde, M. Hainbuchner, H. Rauch, M. Baron, J. S. Lin, L. Fan, P. Thiyagarajan, *International Journal of Coal Geology* **2004**, *59*, 245–271.

[145] P. J. Hall, S. D. Brown, J. M. Calo, *Fuel* **2000**, *79*, 1327–1332.

[146] C. A. Stoltz, B. P. Mason, J. Hooper, *Journal of Applied Physics* **2010**, *107*, 103527.

[147] C. A. Bridges, X.-G. Sun, J. Zhao, M. P. Paranthaman, S. Dai, *The Journal of Physical Chemistry C* **2012**, *116*, 7701–7711.

[148] H. Wang, R. G. Downing, J. A. Dura, D. S. Hussey in *Polymers for energy storage and delivery: polyelectrolytes for batteries and fuel cells. Vol. 1096*, American Chemical Society, **2012**, pp. 91–106.

[149] N. Sharma, V. K. Peterson, M. M. Elcombe, M. Avdeev, A. J. Studer, N. Blagojevic, R. Yusoff, N. Kamarulzaman, *Journal of Power Sources* **2010**, *195*, 8258–8266.

[150] O. Dolotko, A. Senyshyn, M. J. Mühlbauer, K. Nikolowski, H. Ehrenberg, *Journal of Power Sources* **2014**, *255*, 197–203.

[151] A. Senyshyn, M. J. Muhlbauer, O. Dolotko, M. Hofmann, H. Ehrenberg, *Scientific reports* **2015**, *5*, 18380.

[152] J. B. Siegel, X. Lin, A. G. Stefanopoulou, D. S. Hussey, D. L. Jacobson, D. Gorsich, *Journal of the Electrochemical Society* **2011**, *158*, A523.

[153] A. Senyshyn, M. J. Mühlbauer, K. Nikolowski, T. Pirling, H. Ehrenberg, *Journal of Power Sources* **2012**, *203*, 126–129.

[154] X. Zhang, T. W. Verhallen, F. Labohm, M. Wagemaker, *Advanced Energy Materials* **2015**, *5*, n/a–n/a.

[155] I. Buchberger, S. Seidlmayer, A. Pokharel, M. Piana, J. Hattendorff, P. Kudejova, R. Gilles, H. A. Gasteiger, *Journal of the Electrochemical Society* **2015**, *162*, A2737–A2746.

[156] S.-C. Yin, Y.-H. Rho, I. Swainson, L. Nazar, *Chemistry of materials* **2006**, *18*, 1901–1910.

[157] D. Aurbach, E. Zinigrad, Y. Cohen, H. Teller, *Solid State Ionics* **2002**, *148*, 405–416.

[158] J. Steiger, D. Kramer, R. Mönig, *Electrochimica Acta* **2014**, *136*, 529–536.

[159] J. Wandt, C. Marino, H. A. Gasteiger, P. Jakes, R.-. A. Eichel, J. Granwehr, *Energy & Environmental Science* **2015**, *8*, 1358–1367.

[160] M. E. Spahr, H. Wilhelm, T. Palladino, N. Dupont-Pavlovsky, D. Goers, F. Joho, P. Novák, *Journal of Power Sources* **2003**, *119-121*, 543–549.

[161] Imerys, Spec Sheet SLP30, Report.

[162] S. J. Harris, E. K. Rahani, V. B. Shenoy, *Journal of the Electrochemical Society* **2012**, *159*, A1501–A1507.

[163] T. Placke, V. Siozios, R. Schmitz, S. F. Lux, P. Bieker, C. Colle, H. W. Meyer, S. Passerini, M. Winter, *Journal of Power Sources* **2012**, *200*, 83–91.

[164] U. Keiderling, www.psi.ch/sinq/sansii/bersans (26.04.2016), **2012**.

[165] U. Keiderling, *Applied Physics A* **2002**, *74*, s1455–s1457.

[166] U. Keiderling, BerSANS Data Reduction Manual, Manuscript, **2000**.

[167] S. Seidlmayer, L. Karge, R. Gilles, BERSANS Tutorial v2, Manuscript, **2013**.

A. Appendix: Impedance measurements

A.1. Fit of impedance measurements

Experimental impedance data (PEIS) were fitted with a MATLAB routine which implements nonlinear curve fitting for a list of theoretical impedance models. Alternatively, simple models (e. g. the high frequency resistance of separators) were fitted with the ZFit function of the EC-Lab software (V10, Biologic) which yielded similar results. All MATLAB impedance models follow the models that are discussed in section 4.1. The angular frequency is replaced by the frequency in Hz, resistances are given in Ω and capacitances in F or $\mathrm{Fs}^{\gamma-1}$. The terms "c" and "q" are used to distinguish the model with pure capacitance or CPE-behavior. A Randles circuit is also included in the list.

Finally, the following models are considered where the complex impedance Z is given as a function of frequency f and the various input parameters such as high frequency ionic resistance in the separator, ionic resistance in the electrode, transfer resistances, capacities and exponential factors such as γ for CPE elements. Typical areal capacitance values ($10^{-5}\mathrm{F/cm^2}$) multiplied by the total active particle surface yield reasonable starting values for the fit.

Models for fitting separator measurements:

$$\begin{aligned} \text{hfr+c:} \quad Z =& R_{\mathrm{HFR}} + \frac{1}{Q_{\mathrm{t}} i 2\pi f} \\ \text{hfr+q:} \quad Z =& R_{\mathrm{HFR}} + \frac{1}{Q_{\mathrm{t}} (i 2\pi f)^{\gamma}} \end{aligned} \tag{A.1}$$

Models for fitting TLM blocking and faradaic:

$$
\begin{aligned}
\text{hfr+tlmc:} \quad & Z = R_{\mathrm{HFR}} + \sqrt{\frac{R_{\mathrm{ion}}}{Q_{\mathrm{t}} i 2\pi f}}\, coth\left(\sqrt{Q_{\mathrm{t}} i 2\pi f \cdot R_{\mathrm{ion}}}\right) \\
\text{hfr+tlmq:} \quad & Z = R_{\mathrm{HFR}} + \sqrt{\frac{R_{\mathrm{ion}}}{Q_{\mathrm{t}} (i 2\pi f)^{\gamma}}}\, coth\left(\sqrt{Q_{\mathrm{t}} (i 2\pi f)^{\gamma} \cdot R_{\mathrm{ion}}}\right) \\
\text{hfr+tlmqfaradaic:} \quad & Z = R_{\mathrm{HFR}} + \sqrt{\frac{R_{\mathrm{ion}} R_{\mathrm{t}}}{1 + R_{\mathrm{t}} Q_{\mathrm{t}} (i 2\pi f)^{\gamma}}} \ldots \\
& \ldots coth\left(\sqrt{\frac{(1 + R_{\mathrm{t}} Q_{\mathrm{t}} (i 2\pi f)^{\gamma}) \cdot R_{\mathrm{ion}}}{R_{\mathrm{t}}}}\right)
\end{aligned}
\tag{A.2}
$$

Other models for fitting equivalent circuits:

$$
\begin{aligned}
\text{hfr+rcq:} \quad & Z = R_{\mathrm{HFR}} + \frac{R_{\mathrm{t}}}{1 + R_{\mathrm{t}} Q_{\mathrm{t}} (i 2\pi f)^{\gamma}} \\
\text{randles:} \quad & Z = R_{\mathrm{HFR}} + \frac{1}{\frac{1}{R_{\mathrm{t}} + A_{\mathrm{W}} (i 2\pi f)^{-\alpha}} + Q_{\mathrm{t}} (i 2\pi f)^{\gamma}}
\end{aligned}
\tag{A.3}
$$

where for the Randles circuit fit, A_{W} is the Warburg coefficient and α the Warburg alpha (typically 0.5). The variable `relerrsum` was used for error estimation, see section A.4.

Figure A.1 (left) shows the TLM fit in blocking conditions for graphite (t1) which agrees well with the data points. An exemplary fit for the symmetric cell with harvested graphite (t1) in faradaic condition is shown in figure A.1 (right). The last data points towards low frequencies where a Warburg diffusion tail is visible were left out for fitting in order to get a meaningful transfer resistance from the faradaic TLM model. For all faradaic graphite measurements the last 15 data points were left out. For NMC the last 10 data points were left out because also here, a Warburg tail is visible. The first data points at 500 kHz are also at the edge of the device resolution and quite noisy and therefore the first two points are left out in all fits. Fitted resistances are shown in table A.1 for NMC and in table A.2 for graphite.

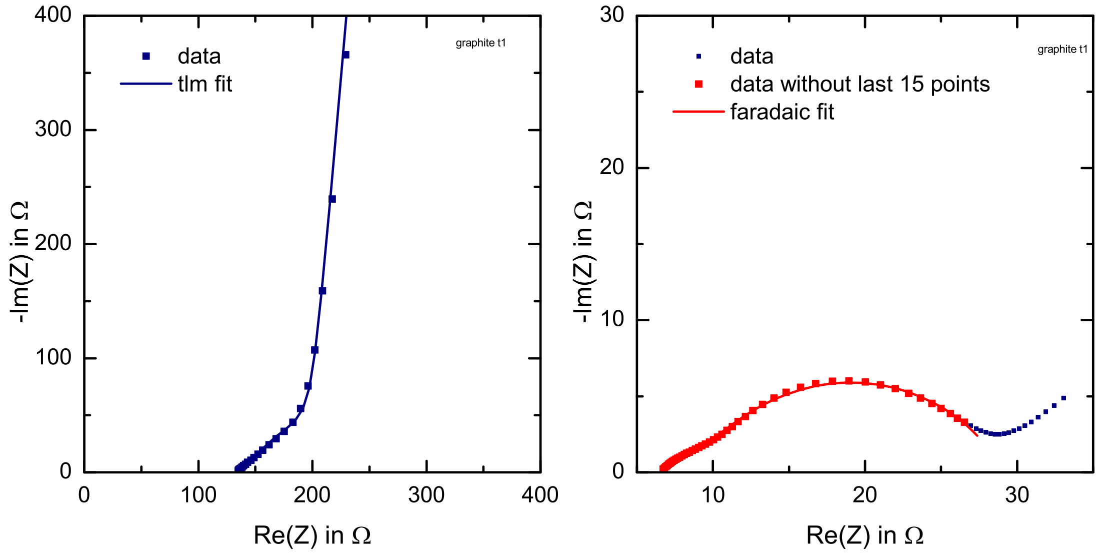

Figure A.1.: Left: Pristine graphite t1 in symmetric cell with 10 mM TBAClO$_4$ salt, data points and fit with blocking conditions TLM model and free γ. Right: Harvested graphite t1 at 50% SoC in symmetric cell with LP572 electrolyte, data points and fit with faradaic conditions TLM model and free γ. The last 15 data points were left out for fitting to exclude the Warburg behavior.

Resistance in Ω, TLM blocking, measured with 10mM $TBAClO_4$					
	10mM $TBAClO_4$		converted to LP572		
	$2R_{\mathrm{ion}}$	HFR	$2R_{\mathrm{ion}}$	HFR	mean rel. error
t0	139.9	68.4	7.0	3.4	2 %
t1	191.7	61.7	9.5	3.1	4 %
t2	571.1	62.9	28.4	3.1	4 %
t3	735.0	62.5	36.5	3.1	4 %

Resistance in Ω, TLM faradaic, measured with LP572				
	$2R_{\mathrm{t}}$	HFR	$2R_{\mathrm{ion}}$	mean rel. error
t0	2422.2	5.3	2.7	6 %
t1	1000.1	6.3	14.6	4 %
t2	340.0	7.4	29.6	3 %
t3	267.3	5.7	15	3 %

Table A.1.: Fitted parameters for NMC from MATLAB. With mean relative error, i. e. the mean relative distance of model point and data point. Data was converted to LP572 conductivity for comparison. The MATLAB-fitted values for R_{ion} in faradaic condition with LP572 are with a significant error; i. e. in the Nyquist diagram it is hard to tell where the linear slope ends and the half-circle begins. Compare figure 4.5 and 4.14.

Resistance in Ω, TLM blocking, measured with 10mM TBAClO$_4$					
	10mM TBAClO$_4$		converted to LP572		
	$2R_{\mathrm{ion}}$	HFR	$2R_{\mathrm{ion}}$	HFR	mean rel. error
t0	110.3	124.0	5.5	6.2	1 %
t1	185.3	133.9	9.2	6.7	1 %
t2	338.9	147.8	16.8	7.3	1 %
t3	516.2	124.3	25.7	6.2	1 %

Resistance in Ω, TLM faradaic, measured with LP572				
	$2R_{\mathrm{t}}$	HFR	$2R_{\mathrm{ion}}$	mean rel. error
t0	32.9	7.1	5.3	1 %
t1	19.8	6.1	10.0	1 %
t2	16.7	6.4	15.6	1 %
t3	16.4	5.8	16.6	4 %

Table A.2.: Fitted parameters for graphite from MATLAB with mean relative error, i. e. the mean relative distance of model point and data point. Data was converted to LP572 conductivity for comparison.

Fit function

Impedance functions are fitted with MATLAB by using the following code. Basically, the routine uses the MATLAB function `fminsearch` to minimize the error function which is the sum of squared errors in distance of measured data points to fitted points. Various impedance models can be selected.

```
% A custom MATLAB fit function

function [estimates, model, relerrsum] = ...
 fitImpAll(fdata, redata, negimdata, start_point, type, weight)
% A nonlinear fit function for impedance models
% call fit function, INPUT: f, Re(Z), -Im(Z), start parameters
% (number depends on model type), model type, weighing yes or
% weighing yes or no? OUTPUT: estimated paramters, fitted data,
% sum of relative errors (i.e. ca. total relative error)
% parameter options are given and can be de/selected

%model is handle for impedance function
model = @imp1fun;

% fminsearch options
opt.MaxFunEvals=10000;
opt.MaxIter=100000; %maximum number of iterations
opt.TolFun=0.000001;
estimates = fminsearch(model, start_point, opt);

% the impedeance function imp1fun accepts curve parameters as
% inputs and gives back sse (sum of squared error between model
% and measure) and the fitted curve fitdata, fminsearch
% minimizes sse

 function [wsse, fitdata] = imp1fun(params)
  hfr = params(1);
  q = params(2);

  switch type
   % selects fit model type and impedance expression
   case 'hfr+c' %serial res. and capacitance
    fitdata =  hfr + 1 ./ (q.*(i.*2.*pi.*fdata)) ;
   case 'hfr+q' %serial res. and cpe
```

```
  g = params(3); %gamma
  fitdata =  hfr + 1 ./ (q.*(i.*2.*pi.*fdata).^g) ;
 case ’hfr+tlmc’ %hfr and tlm with capacitance
  rion = params(3);
  fitdata =  hfr + sqrt(rion ./ (q .* (i.*2.*pi.*fdata))) ...
   .* coth(sqrt(q.*(i.*2.*pi.*fdata).*rion));
 case ’hfr+tlmq’ %hfr and tlm with cpe
  rion = params(3);
  g = params(4);
  fitdata =  hfr + sqrt(rion ./ ...
   (q .* (i.*2.*pi.*fdata).^g) ) ...
   .* coth(sqrt(q.*(i.*2.*pi.*fdata).^g.*rion));
 case ’hfr+tlmqfaradaic’ %hfr and tlm with cpe
  rion = params(3);
  g = params(4);
  rct = params(5);
  fitdata =  hfr + sqrt(rion .* rct ./ ...
   (1+ rct.*q.*(i.*2.*pi.*fdata).^g) ) .* ...
   coth( sqrt( rion .*...
   (1 + rct.*q.*(i.*2.*pi.*fdata).^g) ./ rct ) );
 case ’hfr+rcq’ %serial res. and RC arc with cpe
  rtrans = params(3);
  g = params(4);
  fitdata =  hfr + rtrans ./ ...
   (1+rtrans.*q.*(i.*2.*pi.*fdata).^g);
 case ’randles’ %serial res. and RC arc with cpe
  rtrans = params(3);
  g = params(4);
  aw = params(5); %warburgcoeff
  a = params(6); %alpha warburg
  fitdata =  hfr + 1 ./ (1./(rtrans + aw./ ...
   ((i.*2.*pi.*fdata).^a)) + q.*(i.*2.*pi.*fdata).^g);
end;

% errorfunction of individual data point, error measured
% by complex distance
switch weight
 %select weighing of error function, none or relative values
 case ’none’
  wErrorVector = abs( fitdata - (redata - i.*negimdata));
```

```
    %./abs((redata - i.*negimdata));
   case 'relative'
    wErrorVector = abs( fitdata - (redata - i.*negimdata)) ...
     ./abs((redata - i.*negimdata));
  end;
  wsse = sum(wErrorVector .^ 2);
  % sum of individual errors squared - this is to be minimized
 end
relerrsum = sum((wErrorVector./abs((redata - i.*negimdata))))...
 /length(redata);
% relative sum of individual erros
end
```

Fit script

The MATLAB fit function is called by the following script which also plots the data and fit. Input is impedance data loaded to the MATLAB workspace, typical start parameters are given in the script and selected according to the used model. The fit results are then exported for detailed plots.

```
% A script to fit input data to an impedance function
% MATLAB script

%%%% INPUT SPECIFICATION %%%%
% input: table with 3 columns:
% 1) f/Hz, 2) Re(Z)/Ohm, 3) -Im(Z)/Ohm
input=gra_harvsym_t1; %load input table from MATLAB workspace
fcolumn=1; %freq. values in which column?
%%%% end of INPUT SPECIFICATION %%%%

%%%% OPTIONS %%%%
% start/end fit at data point nr.
fstart=3;  %leave out first 2 points (noisy)
fend=height(input)-15; %leave out x end points?

% specify type of fit model: 'hfr+c' 'hfr+q' 'hfr+tlmc'
% 'hfr+tlmq' 'hfr+tlmqfaradaic' 'hfr+rcq' 'randles'
type='hfr+tlmqfaradaic';

% start values for parameters, here
% R in Ohm, q in F*s^(gamma-1)
%for hfr+c [rhfr, q]
%for hfr+q [rhfr, q, gamma]
%for hfr+tlmc [rhfr, q, rion]
%for hfr+tlmq [rhfr, q, rion, gamma]
%for hfr+tlmqfaradaic [rhfr, q, rion, gamma, rtrans]
%for hfr+rcq [rhfr, q, rtrans, gamma]
%for randles ...
%     [rhfr, q, rtrans, gamma, warburgcoef, warburgalpha]

% typical startvalues
%param0=[5 0.000001 20]; %hfr+q
%param0=[70 0.0005  100 0.9]; %hfr+tlmq
param0=[4 0.001  10 0.9 40]; %hfr+tlmqfaradaic
```

```
%param0=[6 0.0001  300 0.9 ]; %hfr+rcq
%param0=[10 0.001  20 0.9 5 0.5]; %randles

% specify error function weighing 'none' or 'relative'
weight='none';
%%%% end of OPTIONS %%%%

fdata=input{fstart:fend,fcolumn};
redata=input{fstart:fend,2};
negimdata=input{fstart:fend,3};

% call fit function and give estimate vector and
% model handle back
[estimates, model, relerrsum] = ...
    fitImpAll(fdata,redata,negimdata,param0,type,weight);

% plot original and fit
plot(redata, negimdata, '*')
hold on

% get sse
% (error based on complex distance of data and model point)
% and get model point 'fitdata' from model
[sse, fitdata] = model(estimates);

plot(real(fitdata(:)),-imag(fitdata(:)), 'og')

% plot values to console
estimates
% sse
relerrsum
```

A.2. Half cell PEIS measurements

After the rate test all half cells were measured in a standard PEIS experiment. The results (figure A.2) show the combined signal from Li counter electrode and NMC or graphite electrode and it is therefore hard to draw conclusions. The measurement was done in discharged state after the last 1C cycle of the rate test and at 25° C.

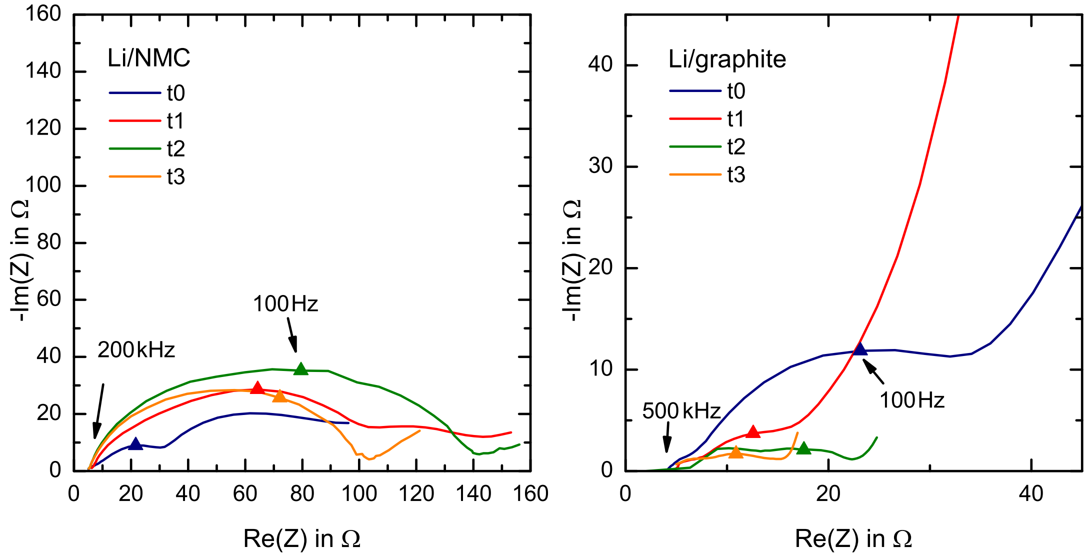

Figure A.2.: PEIS measurements of Li/NMC (left) and Li/graphite (right) half cells. Since no reference was used, the Li contribution cannot be separated. Area 1.54 cm^2.

A.3. Full cell Ragone plot

A Ragone plot for a full cell can be calculated from half cell data by using several simple assumptions. Here, we assume that the anode is balanced 1:1 to the cathode and that the cathode is generally the rate limiting factor. Then, one can calculate the total weight per area A of an assumed full cell:

$$m_{\text{tot. full}}/A = \sum_{\text{a+c}} m_{\text{active}}/A \cdot 1/c_{\text{wt\%}} + \sum_{\text{a+c}} m_{\text{electrolyte}}/A + m_{\text{foils+separator}}/A \quad (A.4)$$

with the loading m_{active}/A (both anode and cathode) and the factor $c_{\text{wt\%}} = 0.95$ or 0.96 for graphite or NMC, respectively. The weight of the electrolyte in the pores of the electrodes scales with thickness and thus with loading. Here, we assume a porosity ϵ of 30% and neglect binder and carbon black content. So for the cathode (and for the anode accordingly) we get:

$$m_{\text{electrol. cathode}}/A = m_{\text{active}}/A \cdot 1/c_{\text{wt\%}} \cdot 1/\rho_{\text{NMC}} \cdot \epsilon \cdot \rho_{\text{electrolyte}} \tag{A.5}$$

An electrolyte density of $\rho_{\text{electrolyte}} = 1.2\,\text{g/cm}^3$ is typical. The areal weight of Cu and Al foils plus electrolyte filled separator can be assumed to be ca. $9\,\text{mg/cm}^2$ in total, if the metal foils are assumed to be coated from both sides as in commercial cells, compare table 3.1. For the plot, capacity per weight and current per weight can now be calculated by dividing the measured capacity and current values by the total weight as derived above. The result is a full cell level Ragone plot within the assumptions, cell housing and tabs are not included.

A.4. Error estimation

Reported cell values x are generally the mean of several cells with a sample standard deviation $s = \sqrt{\sum_{\text{i}}^{\text{n}}((x_{\text{i}} - \bar{x})^2/(n-1))}$ which is plotted as error bar. The standard error of the mean is smaller by a factor of $\sqrt{n}$, but for small n (2 to 3) the difference is not important. Strictly, to judge significance the 95% confidence interval of a mean value would be given by $\pm 1.96 \cdot s/\sqrt{n}$, which for small n however is more or less in the range of the standard deviation. Simple root mean square error propagation was used to give an error estimation of calculated quantities. E. g. the error in tortuosity τ was calculated applying equation 4.7:

$$\Delta\tau = \sqrt{\left(\frac{A\kappa}{t} R_{\text{ion}} \Delta\epsilon\right)^2 + \left(\frac{A\kappa\epsilon}{t} \Delta R_{\text{ion}}\right)^2 + \left(-\frac{A\kappa}{t^2} \epsilon R_{\text{ion}} \Delta t\right)^2} \tag{A.6}$$

The errors in ϵ and thickness t are given from the empirical scatter of data and are below 10% and 5% respectively.

The error in R_{ion} is given as the error of the non-linear fit which involves pure and mixed second derivatives (with respect to the various fit parameters) of the sum of squared distances between fit and data points. This is not trivial to calculate and we use a simplified approach here by evaluating the mean relative distances of data points to fit points. The mean relative distance or mean relative error (`relerrsum`) is the sum of the magnitudes of the relative distances between fit points and data points in the Re(Z)/-Im(Z)-plane divided by the number of data points, “relative” here means relative to distance of data point from origin. Table A.1 and table A.2 state mean relative error values of 2 to 4% for NMC and 1% for graphite for the experimental data in blocking condition. A sensitivity analysis of the parameter R_{ion} shows that a variation of R_{ion} by 5% in the theoretical model

(e. g. equation A.2, “hfr+tlmq”) results in a shift of around the same percentage for model data points in the Nyquist plane for the relevant frequencies. Since R_{ion} is directly correlated to the distance of the data points in the Nyquist plane we can take this simplification as a good estimate for the error. So the error in R_{ion} is typically well below 5% here.

A.5. Overview of cycling and impedance cells

.

cell ID	cell type	measurement	description	limiting electrode area in cm^2	loading electrode 1 mAh/cm^2	loading electrode 1 mAh/cm^2	electrolyte	separator
june5	pouch	TLM	gr vs. gr	2.2708	2.82	2.94	TBA10	C2325
june6	pouch	TLM	gr vs. gr	2.3686	2.84	2.86	TBA50	C2325
june7	pouch	TLM	gr vs. gr	2.4136	2.83	2.92	TBA200	C2325
june8	pouch	TLM	gr vs. gr	2.4168	2.93	2.85	TBA700	C2325
nove2 (c)	coin	cycling	Gr0 vs. Li	1.54	0.55		LP572	glass-fiber
nove3	coin	cycling	Gr1 vs. Li	1.54	1.47		LP572	glass-fiber
nove4 (v2)	coin	cycling	Gr2 vs. Li	1.54	3.03		LP572	glass-fiber
nove5	coin	cycling	Gr3 vs. Li	1.54	4.4		LP572	glass-fiber
nove6	coin	cycling	Gr0 vs. Li	1.54	0.59		LP572	glass-fiber
nove7	coin	cycling	Gr1 vs. Li	1.54	1.63		LP572	glass-fiber
nove8	coin	cycling	Gr2 vs. Li	1.54	3.08		LP572	glass-fiber
nove9	coin	cycling	Gr3 vs. Li	1.54	4.36		LP572	glass-fiber
z1_Gr0TLM_3+5	T-cell	TLM	gr vs. gr	0.95	0.65	0.65	TBA10	glass-fiber
z3_Gr1TLM_2+5	T-cell	TLM	gr vs. gr	0.95	0.68	1.64	TBA10	glass-fiber
z4_Gr2TLM_2+5	T-cell	TLM	gr vs. gr	0.95	3.08	3.11	TBA10	glass-fiber
z5_Gr3TLM_1+3	T-cell	TLM	gr vs. gr	0.95	4.5	4.5	TBA10	glass-fiber
nove10	coin	cycling	NMC0.2 vs. Li	1.54	0.86		LP572	glass-fiber
nove11	coin	cycling	NMC1.2 vs. Li	1.54	1.56		LP572	glass-fiber
nove12	coin	cycling	NMC2.3 vs Li	1.54	3.25		LP572	glass-fiber
nove13	coin	cycling	NMC3.3 vs Li	1.54	4.78		LP572	glass-fiber
nove14	coin	cycling	NMC0.1 vs Li	1.54	0.77		LP572	glass-fiber
nove15	coin	cycling	NMC1.3 vs Li	1.54	1.5		LP572	glass-fiber
nove16	coin	cycling	NMC2.2 vs Li	1.54	3.3		LP572	glass-fiber
nove17	coin	cycling	NMC3.2 vs Li	1.54	5.16		LP572	glass-fiber
nmc_0p1_0p4	T-cell	TLM	NMC vs. NMC	0.95	0.66	0.89	TBA10	glass-fiber
nmc_1p3_1p5	T-cell	TLM	NMC vs. NMC	0.95	1.43	1.55	TBA10	glass-fiber
nmc_2p2_2p6	T-cell	TLM	NMC vs. NMC	0.95	3.46	3.66	TBA10	glass-fiber
nmc_3p4_3p5	T-cell	TLM	NMC vs. NMC	0.95	4.87	5.39	TBA10	glass-fiber

Table A.3.: Overview of cells built for cycling and AC impedance experiments. The electrolyte TBAx is EC:DMC (1:1) with x mM $TBAClO_4$. NMC is always NMC-111.

B. Appendix: SANS

B.1. Mesh averaging simulation

The averaged Porod invariant $\langle\langle \Delta\rho^2 \rangle\rangle$ was calculated with MATLAB according to the following source code.

```
% script to simulate <<delta rho^2>> (Porod), averaged over
% mesh coherence
% volumes

% geometric idea
% phase0|phase2|phase1
% length from left to right = 2 (2x l_coh which is set to 1)

clear all;

N=70; %number of meshes
phases=10; %number of steps
drhosqu1=1.2; %delta rho^2 of phase 1
drhosqu2=1.0; %delta rho^2 of phase 2

for j=0:(phases-1)
l2=j*1/(phases-1); %this phase grows (from left)
l1=1-l2; %this phase shrinks (rest at right)
l1p(j+1)=l1;
l2p(j+1)=l2;

sum1=0; %initialize for loop
sum2=0;

for i=0:N-1 %sum over all N meshes
    if i<=l2*(N-1) %if i/N (=translation for mesh i) < l2
        phi0=1-i/(N-1); %phase 0 shrinked by mesh moving into solid
        phi2=i/(N-1); %phase 2 growing (as long as still within l2)
        phi1=0; %phase 1 not in range of V_coh
```

```
        sum1=sum1+phi0*phi1; %volume fraction sum
        sum2=sum2+phi0*phi2;
    else
        phi0=1-i/(N-1);
        phi2=l2; % phase 2 reaches max.
        phi1=i/(N-1)-l2; % phase 1 growing (-phase2)
        sum1=sum1+phi0*phi1;
        sum2=sum2+phi0*phi2;
    end;
    phi0p(j+1,i+1)=phi0;
    phi1p(j+1,i+1)=phi1;
    phi2p(j+1,i+1)=phi2;
end;
total(j+1)=1/N*(drhosqu1*sum1+drhosqu2*sum2); %volume fraction
% times delta rho, result
end;

hold on; %plot
plot(total);
```

B.2. Cycling data of cells measured with SANS

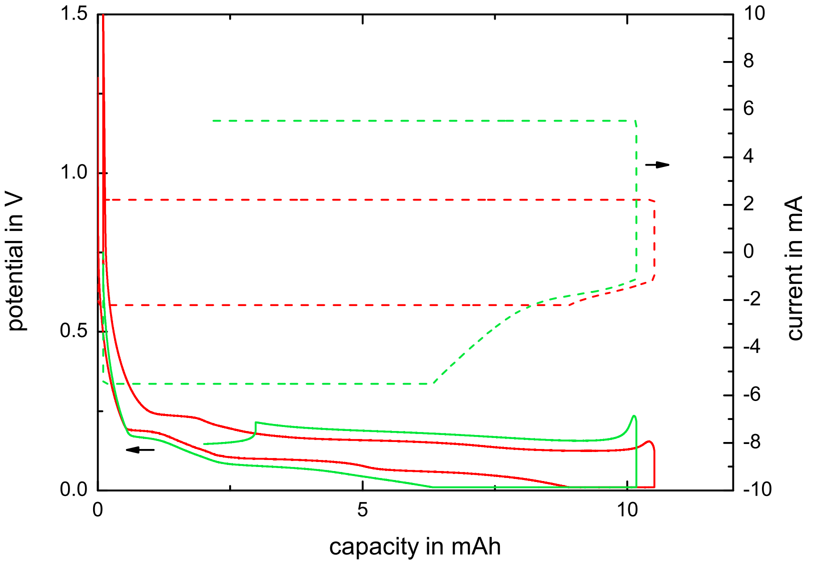

Figure B.1.: Potential and current vs. capacity for Li/C half cell (sept26), as measured during SANS experiment.

The half cell sept26 (see table B.1 for all cell IDs) underwent two formation cycles at C/10, two at C/5 (0.01 V to 1.5 V) and was set to 1.5 V before SANS measurement. In the first experiment the cell was charged from 1.5 V to 0.01 V with C/5 (CCCV) and discharged at the same rate (CC). After a short period in OCV condition, the cell was charged (CCCV) and discharged (CC) with C/2. The last cycle was not fully completed due to time restrictions at the measurement facility.

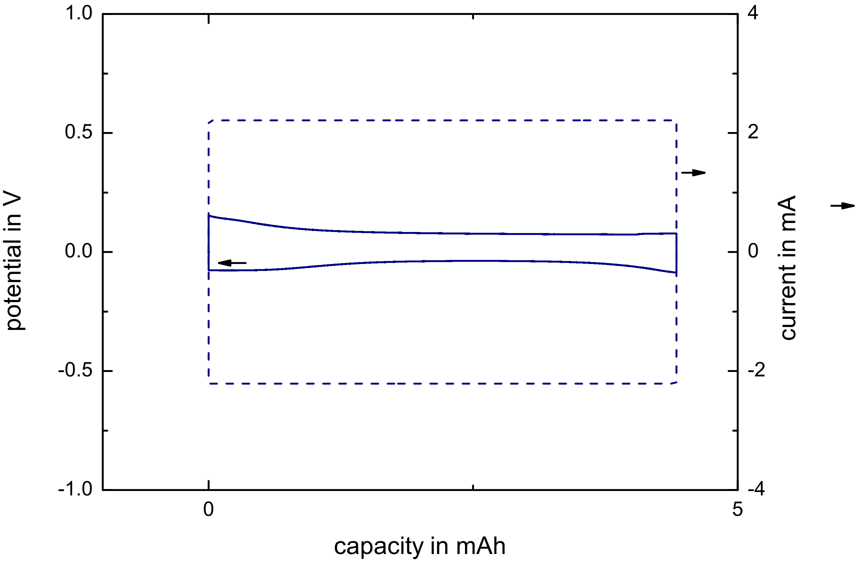

Figure B.2.: Potential and current vs. capacity for Li/Li symmetric cell (sept33), as measured during SANS experiment.

The symmetric cell sept33 contained to Li foils. It was fresh and had seen no prior cycling. During the SANS measurement Li was shuttled by applying a small overvoltage of ca. 100 mV. Current was controlled to 2 mA in order to equal the current density for the Li/C half cell benchmark.

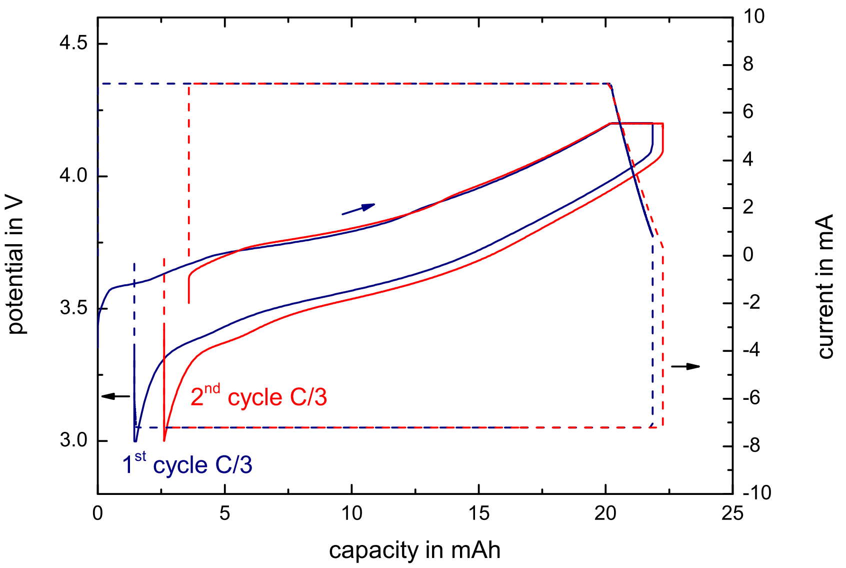

Figure B.3.: Potential and current vs. capacity for balanced C/NMC full cell (nov1), as measured during SANS experiment.

The full cell nov1 underwent two formation cycles at C/10 with 3 to 4.2 V. Then, in November 2013 it was cycled at C/3 in situ at the SANS experiment. After a 3 month break, it underwent one check-up cycle and was cycled a second time at the SANS instrument.

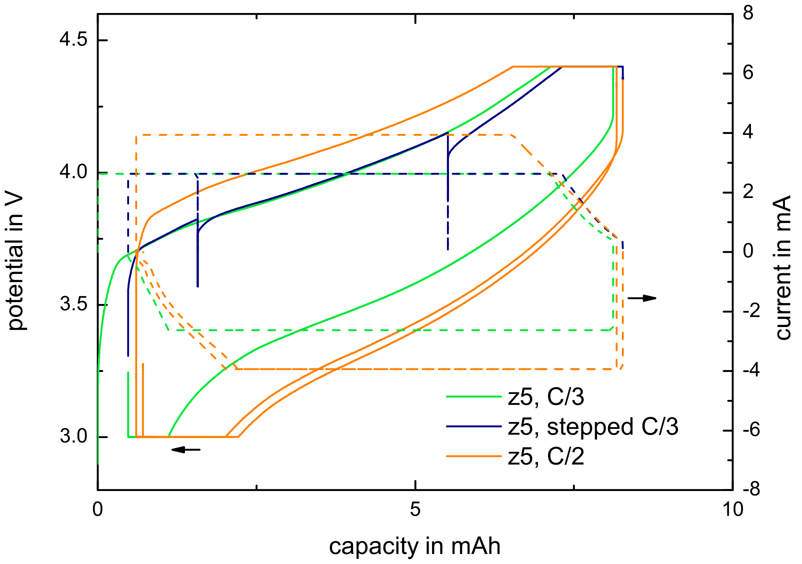

Figure B.4.: Potential and current vs. capacity for balanced C/NMC full cell (z5), as measured during SANS experiment.

The balanced full cell z5 underwent two formation cycles at C/10 (3 to 4.2 V) and was degassed afterwards. In the first SANS experiment the cell was charged from 3 to 4.4 V (higher cut-off voltage to compensate for irreversible loss during formation) at C/3 in CCCV mode and discharged in the same manner. In the second experiment the cell was charged at C/3 with two interruptions (CCCV). In the third experiment the cell was cycled at C/2 (CCCV) for one discharge and a complete cycle.

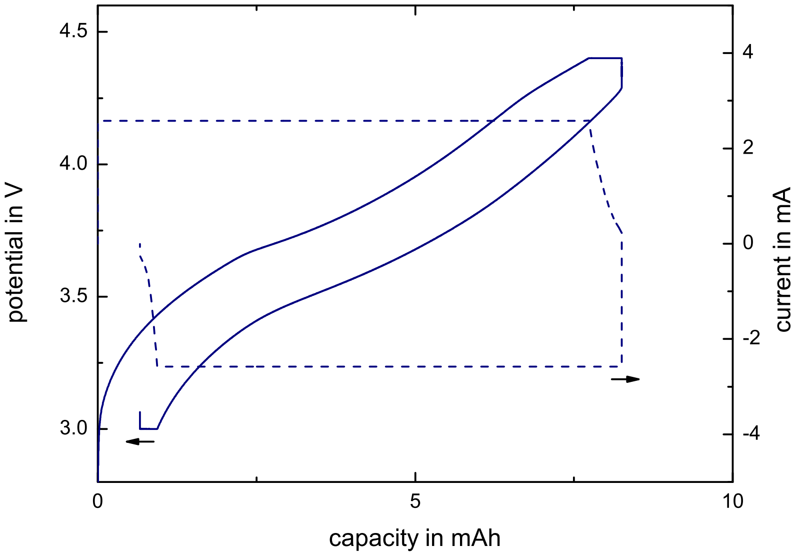

Figure B.5.: Potential and current vs. capacity for C/NMC full cell with oversized anode (z8), as measured during SANS experiment.

In cell z8 the anode was overbalanced by a factor of 5, the cathode was comparable to cell z5. The cell underwent two formation cycles at C/10 (3 to 4.2 V). From the start at 2.5 V the cell was charged to 4.4 V at C/3 (CCCV) and then discharged alike to 3 V.

B.3. SANS raw data processing

The detailed SANS raw data processing follows several steps and involves scaling to a standard. Theoretically, we relate the measured intensity to the absolute cross section by dividing by the intensity of the unscattered beam I_0, according to equation 5.59:

$$\frac{d\Sigma}{d\Omega} = \frac{I_{\mathrm{meas}}(q)}{I_0\, A\, T\, t\, \Delta\Omega} \tag{B.1}$$

(T is transmission, t is thickness, A irradiated surface, and I_0 incoming flux in neutrons per second per area). In reality, it is however often not possible to measure the intensity of the beam without a sample under same conditions, due to fluctuations in the flux or due to restrictions of the sensitivity of the detector which has to be protected from the primary beam. For this reason, instead of I_0 another sample is measured under similar conditions and taken as a standard.

Here, the standard software BerSANS [164, 165] was used to process the raw data from the SANS detector to radially averaged $d\Sigma/d\Omega(q)$ curves. Of course, all comparable data files are acquired in equal measurement durations. All processing steps follow the methods described in the original manual [166] and a manual by Seidlmayer et al. at FRM II [167]:

1. Raw data preparation: beam center and appropriate masks (to mask regions at edge of detector or faulty pixels) are determined

2. Transmission: calculate transmission T for all pixels ij in the beam center (defined by mask) and all samples and standards according to

   $$T = \frac{\sum I_{\mathrm{ij}}}{\sum I_{0\,\mathrm{ij}}} \tag{B.2}$$

   where I is the measured intensity in counts and I_0 the same for empty beam.

3. Absolute scaling: data is corrected for detector deadtime and flux as measured by monitor (a proportional measure to the real beam intensity) and scaled by

   $$I_{\mathrm{ij}} = \frac{\left(\frac{S_{\mathrm{ij}} - B4C_{\mathrm{ij}}}{T(S)}\right) \cdot At(S) - \left(\frac{SB_{\mathrm{ij}} - B4C_{\mathrm{ij}}}{T(SB)}\right) \cdot (1 - p(S))}{W_{\mathrm{ij}}/T(W)} \cdot f_{\mathrm{scaling}} \tag{B.3}$$

   with S counts from sample (for pixels i, j outside beam center in this case), $B4C$ counts from absorbing B_4C for electronic background noise, SB the sample background (e. g. a cuvette, not relevant for pouch cells), W water standard 1 mm and T the respective transmission values. At is the attenuation factor (to compensate for any attenuation of the beam during measurement) and p the probability factor for multiple scattering, which can be assumed to be 1 (At) and 0 (p) in a first approximation. The scaling factor is given by:

$$f_{\text{scaling}} = \frac{col(S)^2\, sd(S)^2}{col(W)^2\, sd(W)^2} \cdot \frac{A\, t_{\text{W}}}{A\, t_{\text{S}}} \tag{B.4}$$

with *col* and *sd* being the measurement geometry given by collimation length and sample detector distance. The last factor accounts for the irradiated area A (or beam slit area) and thickness of the sample or standard. Thus, I_{ij} is indeed the macroscopic cross section as defined theoretically, normalized to T, A, t and water standard. It gives the cross section in the solid angle given by the detector pixel. Errors are calculated from the individual errors in scattering signal from S, W etc. via the root mean square method. The error in q is neglected because we are finally only interested in the integral and stochastic errors in q will not play a significant role. Sometimes, an additional scaling factor which accounts for secondary effects of the thickness of the sample is added but this approach is not meaningful for a layered multi-component system such as a battery.

4. Radial averaging: in order to get the scattering scross section as a function of angle or q for an isotropic sample, we can average the two-dimensional normalized pixel data radially, i. e. over φ. This yields $d\Sigma/d\Omega(q)$, named also $I(q)$ by the software and given in units of cm^{-1}.

5. Merging: If several setups with different q-range have been measured, they can be joined and normalized to the scaling level.

6. Fit: Data fitting $d\Sigma/d\Omega(q)$ was done with the SASfit software [123]. The anode was fitted with the pre-defined “Background” fit function (equivalent to equation 5.29) with all parameters left floating. The cathode was fitted with a superposition of “Background” and “MassFractExp” (equivalent to equations 5.30 and 5.31) where the Porod slope was fixed to $n = 4$ and all other parameters were iteratively adjusted.

B.4. Calculation of Porod invariant, integrated intensity and utilization

From the SANS raw data, i. e. $d\Sigma/d\Omega(q)$, named also $I(q)$, the integrated intensity was calculated by integration with MATLAB by the trapezoidal method where the first and last 4 data points were left out due to high relative errors. Porod's invariant was calculated by integrating $I(q)\cdot q^2$ accordingly. The error in integrated intensity (and Porod invariant) was calculated via the root mean square method, i. e. $\Delta\text{Int. Int.} = \sqrt{\delta q^2 \cdot \sum \Delta I(q)^2}$ or $\Delta\text{Porod inv.} = \sqrt{\delta q^2 \cdot \sum \Delta I(q)^2 \cdot q^4}$, where δq is the q spacing and $\Delta I(q)$ is the individual error of each data point given by the raw data files and BERSANS. The error in q is small in comparison and neglected. In order to highlight the general trend, data points are smoothed with the Savitzky-Golay filter using a 3rd order polynomial and a window of 5 to 13 points.

The utilization was calculated from measured charge transfer Q_{measured} in the following way: Utilization for NMC x in $\text{Li}_\text{x}\text{Ni}_{0.33}\text{Mn}_{0.33}\text{Co}_{0.33}\text{O}_2$ is:

$$x = 1 - \left(Q_{\text{measured}} + \Delta Q_{\text{theor.}x\approx 0.5/\text{pract.}}\right)/Q_{\text{theor.},x=1} \tag{B.5}$$

where $\Delta Q_{\text{theor.}x\approx 0.5/\text{pract.}}$ corrects for irreversible losses by comparing the expected cathode capacity at 150 mAh/g to the capacity actually reached after formation and $Q_{\text{theor.},x=1}$ is the charge equivalent to all mol of Li in the fully lithiated cathode material. The correction term is 1.18 mAh (cell ID z5), 1.44 mAh (cell ID z8), 1.14 mAh (cell ID nov1), compare the figures in section B.2. Note: the unknown small over-lithiation of the pristine material yields a small error in the weight of the pure $\text{LiNi}_{0.33}\text{Mn}_{0.33}\text{Co}_{0.33}\text{O}_2$ phase.

For graphite utilization x in $\text{Li}_\text{x}\text{C}_6$ is calculated just by dividing Q_{measured} by the weighed anode capacity based on 372 mAh/g. However, the anode capacity is restricted to the area that is opposite the cathode. Additional capacity at the sides (anode is oversized) is neglected on the timescale of the experiment. It is assumed that the anode is more or less empty after a CV phase at 3 V, so that $x = 0$ is well justified.

B.5. Overview of all cells for SANS

.

cell ID	description	date	measurem. time per SANS scatter file in min	limiting electrode area in cm²	graphite loading in mAh/cm², based on 360	graphite loading in mAh/cm², based on 372	NMC-111 loading in mAh/cm²	electrolyte	separator
epb	empty pouch bag	May 13	total 88					LP57	
0p10	inactive materials (pouch, Al, Cu, separator, electrolyte)	Aug 13	total 88	9.0				LP57	C2325
1p1	full cell graphite/NMC	Aug 13	total 88	9.0	1.88	1.94	1.53	LP57	C2325
0p2a	full cell without NMC	Aug 13	total 88	12.25	2.12	2.19		LP57	C2325
0p2b	full cell without graphite	Aug 13	total 88	9.0			1.80	LP57	C2325
nov1	full cell graphite/NMC	Nov 13	10	9.0	2.97	3.07	2.53	LP57	C2325
nov1	full cell graphite/NMC	Feb 14	10	9.0	2.97	3.07	2.53	LP57	C2325
z5	full cell graphite/NMC	Sep 14	3	9.0	0.88	0.91	0.88	LP57	C480
z8	full cell graphite (overbalanced)/NMC	Sep 14	3	9.0	5.00	5.17	0.86	LP57	C480
sept26	half cell Li/graphite	Sep 15	3	6.76	1.63	1.68		LP572	C2013
sept33	Li/Li cell	Sep 15	3	6.76				LP572	C2013
					porosity 50±5%	porosity 50±5%			

Table B.1.: Overview of pouch cells built for SANS experiments with all details. Electrode capacity is given on the basis of the practical resp. theoretical capacity of 360 resp. 372 mAh/g.

Acronyms

BET	Brunauer-Emmett-Teller
CPE	constant-phase element
DMC	dimethyl carbonate
EC	ethylene carbonate
EMC	ethyl methyl carbonate
HFR	high-frequency resistance
ID	identity
LFP	Li_xFePO_4
LFR	low-frequency resistance
LP57(2)	type of electrolyte with or without 2% VC
M	mol/l
NCA	$Li_xNi_{0.8}Co_{0.15}Al_{0.05}O_2$
NMC	$Li_xNi_{0.33}Mn_{0.33}Co_{0.33}O_2$
OCV	open-circuit voltage
PEIS	potentiostatic electrical impedance spectroscopy
SANS	small-angle neutron scattering
SEI	solid electrolyte interface
SLD	scattering length density
SLP30	a synthetic graphite by Timcal/Imerys
SoC	state of charge
TBA	tetrabutylammonium
TLM	transmission line model
VC	vinylene carbonate
wt.%	weight percent
XRD	X-ray diffraction

Symbols

a	activity
A	area
α	transfer coefficient or Bruggeman coefficient or angle
b	scattering length
β	angle
c	constant or concentration
γ	constant-phase exponent
d	sample diameter
D	diffusivity
e	elementary charge
ϵ	porosity
η	overpotential
f	scattering amplitude
F	Faraday constant or square root of form factor
G	Gibbs free energy
Γ	integrated intensity
h	height
$\hbar$	reduced Planck constant
ϑ	polar angle
θ	half of the scattering angle
i	imaginary unit
I	current or flux
$\vec{k}$	wave vector
k_{B}	Boltzmann constant
κ	conductivity
L	collimation length
λ	wavelength
m	mass
n, N	numbers
N_{M}	MacMullin number
$\vec{p}$	momentum

P	form factor
$\vec{q}$	scattering vector
Q	charge or capacity parameter
ρ	density or scattering length density
$\vec{r}$	radial vector
R	radius or resistance or universal gas constant
R_{t}	transfer resistance
R_{ion}	(effective) ionic resistance in electrolyte
R_{el}	electrical resistance
s	standard deviation
S	structure factor
$\tilde{S}_{\mathrm{ij}}$	multi-phase scattering function
σ	cross section
t	thickness
T	temperature
τ	tortuosity
U	electrical potential
$\vec{u}, \vec{v}$	displacement vectors
v	velocity
V	volume
x	any value or distance
φ	azimuthal angle
ϕ	phase angle or volume fraction
χ	length measure
ψ	wave function
z	number of electrons
Z	complex impedance
ω	angular frequency
$d\Omega$	solid angle element

Selected publications

Talks and poster presentations given at conferences

- J. Hattendorff, I. Buchberger, J. Schuster, S. Seidlmayer, V. Zinth, P. Kudejova, H. A. Gasteiger, R. Gilles, *Untersuchungen von Elektrodendesign, -alterung & -sicherheit im Projekt ExZellTUM. Batterieforum Deutschland* **2014**, Berlin.

- J. Hattendorff, S. Seidlmayer, I. Buchberger, J. Schuster, F. Kindermann, R. Gilles, H. A. Gasteiger, *Small-Angle Neutron Scattering on Lithium-Ion Pouch Cells. Kraftwerk Batterie* **2014**, Münster.

- J. Hattendorff, J. Landesfeind, A. Ehrl, W. A. Wall, H. A. Gasteiger, *Effective Ionic Resistivity in Battery Materials. 228th ECS Meeting* **2015**, Phoenix.

- J. Hattendorff, S.Seidlmayer, R. Gilles, *Small-Angle Neutron Scattering of Lithium-Ion-Batteries. Deutsche Neutronenstreutagung* **2016**, Kiel.

Peer reviewed papers

- V. Zinth, C. von Lüders, M. Hofmann, J. Hattendorff, I. Buchberger, S. Erhard, R. Gilles, *Lithium Plating in Lithium-Ion Batteries at Sub-Ambient Temperatures Investigated by in situ Neutron Diffraction. Journal of Power Sources* **2014**, *271*, 152-159.

- S. Seidlmayer, J. Hattendorff, I. Buchberger, L. Karge, H. A. Gasteiger, R. Gilles, *In Operando Small-Angle Neutron Scattering (SANS) on Li-Ion Batteries. Journal of the Electrochemical Society* **2015**, *162*, A3116–A3125.

- J. Hattendorff, J. Landesfeind, A. Ehrl, W. A. Wall, H. A. Gasteiger, *Effective Ionic Resistivity in Battery Separators. ECS Transactions* **2015**, *69*, 135-140.

- I. Buchberger, S. Seidlmayer, A. Pokharel, M. Piana, J. Hattendorff, P. Kudejova, R. Gilles, H. A. Gasteiger,
  Aging Analysis of Graphite / $LiNi_{1/3}Mn_{1/3}Co_{1/3}O_2$ Cells Using XRD, PGAA, and AC Impedance. Journal of the Electrochemical Society **2015**, *162*, A2737-A2746
- J. Landesfeind, J. Hattendorff, A. Ehrl, W. A. Wall, H. A. Gasteiger, *Tortuosity Determination of Battery Electrodes and Separators by Impedance Spectroscopy. Journal of the Electrochemical Society* **2016**, *163*, A1373-A1387.
- L. M. Scherf, J. Hattendorff, I. Buchberger, S. Geier, H. A. Gasteiger, T.F. Fässler, *Electrochemical Synthesis of the Allotrope allo-Ge and Investigations on the Use as an Anode Material. Journal of Materials Chemistry* **2017**, *A5* (22), 11179-11187 , L.M.S. and J.H. contributed equally.
- J. Hattendorff, S. Seidlmayer, H. A. Gasteiger, R. Gilles, *Li-Ion Half-Cells Studied Operando During Cycling by Small-Angle Neutron Scattering. Journal of Applied Crystallography.* **2020**, *53* (1), 210-221